POLITECNICO DI MILANO

Scuola di Ingegneria Industriale

Corso di Laurea Magistrale in Ingegneria Spaziale

Non-Destructive Testing in cylindrical geometry by "Pulse Phase Thermography" technique

Relatore:

Prof. Ing. Alfonso NIRO

Co-relatore:

Dr. Ing. Damiano FUSTINONI

Tesi di Laurea di:

Laura SALVI

Matr. 752195

Anno Accademico 2011-2012

Table of Contents

Index of figures

Index of tables

Abstract

This thesis regards Non-Destructive Testing, in particular *Pulse Phase Thermography*. Goal of this work is the characterization of flaws in cylindrical geometry. A semicylindrical pipe, with dummy holes, different both in diameter and in depth under the external surface of the cylinder is taken into account. Different issues linked with the curvature of the surface have to be taken into account, both from a geometrical and from a thermal standpoint: the analysis of the cylindrical sample requires morphological operations, since the projection of the cylinder in the plane seen by the thermo-camera is scaled with respect to the diameter of the cylinder, not to the circumference. Since the analysis has to be conducted on the actual surface of the object under investigation, it is necessary a dilatation of the image; in addition to this aspect, it has to be taken into account also the contribution due to the directional emissivity, which varies as a function of the observation angle between the analyzed point and the thermo-camera. After that the image has been corrected with this operation, the analysis aimed to the characterization of the depth of the different flaws is conducted. Experimental tests show good results. Numerical analyses are conducted to preliminary evaluate the behaviour of the *Pulse Phase Thermography* with non-straight samples and with non-uniform heating and to characterize the optimal excitation parameters. In addition to this, additional analyses on flaws, different both in dimension and in materials typology, are numerically simulated.

Key words: Non-Destructive Testing; Pulse Phase Thermography; Cylindrical geometry; Directional Emissivity; Non-uniform heating.

Sommario

Il lavoro di tesi di seguito proposto si pone nell'ambito dei controlli non distruttivi che adoperano la termografia pulsata con analisi di fase. Obiettivo del presente lavoro è la caratterizzazione di difetti in geometria cilindrica. Si è analizzato un semicilindro di Plexiglas, caratterizzato da fori ciechi diversi sia per diametro sia per profondità. Si sono analizzate diverse problematiche, di tipo geometrico e termico, legate alla calandratura della superficie: l'analisi del provino cilindrico richiede operazioni di tipo morfologico, dato che la proiezione del cilindro nel piano visto dalla termocamera è scalata rispetto alla dimensione del diametro del cilindro e non rispetto alla circonferenza. Dato che l'analisi deve essere condotta sull'effettiva superficie del corpo, è necessaria una dilatazione dell'immagine; in aggiunta a questo, bisogna tenere in conto il contributo dell'emissività direzionale, che varia in funzione dell'angolo di osservazione del punto in esame rispetto alla termocamera. Dopo aver realizzato queste correzioni, si procede all'analisi effettiva finalizzata alla caratterizzazione della profondità dei diversi difetti. Le prove sperimentali mostrano dei risultati soddisfacenti. Si sono condotte anche analisi numeriche per valutare preliminarmente il comportamento della termografia pulsata con analisi di fase, in presenza di provini curvi e di riscaldamento non uniforme, e per la caratterizzazione dei parametri ottimali di eccitazione del provino. Oltre a questo, gli studi numerici permettono di condurre ulteriori analisi su difetti diversi sia per dimensione sia per tipologia di materiale.

Parole chiave: Controlli non distruttivi; Termografia pulsata con analisi di fase; Geometria cilindrica; Emissività direzionale; Riscaldamento non uniforme.

Introduction

Pulse Phase Thermography is a method which forms part of the Non-Destructive Testing branch. This technique is largely adopted in the characterization of flaws in different kinds of samples, due to the typology of analysis applied to the thermal decay of the superficial temperature of the specimen. Indeed, it is based on the evaluation of the Fourier transform of this temporal trend, in such a way that the analysis is shifted from a time domain to a frequency domain. In this way the obtained phase images are less sensitive to effects due to a non-uniform heating and to local variations of thermal emissivity. The results obtained with this technique are, thus, better, due to this particular aspect of the method. The principal aim of this work is the characterization of flaws in cylindrical geometry, topic that has to deal with several issues, principally linked with the curvature of the sample. Since this is the first work in the ThermALab regarding this application of *Pulse Phase Thermography*, some experimental tests are preliminary carried on to characterize the behaviour of this kinds of *specimina* in such case. In addition to this, since the heating device of the laboratory has been improved during the development of this thesis work, some numerical analyses have been conducted to determine the best parameters to adopt in the experimental tests. In particular, this dissertation is structured as follows: it starts with an overview of Non-Destructive Testing in Chapter 1, comparing them with destructive techniques, focusing on cons and pros of each typology of analysis. Then, a detailed description of different typologies of thermography is presented: *Pulse Thermography*, *Lock-in Thermography* and *Pulse Phase Thermography*. In Chapter 2 the main theoretical concepts regarding the analyzed technique are described. A key aspect in this section is the energetic analysis of the so-called thermal waves, the basis of the *Pulse Phase Thermography*. In this way it is demonstrated that they are not real waves, since they do not carry energy. Chapter 3 presents the state of art of this technique, firstly from a more general point of view; then the presentation becomes more specific describing the state of art in the analysis of angled cracks and pipes. Chapter 4 is organized in three parts: in its first section, the experimental results regarding the characterization of the depth of the flaws obtained exploiting all the previous assumptions are presented. Then it focuses on the description of the experimental issues, the analysis of curved sample has to deal with, describing the experimental tests exploited to characterize the behaviour of the sample with regards to each issue. Afterwards, the morphological operations required by the analysis of the cylinder are presented, focusing on the fact that the projection in the plane of the

infrared camera has a dimension proportional to the diameter and to the height of the sample and not to the dimension of the circumference and to its height. Chapter 5 is focused on the numerical simulations. First of all, some preliminary studies on the difference between a straight and a tilted geometry are shown, taking into consideration a simplified geometry. Then, the behaviour of *Pulse Phase Thermography* technique dealing with non-uniform heating is dissected. A study to its sensitivity to different heating time is also carried on, to characterize the heating parameters, useful in the experimental test. In this way, all the preliminary considerations have been examined thoroughly. Chapter 6 presents the results on the cylindrical geometry obtained exploiting all the previous assumptions. The experimental outcomes regarding the characterization of the depth of the flaws are compared with the numerical ones. To generalize the analysis, also other flaws different both in the diameter, in the depth under the external surface and in the reflection coefficients are numerically examined. The section concerning the conclusion and the future developments ends the dissertation.
Appendices report the complete standard deviations of tests made in Chapter 4 (Appendix A), an analysis of the Fourier equation with the method of the separation of variables (Appendix B), further information on the developed heating device (Appendix C) and a close examination of the hyperbolic formulation of the Fourier equation (Appendix D).

Chapter 1
Overview of Non-Destructive Testing

Non-Destructive Testing *"…is an examination, test, or evaluation performed on any type of test object without changing or altering that object in anyway, in order to determine the absence or presence of conditions or discontinuities that may have an effect on the usefulness or serviceability of that object* [1]". The Non-Destructive Testing technique is able, thus, as it is stated by its own definition, to determine the existence of different kinds of anomalies, such as flaws, discontinuities, leaks, contamination or imperfections in different components without invalidating the integrity of the inspected part. On the other hand, Destructive Testing technique is defined as "*a form of mechanical test, primarily destructive, of materials whereby certain specific characteristics of the material can be evaluated quantitatively* [1]". Such destructive tests can provide direct and accurate information [2], especially relating to the material's design and in-service behaviour. For the majority of the cases, the specimens, during the tests, are subjected to particular conditions able to reproduce the in-service pattern of the object. The information obtained from this technique is quite precise, but it only applies to the examined specimen, since during these tests it is destroyed or irreversibly changed. For this reason the specimen cannot be used for goals different from the mechanical tests. In addition to this fact, although the test specimen is assumed to be representative of its original matrix, it may have not exactly the same characteristics and peculiarities of the material. To sum up, this technique is able to give reliable data, useful for design goals. The information obtained is, in the majority of the cases, quantitative, in such a way that it is possible to establish standards and specifications. Typically, Destructive Testing technique is capable to measure different service conditions of the objects under investigation and the data do not require any elaboration. On the other hand, these data are applied only to the specimen under investigation, that, usually, can be utilized only during the test. Non-Destructive Testing is complementary to this method. They do not, generally, provide quantitative data and the given indirect information needs to be interpreted. In addition to this fact, the orientation of discontinuities has to be taken into account. However, the specimen is not altered and it can be used also after the test. Depending on the chosen technique, both internal and superficial integrity of the part can be analyzed and, with no adverse consequences, it is possible to investigate also a large portion of an object. This is, in general, a cost effective technique, although with some exceptions, as radiography, for example. In addition to these aspects, parts can be examined also while the objects are in

service [1]. This opportunity represents a distinct advantage of non-destructive techniques over destructive ones. Non-Destructive Testing, indeed, is exploited also during the in-service-life of the object, to determine the necessary maintenance requirements, monitoring periodically the conditions of damage growth in order to assure the safe operation of the investigated part. In addition to this fact, this technique can be also utilized for real-time control of the different objects during manufacturing process to measure the physical properties and to inspect assemblies for tolerances and alignment. Indeed, during the last years, non-destructive evaluation of different parts is becoming more and more important in the design and manufacture stages. The cost of materials is rapidly growing up and, subsequently, even the cost of the different parts utilized in different industrial fields is increasing. Components which have problems in accomplishing their primary requirements due to several undetected defects may require expensive repair or they may cause catastrophic failure. Thus, it is fundamental the use of this technique early both in the design and in the fabrication process. With the development of new materials, such as composites, non-destructive technology is constantly improving its applications, thanks also to the advances in imaging technology as well as to the improvements in post-processing techniques, increasing the quality of the information obtained by this kind of control [3]. Several methods are considered in this field, ranging from the simplest to the most complicated. Visual inspection is the simplest of all. Surface imperfections invisible to the eye may be revealed by penetrant or magnetic methods. In general, these methods are unsuited for crack defect identification [4].If really serious surface defects are found, it is usually necessary an examination of the interior by ultrasound or thermography. Penetrant testing is based on the capillarity principle, a surface tension phenomenon that allows liquids to be drawn into small openings, an effect due to energies at the surfaces of the openings. This is a method which can be employed for the detection of discontinuities in any non porous material. In its procedure a liquid penetrant is applied to the surface of the object under investigation. Then the penetrant in excess is removed from the surface. The surface is then dried and a developer is applied to it. The penetrant which remains in the discontinuity is absorbed by the developer to indicate the presence of the discontinuity and to characterize it. Magnetic particle testing is used for the testing of materials which can be easily magnetized. This method detects flaws located just below the surface. The specimen is magnetized, inducing a magnetic field inside it. In the case in which a flaw is present, this changes the flow of the magnetic lines of force. So, some of these exit and re-enter in the specimen, forming opposite magnetic poles. Several little magnetic particles are sprinkled on the surface of the specimen and they are attracted by these poles, in such a way that it is possible to characterize the defect [1]. For more specialized situations, different kinds of methods are more useful. Ultrasonic testing is based on high-frequency sound waves introduced into materials, through which these waves travel with some associated loss of

energy. Considering an inhomogeneity in a material, a portion of these waves may be transmitted to the next medium and the remainder reflected back. It is important to highlight that interface is meant as the boundary between one medium and another one. The ratio between the part transmitted and the one reflected depends on the properties of the materials on either side of the interface. To give an example, in a steel-to-air interface all the energy reflects and virtually none goes into the air. If there is a steel-to-water interface, 88% of the energy is reflected and 12% is transmitted into the water [1]. The reflected beam is analyzed to define the presence and the characterization of flaws or their absence. This kind of methodologies is exploited in several fields, such as the radar systems for the air traffic control with the electromagnetic wave propagation, the ultrasonic images of the fetus implying the mechanical wave propagation and the medical x-rays with the penetrating radiation [2]. It is important to highlight that none of these methods is able to provide a solutions to all the possible problems, they are not mutually exclusive but rather complementary to each other.
Another fundamental technique is the infrared thermography.

1.1 Infrared thermography

This work is focused on this last field of study, which is inherent to infrared thermography, a useful technique to determine whether a component has subsurface anomaly, as delaminations, gaps or different inclusions. This technique involves the measurement or mapping of surface temperatures as heat flows to the object under investigation. The basic premise of thermographic Non-Destructive Testing is that this flow of heat from the surface of the solid is affected by internal flaws of different kind. In this treatment defect conductivity is considered equal to the air conductivity $\left(k = 0.02\ \frac{W}{m\ K}\right)$. For this reason, detecting the temperature on the upper surface of the specimen, the zone corresponding to the flaw surface is hotter than the rest of the specimen. Hence this technique acquires and analyzes thermal information exploiting non contact thermal imaging devices. The experimental set-up required by this method is, thus, a thermal imaging system, that is an instrument that creates pictures of the thermal radiation emitted by a body, and a post processing data system, a computer, to obtain information on the physics characteristics of the defect. In addition to these instruments, in the case of active thermography, a heating source is required. Indeed an external stimulus is necessary to induce relevant thermal contrasts. Passive and active approaches are considered in optical applications; the first one investigates specimen structures that naturally have different temperatures, the thermal radiation emitted from their surfaces is scanned by an infrared camera, giving information about the surface

temperatures of the object in thermal equilibrium; in the active thermography process, instead, the object under investigations is thermally excited with a pulse of heat applied to the specimen; the object is in non equilibrium state: when energy is focused onto its surface, the material absorbs some of the incident energy, producing a localized heat flow on the specimen. This time-dependent heat flow is governed by the one dimension diffusion equation:

$$\alpha \frac{\partial^2}{\partial x^2}\big(T(x,t)\big) = \frac{\partial T(x,t)}{\partial t} \text{ [5],} \qquad (1.1)$$

where α indicates the thermal diffusivity of the material, equal to $\frac{k}{\rho c}$. An infrared thermo-camera records the thermal response to this stimulus, that is the infrared emission from the surface. Figure 1.1 schematizes the active approach. Therefore, thermography offers noncontact, wide area detection of subsurface defects [6], characteristics that made it one of the most studied techniques of the last years.

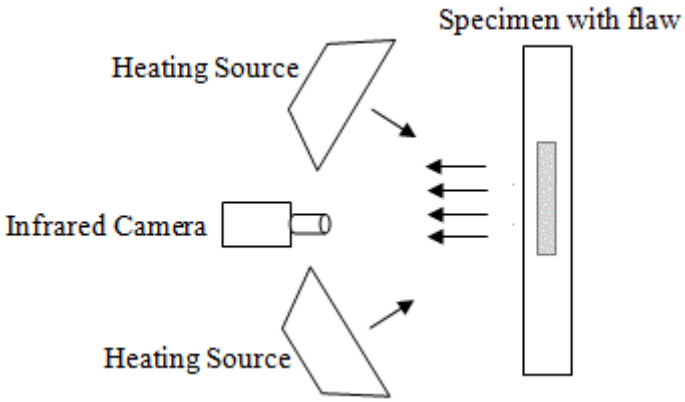

Figure 1.1: Outline of the active thermography.

It is important to highlight that any Non-Destructive technique is not a *panacea*, each one of them has its own strengths and weaknesses. In the case of thermography, it has proven itself as an inspection technique that is highly effective and very easy to use, whereas other applications may require deeper analyses. On the other hand, it has to deal with the difficulties both to determine the amount of energy necessary to excite the specimen in the most effective and feasible way and to deposit this energy onto a wide surface in a short interval of time. In addition to this fact, it is considered a "*boundary technique* [7]", due to its capability to detect only subsurface defect, it is sensitive to the effect of thermal losses, caused by conduction, convection and radiation and it has the capability of detecting only defects that cause a reasonable change of the thermal properties.

These pros and cons are found also in the tree principal methods that are developed: active thermography comprehends, principally, *Pulse*, *Lock-in* and *Pulse Phase Thermography*.

1.1.1 Pulse Thermography

In *Pulse Thermography* the specimen is subjected to a thermal pulse, the duration of which depends on the thermal characteristics of the specimen: the heating stage spaces from few milliseconds for high conductivity materials, such as metals, while, low conductivity materials, like plastics, are heated for few seconds [6]. This technique is a fast method, since its investigation depends only on the duration of the heat pulse [5].The temperature of the upper surface of the specimen is, then, recorded by a thermal imaging device. During the heating stage the temperature rises and then it decays during the cooling phase due to the diffusion under the surface. The flaw reduces the diffusion rate in such a way that its presence causes a heat accumulation. So its projection over the upper surface origins an area of higher temperature with respect to the surrounding undamaged zones. This temperature difference is a time dependent phenomenon: shallower defects are observed before with respect to the deeper defects, which are characterized by a reduced thermal difference. The observation time is linked to the defect depth by the relation:

$$t = \frac{z^2}{\alpha}, \tag{1.2}$$

where α is the thermal diffusivity of the material. An empirical rules states that "*the radius of the smallest detectable defect should be at least one to two times larger than its depth under the surface"* [8][9]. A recent theoretical study, [10], has the goal to improve this ratio. Both a point inspection and a surface investigation are possible: in the first case the heating is obtained with a laser or a focused beam in such a way that it is not difficult to obtain an uniform heating; on the other hand this technique involves the necessity to heat different points to inspect the whole specimen and this drawback slows down the process a lot; on the contrary, surface inspection exploits lamps to make a complete analysis of the phenomenon, but the difficulty to heat the sample in a uniform way has to be carefully considered. Since the basis of this technique is the differential temperature between the thermal sources and the object under investigation, if the temperature of the specimen is higher with respect to the environment temperature, the specimen can also be subjected to a cold thermal source, as an air jet: this does not involve spurious effects in the thermo-camera. In general it is preferred to heat the sample for sake of simplicity. Two different methods are

possible: reflection mode and transmission mode. As they are depicted in Figure 1.2, reflection mode requires that the thermal source and the camera are on the same side with respect to the analyzed object, while they are located on its opposite side in the latter methodology, a method useful to detect defect close to the bottom surface thus requiring the accessibility to the rear surface. In addition to this fact, in transmission approach the thermal waves travel along the same distance, in such a way that the flaw can only be detected, but not characterized [6].

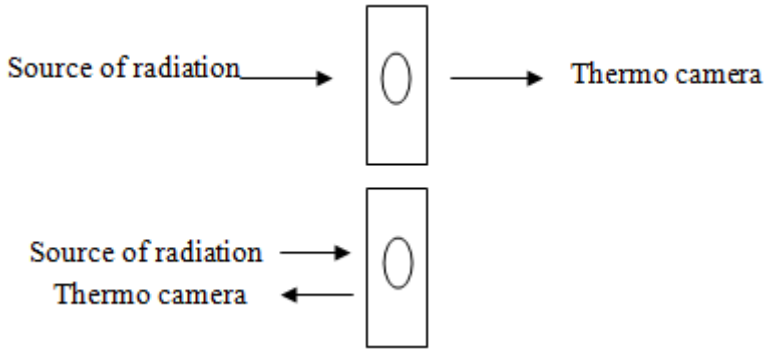

Figure 1.2: Transmission mode (above) and reflection mode (below).

1.1.2 Lock-in Thermography

In *Lock-in Thermography*, the specimen is thermally excited using a periodic heat source. In the case of a sinusoidal temperature stimulation of a specimen, thermal waves, which are highly attenuated and dispersive waves, are found inside the material. These waves can be generated and detected remotely, for example exploiting a lamp that is able to depose periodically heat on the surface of the specimen [6]. After the reaching of the steady state regime, the thermal response is recorded by the infrared camera, which has to be synchronized to the excitation source. From the recorded temperature response, phase and amplitude images can be generated. This is one of the principal differences distinguishing *Lock-in Thermography* from *Pulse Thermography*, since these parameters are both available in the thermal images obtained with this technique [6] [10]: in *Pulse Thermography* are obtained images which are connected to the radiation emitted by the surface; amplitude images, on the other hand, are related to thermal diffusivity, while phase images to the propagation time [8] [9]. These last images are exploited to reveal local thermal subsurface inhomogeneities. In [11] is found the relation that relates the probing depth and the frequency, involving the thermal diffusion length:

$$\mu = \sqrt{\frac{2\alpha}{\omega}}\ [5], \tag{1.3}$$

where ω indicates the modulation frequency. A low modulation frequency causes a deeper probing. On the other hand, due to the damping of the thermal waves, as it is stated in [12], the depth of the probing is limited to surface features. The velocity of propagation of the thermal waves depends on the thermal characteristics of the materials:

$$\nu = \lambda * \frac{\omega}{2\pi} = \sqrt{2\omega\alpha}\ [5], \tag{1.4}$$

where α is the diffusivity and $\lambda=2\pi\mu$.
A direct relation exists between the phase and the depth z:

$$\frac{2\pi z}{\lambda} = \frac{z}{\mu}\ [5]. \tag{1.5}$$

The *Lock-in Thermography* has a better depth resolution and it is less sensitive to surface variations, as non uniform heating and emissivity variations, but it requires a long measurement time, especially with low thermal conductivity materials [5].

1.1.3 Pulse Phase Thermography

Pulse Phase Thermography combines the two techniques described above. Its basis is the heating of the sample exploiting a heat pulses, as in the *Pulse Thermography*, but the analysis is done in the frequency domain in such a way that the thermal waves launched in the specimen can be analyzed in a more efficient way. In *Lock-in Thermography*, only one frequency is tested in the quasi-steady-state regime. In *Pulse Phase Thermography*, otherwise, all frequencies can be tested in the transient regime, exploiting the Fourier transform. To derive a phase image, usually, the Discrete Fourier transform is exploited. It is important to highlight that if N thermograms are acquired, due to the *hermitian* symmetry of the Fourier Transform, $\frac{N}{2}+1$ phase images are available, associated to the frequencies that goes from 0 frequency, which does not contain useful information, to $\frac{N}{2}\Delta f$, where $\Delta f = \frac{1}{t_{observation}}$.
To go deeper below the surface, large observation time or large N are required. It is important to highlight that the longer the pulse in the time domain, the higher energy is concentrated in the low frequencies range. If defects very near

to the surface are observed, it is necessary a shorter heat pulse, since high frequencies are required. This implicates the problem to depose an appropriate amount of energy uniformly on the surface of the specimen in a brief interval of time. This technique is able to detect deep flaws under the surface and it is characterized by a better defect shape resolution compared with the thermal contrast exploited by the *Pulse Thermography*. Its drawbacks are the fact that the choice of the thermal pulse duration also affects the results and the loss of temporal information due to the intrinsic nature of the Fourier Transform [5]. The complex Wavelet transform can be used to preserve time information of the signal, which can be correlated to defect depth. The Morlet wavelet is a complex sinusoid in which it is possible to tune some parameters, such as the central frequency f_c, in order to match the characteristics of the specimen under investigation. An area of the sample without defect is taken as a reference. When a maximum is reached in the wavelet phase contrast, the instant of time when this situation occurs correspond to the defect depth [5].

Chapter 2

Theoretical background

The basis of each thermal process relies on the variation of the temperature of the body under investigation. This changing is connected to the variation of the internal energy of the body, as it is expressed in the first law of thermodynamics, which states that the variation in the total energy is due to the amount of energy that enters in the volume under investigation minus the amount that leaves it.

$$\frac{dE}{dt} = Q + \Sigma, \tag{2.1}$$

where Q is the heat flow, positive if it enters in the system, while Σ refers to the pseudotrasformation of energy, connected to the internal energy. Taking into account an infinitesimal volume dV, with a mass dM and an energy dE, the previous equation becomes:

$$\int \left(\varrho c \frac{\partial T}{\partial t} + \nabla \cdot q - \sigma \right) dV = 0, \tag{2.2}$$

where ρ is the density of the body under investigation, σ is the internal heat flow per unit volume and q refers to the heat flux, which has to be characterized. *Rate equations* are exploited to compute the amount of energy that is transferred per unit time [13]. As it is stated in section 1.1, the basis of the Infrared Thermal Testing relies on heat conduction. Two constitutive equations are commonly used in the analysis of conduction heat process, which arise to different formulations of the temperature field.

2.1 Parabolic formulation

The first analyzed constitutive law is the so called *Fourier's law*. This implies a linear relation between the heat flux through a material and the gradient of temperature:

$$\vec{q}(x,t) = -\underline{\underline{k}} : \vec{\nabla} T(x). \tag{2.3}$$

It is important to underline that the heat flux has the same direction of the temperature gradient, but an opposite sense: the heat flows from the area with a higher temperature to the ones characterized by a lower temperature, while the temperature gradient has an opposite behaviour. *k* is a parameter of the material in which the conduction occurs, it is a transport property called *thermal conductivity* [13]. Since this is a physical parameter, it has to be positive. Thus, the minus sign in the Fourier equation is due to this aspect. Defining *k* as $k = \mathcal{K}(r; \mathcal{T}(r,t))$, it is easily noticed that *k* has a twofold dependence on the spatial coordinate: direct and indirect. In the inhomogeneous material, *k* varies because of the changing of the material constituting the object. In addition to this fact, the temperature, in general, varies from point to point. Consequently, *k* is different in each point of the material. For the ideal gas, considering the dependence on time:

$$\mathrm{k} = \mathrm{k_o}\sqrt{\frac{\mathrm{T}}{\mathrm{T_0}}}, \tag{2.4}$$

where the 0 subscribes refers to a condition in which both *k* and T are known. For the other cases, the definition of *k* is quite complicated. In this treatment, this indirect dependence is considered negligible and only homogeneous materials are taken into account. So *k* is assumed to be independent from its own position inside the object goal of the study. Accordingly to this hypothesis, the diffusion equation of energy is obtained from a revision of the previous equations:

$$\varrho \mathrm{c}\frac{\partial \mathrm{T}}{\partial \mathrm{t}} = \mathrm{k}\nabla^2\mathrm{T} + \sigma, \tag{2.5}$$

that, in the case in which no internal heat flow is generated, becomes the *Fourier's equation* [13]:

$$\varrho \mathrm{c}\frac{\partial \mathrm{T}}{\partial \mathrm{t}} = \mathrm{k}\nabla^2\mathrm{T}. \tag{2.6}$$

Defining α, the thermal diffusivity, defined as $\alpha = \frac{\mathrm{k}}{\rho \mathrm{c}}$, it becomes:

$$\frac{\partial \mathrm{T}}{\partial \mathrm{t}} = \alpha\nabla^2\mathrm{T} \tag{2.7}$$

This model is, thus, characterized by a partial differential parabolic equation. The speed of thermal propagation is infinite, in such a way that the temperature stabilizes immediately after the application of the thermal stimulus. This implies

that the effect of a temperature change at some points of the domain is experienced instantaneously in the whole domain [14]. Indeed, the *Fourier's law* is an empirical relation, it has no physical meanings [15]. Then a modified model describing the link between temperature and heat flux is proposed, that leads to a hyperbolic formulation.

2.2 Hyperbolic formulation

To overcome the matter of an infinite propagation speed, Cattaneo [16] and Vernotte have proposed a different constitutive equation, which gives the possibility to consider the propagation speed, introducing a delay.

$$\vec{q}(x, t + \tau) = -k\vec{\nabla}T(x, t). \tag{2.8}$$

Considering a Taylor expansion of the heat flux around τ=0, the previous equation becomes:

$$\vec{q}(x, t) + \tau \frac{\partial \vec{q}(x,t)}{\partial t} = = -k\vec{\nabla}T(x, t). \tag{2.9}$$

Thus, the hyperbolic heat conduction equation is [17]:

$$\frac{\partial T}{\partial t} + \tau \frac{\partial^2 T}{\partial t^2} = \alpha \nabla^2 T, \tag{2.10}$$

that, in the case of a cylindrical domain, becomes [18]:

$$\frac{\alpha}{r}\frac{\partial}{\partial r}\left(r\frac{\partial T}{\partial r}\right) = \frac{\partial T}{\partial t} + \tau \frac{\partial^2 T}{\partial t^2} \tag{2.11}$$

The previous equation has, as solution, a temperature field which propagates with a finite speed equal to [18]:

$$\nu = \sqrt{\frac{\alpha}{\tau}}. \tag{2.12}$$

The Fourier's law shows good consistency with experiments for most practical problems, since the relaxation time τ is usually small [14]. More specifications are given in Appendix D.

2.3 Analytical issues

2.3.1 Energetic analysis of the thermal pseudo waves

In a solid specimen heated by a periodic source, temperature oscillations take place. Their formulation is like the ones of highly damped wave. To give an example, they are similar to the ones found in metals when electromagnetic waves propagate through them [17]. For this reason, in literature, such phenomenon is usually called thermal waves. Otherwise, a study of 2006, [17], has demonstrated that these are improperly called waves, since their nature is different from that of a wave, due to the fact that they do not bring any energy contribution. This is demonstrated both for the parabolic heat conduction equation and for the hyperbolic formulation of this equation, based on the Cattaneo's relation between the heat transfer and the temperature gradient. The treatise takes as reference a semi–infinite medium opaque, as it is depicted in Figure 2.1, excited by a periodic light source of intensity I_0 and modulation frequency f.

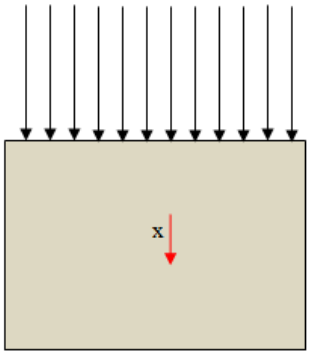

Figure 2.1: Geometry of an opaque semi-infinite medium.

2.3.1.1 Parabolic case

In the case of the parabolic formulation, exploiting, as a boundary condition, the continuity of the heat flux on the surface of the medium, the time dependent component of the temperature results:

$$T(x,t) = Re\left[\frac{I_0}{2kb}e^{-bx}e^{i\omega t}\right] = \frac{I_0}{2\varepsilon\sqrt{\omega}}e^{-\frac{x}{\mu}}\cos\left(\frac{x}{\mu} - \omega t + \frac{\pi}{4}\right), \qquad (2.13)$$

where $b = \frac{\sqrt{i\omega}}{\alpha}$ and ε is the thermal effusivity of the specimen.
This is the solution of a diffusive equation, with first order time derivative. Although, due to the fact that this formula has the same mathematical shape of a plane, harmonic and highly damped wave, the temperature oscillations are usually called thermal waves, even if they are not the solution of a wave equation, which usually involves a second order time derivative [17]. Exploiting the Fourier's law obtained in section 2.3.1.1, the corresponding heat flux becomes:

$$\vec{q} = \frac{I_0}{2}e^{-\frac{x}{\mu}}\cos\left(\frac{x}{\mu} - \omega t\right)\vec{\imath}\,. \qquad (2.14)$$

It can be easily noticed that the time average over a whole period is 0. Thus, the so called thermal waves do not carry energy. In the real waves, there is a quadratic relation between the intensity and the physical quantity involved in the propagation, while, in this case, the Fourier's law establishes a different link between the heat flux and the temperature.

2.3.1.2 Hyperbolic case

Exploiting the same procedure utilized before, the heat flux, imposing as boundary condition:

$$q(0,t) = I_0 e^{\frac{i\omega t}{2}}, \qquad (2.15)$$

in this case results:

$$\vec{q} = \frac{I_0}{2}e^{\left(-\left(\frac{1}{2\sqrt{\alpha\tau}} + i\frac{\omega\sqrt{\tau}}{\sqrt{\alpha}}\right)x\right)}\cos(\omega t)\vec{\imath}\,. \qquad (2.16)$$

Also in this case the time average of the heat flux over a period is equal to 0. So, also in this case, the temperature oscillations cannot be seen as real waves, although in this case they are solution of a wave equation [17].
Thus, it is demonstrated that, both in the parabolic and in the hyperbolic formulation, the nature of temperature oscillations is different from the one of travelling waves. For this reason, from this point forward, temperature oscillations are called pseudo thermal waves.

2.3.2 Reflection and transmission coefficients

For a more detailed exposition of the basic concepts expressed in this section, the reader should refer to [19]. Basing on [20] [21] [22] [23], it is possible to define two important coefficients useful in the following analyses. An interface between two different materials, each one homogeneous inside, is considered. Without lack of generality, a plane pseudo thermal wave is taken into account, incident with an angle ϑ_i on the interface posed at z=0 whose normal is parallel to z axis. When the pseudo wave travels from one material to the other one, it is split in one reflected pseudo wave in the first material and in one transmitted pseudo wave in the second medium. Exploiting the Schnell laws, imposing the equality between the temperature and the heat flux at the interface, the reflection and transmission coefficients are obtained:

$$\hat{r} = \frac{e_1 \cos(\vartheta_i) - e_2 \cos(\vartheta_t)}{e_1 \cos(\vartheta_i) + e_2 \cos(\vartheta_t)}, \tag{2.17}$$

$$\hat{t} = \frac{2e_2 \cos(\vartheta_t)}{e_1 \cos(\vartheta_i) + e_2 \cos(\vartheta_t)}. \tag{2.18}$$

It is important to highlight that e_1 and e_2 are the thermal effusivity of each medium, defined as:

$$e = \sqrt{k\varrho c} \quad \left[\frac{Ws^{0.5}}{m^2 K}\right] \tag{2.19}$$

In the case in which the incident pseudo thermal wave is normal to the interface, they become:

$$\hat{r} = \frac{e_1 - e_2}{e_1 + e_2}, \tag{2.20}$$

$$\hat{t} = \frac{2e_2}{e_1 + e_2}. \tag{2.21}$$

In the case of an interface Plexiglas-air, it is assumed that the normal incident pseudo wave is almost totally reflected, due to the high value of the r coefficient (0.98) in this case.

2.3.3 Thermal pseudo waves

To enhance comprehension of the physics of the system under investigation, a one dimension solution is taken into account. It is demonstrated in [19] that, considering a model, whose heat transfer model is described by the equation obtained in the previous section, subjected to a heating source able to deposit heat on its upper surface with a particular modulation frequency, the basic solution at time t and depth z is described by a thermal pseudo wave of amplitude T_0 and frequency f :

$$T(z,t) = T_0 e^{-\frac{z}{\mu}} \cos\left(2\pi ft - \frac{z}{\mu} - \varphi\right), \tag{2.22}$$

where $\mu = \sqrt{\frac{\alpha}{\pi f}}$ is the thermal diffusion length.
The propagation speed of this pseudo wave is:

$$\nu = \sqrt{4\pi f\alpha} \tag{2.23}$$

It is important to highlight that the modulation frequency is inversely proportional to the thermal diffusion length but, at the same time, it has a direct relation with the speed of the waves: the higher the frequency, the nearest the investigation and the faster the wave; the lowest the frequency, the deepest the analysis but with the smallest speed. For $z=\mu$ the amplitude of the wave is attenuated of a factor equal to $\frac{1}{e}$. If in a sample some discontinuities are present, such as delaminations, air bubbles and so on, when the wave passes through different material, due to the different physical properties of the interface ($\alpha_1 \neq \alpha_2$), a reflection of the pseudo wave occurs. This effect is strongly affected by the physical nature of the interface: the highest the difference between the properties of the material of the object under investigation and the properties of the flaw, the highest the effect on the reflected thermal pseudo wave. Thus, on the external surface, the contribution of this reflected pseudo wave is present:

$$T(z,t) = T_0 \cos(2\pi ft - \varphi) + \hat{r}\, T_0 e^{-\frac{2L}{\mu}} \cos\left(2\pi ft - \frac{2L}{\mu} - \varphi\right). \tag{2.24}$$

Thus, if the material is homogeneous, the temperature on the upper surface, where the heat flux is applied, is uniform everywhere, swinging constantly in time. If the material is heterogeneous, in such a way that the thermal wave deals with different thermal properties, a series of hotter isotherm curves occurs on the

heated surface, by the flaw: over the defect the area is hotter due to the reflected wave that affects it, which appears later in time. The analysis can be conducted both in the time field or in the frequency field, transforming each temperature value accordingly to the Fourier transform, in such a way that a direct analysis on the phase is possible. The presence of a defect, indeed, causes a phase shifting. With this method, any thermal stimulus can be seen as the summation of harmonic functions, exploiting the superposition principle. This can be applied due to its linear nature. In this way, knowing the response to a harmonic thermal excitation, the response to different *stimuli* with various natures can be found.

2.4 Impulsive heating

The heating of the surface is obtained by lamps. Their thermal stimulus is not an infinitesimal pulse, but, in first approximation, it is a rectangular pulse characterized by an amplitude q_0 and a duration τ. The frequency spectrum of this rectangular pulse is:

$$Q(f) = q_0 \tau \frac{\sin(\pi f t)}{\pi f t} \; e^{(-j\pi f t)}. \qquad (2.25)$$

The longest the duration of the pulse, the smallest the frequency band excited, as Figure 2.2 shows. For τ tending to 0, all the frequencies are excited with the same amount of energy, while, as τ increases, the energy is given principally to the lower band of the frequency spectrum. Thus, exploiting a finite pulse, with the proper calibration of its duration, thermal waves propagation occur for all the frequencies, but their amplitude is going to decrease as the frequency grows up. In this way, considering a finite pulse, the noisy higher frequencies are not taken into account. In the cases analyzed in this work, the values of interest are the lowest, since the maximum phase difference occurs at the lowest frequencies, in such a way that the choice of a pulse with a finite duration does not invalidate the results.

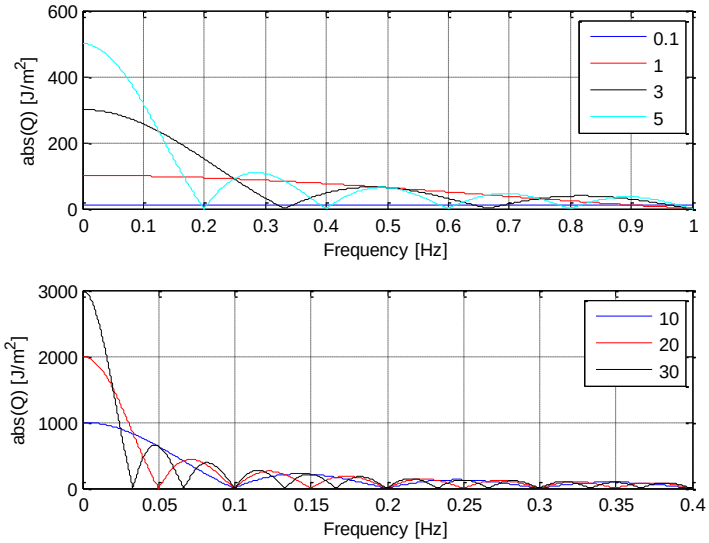

Figure 2.2: Frequency spectrum of the rectangular pulse heating, different frequencies

2.5 Black Body theory

Infrared thermography, as it is stated by its own name, implies the record of the radiated electromagnetic energy. The employed thermal imaging system is able to detect these radiometric emissions and, with the proper calibration, it is possible to connect these measured values to their corresponding temperature, since there is a biunique relation between them. An ideal emitter, called black body, is an object able to emit the maximum energy in a uniform way in all directions and to absorb the radiation coming from all directions. Since the black body is an ideal surface, the radiation emitted by the real bodies is always less with respect to it [13]. For this reason, the *emissivity* ε is a measure of the ratio of the intensity of the radiation emitted by a body to the intensity of the radiation emitted by a black body [13]. In general this parameter depends directly on the wavelength, on the temperature and on the viewing angle. As Maldague affirms in [6], for most common thermographic procedures, this aspect is neglected, without an excessive approximation. It is important to highlight that surfaces with a low emissivity behave like a mirror, following the Kirchoff laws. Thus it is difficult to measure their temperature basing on radiometric emission. For this reason, in several cases the surfaces under investigation are painted in black, increasing the superficial emissivity.

Chapter 3
State of art

3.1 Infrared Thermography

This work is focused on infrared thermography, a field of interest of several groups of study, due to the versatile applications of this technique. The principle at the basis of this technique has been known since 1800, when Sir William Herschel, using a prism to break sunlight into its various colors, measured the temperature of each color using a very sensitive mercury thermometer. The temperature increased when he moved out beyond red light into an area he came to term the "dark heat." This is the area of the electromagnetic spectrum, linked to the electromagnetic radiation that is able to cause an increase of the temperature of the material when absorbed [1]. In the following years, other developments have been conducted, for example in 1840, when Herschel's son, Sir John, using an evaporigraph, produced the first infrared image, exploiting the differential evaporation of a thin film of oil. During the two world wars, this technique was accurately studied. The discovery by German scientists that a cooled detector gave better performances allowed the rapid expansion of the infrared technology. It was not until the 1960s that infrared thermal imaging began to be used for non-military applications. Thanks to the continuous improvements in the computer technologies and in thermal imaging process, the study of this technique continues to spread out, increasing the different procedures applied. The first article on *Pulse Phase Thermography* is published by Xavier Maldague [24], who is one of the most important researcher of this method. He focuses his attention also on the improvements in the data treatment [25] [26] [27]. Mulaveesala of the Indian Institute of Technology focuses his attention on the Frequency Modulated Thermal Wave Imaging technique, an evolution of the *Lock-in Thermography*, basing on the simultaneously acquisition and excitation of the sample with a frequency that increases linearly with time [28]. Different kind of materials have been studied, such as composites, by Vavilov of the Tomsk Polytechnic University [29] [30], or Plexiglas. This work is focused on the detection of flaws in this last kind of material. The defect is, usually, characterized both in term of diameter and depth. The first aspect is more complicated, principally because of problems coming from measurements noise and the filtering of the images, which could cause the boundaries of the defect to be shaded. The technique of the segmentation, proposed by Maldague [31], is one of the principal methods

exploited. Another analysis is conducted considering the value of each pixel with respect to the mean value obtained from the thermography, in such a way that the difference becomes the *discrimen* for the establishment if the pixel belongs or not to the flaw. [32]. With respect to the depth identification, this aspect is analyzed in different studies. In specimen with a depth of 4 mm or 6.5 mm, such defects are detected and characterized in an accurate way when their diameter is 10 mm, while, if they have a 5 mm diameter, they are only detected, but their characterization is not so close to the real condition [33]; considering samples characterized by a 8 mm depth [34], taking into account the *Lock-in Thermography* technique, flaws with a 10 mm diameter are found to have an accurate characterization of their depth, while, regarding to the identification of the diameter, the higher the depth, the more inaccurate the results. The same procedure is applied with the *Pulse Phase Thermography*. This technique, in this case, allows an accurate detection of the flaws only when the their depth is less than 3 mm. Regarding to the space field, the NASA agency applied *Pulse Thermography* with a first control after the re–entering of the Space Shuttle, for the evaluation both of its leading edge and of its front part, constituted both by reinforced carbon fibres [35].

3.2 Angled cracks and Pipes

One of the principal aims of this thesis concerns the study of flaws in *specimena* with particular configuration with respect both to the heating source and to the infrared camera. A study on the first aspect of interest has been done by researchers of the Federal Institute for Material Researcher and Testing [4]. Heating the sample with a laser with a maximum power density of 8.2 kW/cm^2, they have verified a method suitable for the quantitative characterization of depth and angle of surface cracks, evaluating the crack-caused asymmetry of the laser's thermal footprint. The laser is used to heat the specimen locally in a fixed lateral distance d perpendicular to the position of the crack for 2 seconds. For a perpendicular flaw, the difference between the detected spatially averaged temperature in two reference areas at a fixed distance *e* to the laser spot is analyzed,

$$\Delta T_{d,i}(t) = T_{1,i}(t) - T_{2,i}(t), \tag{3.1}$$

where 1 and 2 refers to both sides of the crack. The temporal mean temperature difference in a range t_1- t_2 is taken into account:

$$c_{d,i} = \frac{1}{t_2 - t_1} \sum_j \Delta t \, \Delta T_{d,i}(\Delta t \, j). \tag{3.2}$$

Comparing this parameter to a calibration curve, which has to be previously determined using an experimental campaign of test specimens, the depth of the flaw can be found. To determine the depth and the angle of an angled crack, it is possible to evaluate $c_{d,I}$ for two experiments with laser excitation on each side of the crack. Referring to the parameter found before, in this case the following relations are obtained:

$$\Delta T_d = \frac{\Delta T_{d,1} + \Delta T_{d,2}}{2} \rightarrow c_d = \frac{c_{d,1} + c_{d,2}}{2} \tag{3.3}$$

and

$$\Delta T_a = \frac{\Delta T_{d,1} - \Delta T_{d,2}}{2} \rightarrow c_a = \frac{c_{d,1} - c_{d,2}}{2}. \tag{3.4}$$

The first term depends on crack depth, while the second to the angle. Both these parameters are spatial and temporal averages and so they are robust to experimental noise.

Regarding to the evaluation of the pipes, this aspect have been analyzed, focusing on the locally reduction of the wall thickness due to the corrosion. This phenomenon has to be accurately investigated to determine the remaining life of pipes. According to the statistics [36], indeed, it is the principal cause of more than 50% of the total accidents of leakage and explosion. Maldague appears to be the one of the first to perform infrared thermography testing of a small pipe in the laboratory. He has demonstrated in [37] the way in which pulse active infrared thermography is able to detect the wall thinning due to different flaws in elbow pipes. These kinds of pipe are strongly affected by the wall thickness due to turbulences and vortices taking place in large amount in them. Under transient conditions significant thermal contrasts are obtained in regions of the same pipe characterized by a different wall thickness. In this situation, as it is stated in section 1.1.1, a relation is established, connecting the depth *z* of the structure under investigation to the time *t* when the thermal contrasts appear on the front surface. It is important to highlight that *t* is counted from the start of the thermal perturbation: $t = \frac{z^2}{\alpha}$, where α is the thermal diffusivity of the material. According to this equation, if the surface of the pipe is damaged, the thermal disturbance reaches the outer surface after a time smaller with respect to the one spent in the sound areas. The measuring of the time *t* applied in this experiment is applied both in transmission and in reflection mode. In the first case, the temperature of the fluid circulating inside the tube is changed, obtaining a thermal transient, both in the hot to cold case and in the cold to hot situation. The infrared camera measures the temperature distribution of the outside surface in such a way that an evaluation of the remaining thickness is

allowed. Reflective method is applied in the case in which it is not possible to change the temperature of the circulating flow. A uniform heat flow is applied to the external surface of the pipe. The flow circulating inside the pipe has to be stopped. Due to the different thermal properties between the material of the tube and the circulating flow, thermal waves reach these surfaces at different times depending on wall thickness. The infrared camera records the surface temperature distribution in the outer surface of the pipe, detecting the wall thickness. Maldague, with this experiment, has demonstrated that the two different methods allow a correct detection of flaws in tube. The transmission mode has, also, the advantages to give a high thermal contrast and not to be affected by reflective noise, since the thermal variation is induced inside the pipe. In the last years, in [36], two Chinese researcher have followed the ideas and the procedures of Maldague [37], striving for a systemic investigation of this kind of problems. They have tested different flaws in different materials, such as stainless steel and carbon steel pipes. They have obtained that the minimum detectable flaw has a diameter of 6 mm and a depth of 1 mm for a stainless steel pipe, while it is a 10 mm diameter and 2 mm depth hole for the carbon steel tube. In this way they have proved that the testing sensitivity of the carbon steel is much smaller than the one of the stainless steel, accordingly to the assumption that a lower conductivity allows a higher sensitivity and a longer duration of the emerging of the defects. This last parameter has been proved to be affected also by the thickness of the wall. Making a comparison between three different type of carbon steels (Φ140x5, Φ168x16, Φ180x36), it is demonstrated that the thinner the wall, the longer the duration of defect emerging, respectively, 30 s, 120 s and 180 s, but the lower the testing sensitivity. In addition to this fact, it is found that the detecting sensitivity is higher with an inside heating with respect to the outside cooling. Another interesting study is made by some researcher of the Indian Institute of Technology [38]. A metal tube with possible wall thinning on its external surface have been investigated with the limitation that the inner part of the tube is the only accessible portion for line of sight inspection and that the infrared camera is located at the end of the tube. They exploit the *Pulse Thermography*. Two approaches are taken into account: the transmission mode, changing the temperature of the outer surface and observing the changes induced in the inner surface, and the reflection mode, based on both a change of temperature and an observation from the inner surface. High power flashes are used to heat the sample. For accessing the inner part of the tube, an aluminum reflector is utilized in such a way that it is able to reflect the surface emission of the tube's inner surface to the infrared camera placed at one end of the tube, as it is depicted in Figure 3.1 for the transmission mode.

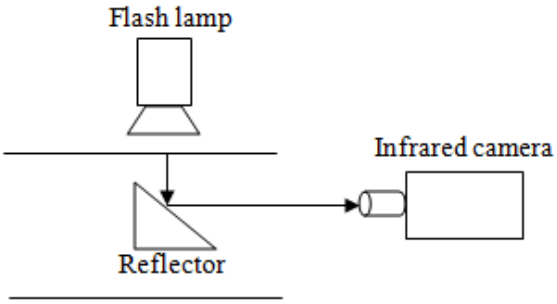

Figure 3.1: Outline of the proof with the aluminum reflector in the transmission mode.

The remaining thickness of the regions affected by different flaws is evaluated exploiting:

$$\alpha = \frac{0.48 * l^2}{\pi^2 t_x}, \tag{3.5}$$

where α is the thermal diffusivity, L is the thickness of the sample and the characteristics time t_x is evaluated considering a time-versus-temperature graph. This is the point where the straight line tangent to the time-temperature evolution line intercepts the time axis. This experiment has proved itself to be able both to detect and to accurately quantify different flaws in tube, with an error of 5.75%. In particular, this technique is able to detect defects as deep as one third of the total wall thickness or even more, with an error inferior to 0.5%. These results are obtained without the need of the camera to be inserted in the tube, an important improvement, since this is a significant issue in this kind of experiments.

Chapter 4
Experimental procedures

As it is stated in section 1.1.3, *Pulse Phase Thermography* has the goal to detect flaws under the surface of the sample under investigation and to characterize their size in terms of shape, dimension and depth. This objective can be reached through the analysis of the temperature of the sample of interest during the cooling stage, after the end of the heating stage. This inquiry requires, then, in addition to the purely experimental stage, also a particular post-processing stage. The specimen has to be heated and its surface emission has to be collected by a thermal imaging device during the cooling stage. With this last operation ends the experimental part. The post-processing stage starts with the proper calibration of the data collected by the infrared camera, in order to obtain the temperature of the surface of the sample. Then several elaborations are applied to them to characterize the flaws. The experimental set-up is made by some halogen lamps, by a Raytheon Radiance HS infrared camera and, obviously, by the sample with several flaws, characterized by different diameter sizes and located at different depth under the external surface of the specimen. Several parameters have to be set up during these stages: the heating time, the sampling frequency, the observation time and the appropriate calibration of the thermo-camera.

4.1 Experimental stage

4.1.1 Sample

The test has to simulate the behaviour of *Pulse Phase Thermography* method with cylindrical samples. For this reason, a hollow semicylindrical Plexiglas pipe is taken into account. Its inner and outer diameter measure, respectively, 130 mm and 150 mm; thus, its thickness is 10 mm. Several dummy holes are made on its inner surface, in such a way that they are located at a previously established depth under the external surface of the cylindrical sample. Their size is reported in Table 4.1. See Appendix C for details.

Table 4.1: Flaws on cylindrical sample.

Flaws characterization		
Number	Diameter [m^{-3}]	Depth [m^{-3}]
1	2	2
2	8	5
3	4	5
4	8	8
5	4	2

It is important to highlight that the external surface of the sample is coated with a black plaint, in order to reduce its reflectivity.

4.1.2 Heating stage

During the development of this work, the heating apparatus of the Thermal Lab has been improved. The old heating source was constituted by two halogen lamps, each one with an output power of 500 W, which were able to provide a-total power of 1000 W. The developed heating device is constituted by six halogen lamps, each one with a power of 500 W, located three at one side and three at the other side of the sample. They are contained in two wooden boxes, tilted by an angle of 45° with respect to the specimen. In this way this tool is able to provide an output power of 3000 W. In order to convey the maximum amount of power to the surface of the sample, each box is endowed with an aluminum paraboloid, located in the space between its wall and the lamps. More specifications on the building of this apparatus can be found in Appendix C. The sample is heated for 20 s, a time able both to excite the correct part of the frequency spectrum, as it is shown in section 2.4, and to lead the lamps to deposit an amount of energy in such a way that a ΔT between the defect and the sound area detectable by the infrared camera [22] [23] is guaranteed. In order to obtain a heating of the external surface as rectangular as possible, each box has a sash window, acting as a shutter mechanically connected to the box, which comes down at the end of the heating stage, physically insulating the lamps from the sample. In this way, it is able to abruptly stop the heat flux. It is, also, internally covered by an aluminum foil. In this way the spurious effects due to the transitory of the switching off of the lamps, still present even when the lamps are shut down, are minimized in such a way that their effects on the data acquired by the thermo-camera during the cooling stage are reduced as far as possible.
The experimental set-up is shown in Figure 4.1.

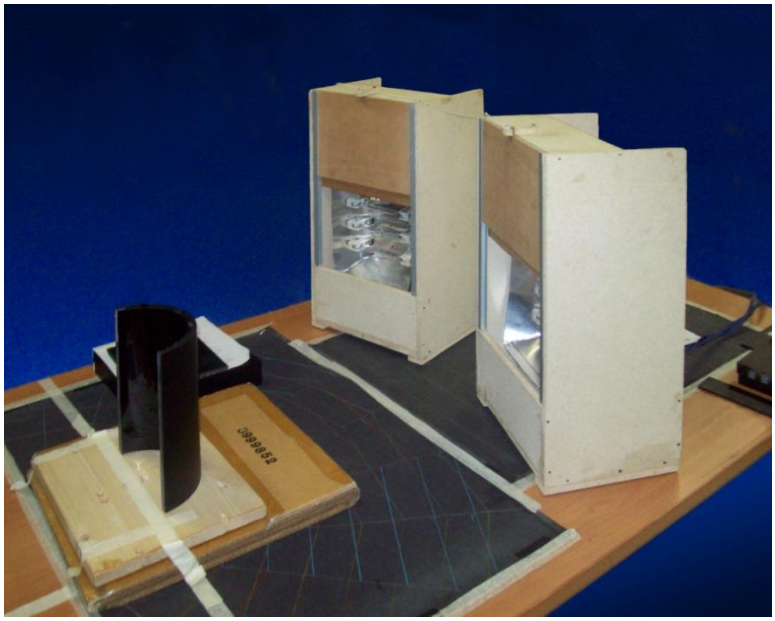

Figure 4.1: Experimental set-up.

4.1.3 Cooling stage

The acquisition of the emission of the external surface of the sample starts immediately after switching off the lamps. The sampling frequency and the observation time have to be accurately determined, since, as it is stated in section 1.1.3, the observation time determines the resolution in frequency:

$$\Delta f = \frac{1}{t_{observation}} \tag{4.1}$$

It is assumed to observe the sample for 1200 s, as in the previous works [22] [23], one measure for each second. This leads to a minimum detectable frequency of 8.3e-4 Hz. This value is the best compromise between the resolution in frequency and the memory required to the thermo-camera. On the other hand, the following formula:

$$\mu = \sqrt{\frac{\alpha}{\pi f}} \tag{4.2}$$

is the basis to identify the depth of the sample. Figure 4.2 shows the value of the estimated depth as a function of the frequency.

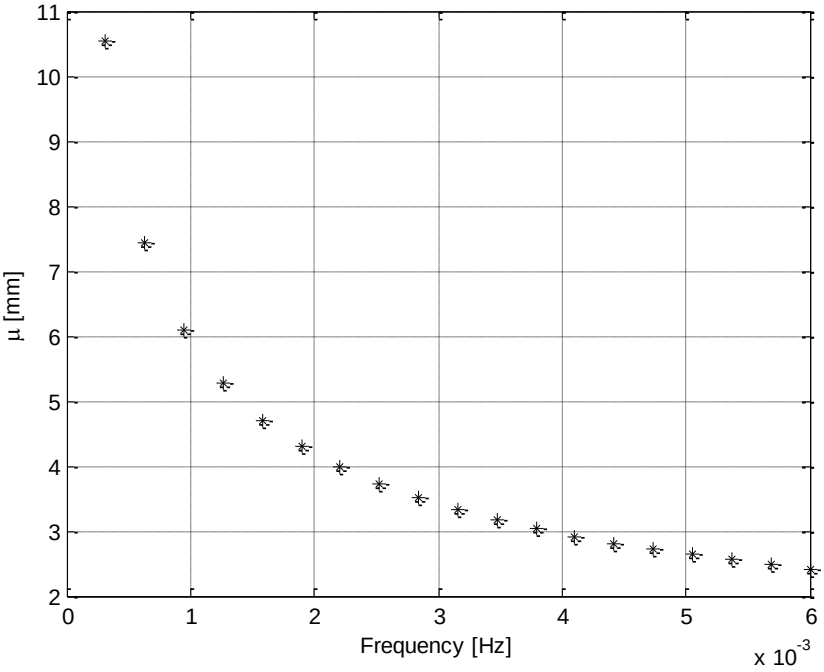

Figure 4.2: Thermal diffusion length.

To resume, the established experimental parameters are reported in the table below.

Table 4.2: Experimental parameters.

Stage	Parameter	Value
Heating	Heating time	20 s
Heating	Heating power	3000 W
Cooling	Observation time	1200 s
Cooling	Sampling frequency	1 Hz

4.2 Calibration procedures

4.2.1 Thermo-camera calibration

To obtain the temperature of the external surface of the sample, it is exploited the thermo-camera, that is an instrument that measures the radiation intensity of a body. This signal depends on the temperature of the body under investigation itself. The functioning of the Raytheon Radiance HS thermo-camera utilized in the ThermALab is based on a 256x256 matrix of sensors, located in the Focal Plane Array in such a way that each sensor gives as output the value of each pixel of the acquired image. In this way, once that the emissivity of the surface is known, a grey shade image of 256x256 pixels is obtained as output. The values of this grey scale vary from 1024 to 4096 divided in 768 tones (1 every four numbers). In the post processing stage, each value is associated to a different temperature, exploiting the biunique correspondence between the grey tones and the temperatures. This is possible thanks to the calibration of the thermo-camera. This procedure is carried on by acquiring a thermal image of a black body of known temperature; the obtained grey tone matrix is then biunivocally related to the measured temperature. The integration time is a fundamental parameter in order to obtain a correct detection of the temperature: the highest the integration time, the most precise the measure, but the lowest the maximum detectable temperature. The precedent works [20] [21] [22] [23] take into account an integration time of 0.1 s. It is very important to choose the thermo-camera parameters in such a way that they are able to fit in the best way the requirements of the problem. For this reason, during the development of this thesis work, this choice is checked, in order to select the value offering the best guarantees of calibration improvement and, consequently, leading to improved post-processing results. In order to choose the most appropriate integration time, several tests might be conducted. In this work, it is chosen an experimental set-up like the one that is going to be exploited for the determination of the directional emissivity of the sample. A rectangular aluminium box, 460 mm lengthwise, 100 mm breadthwise and 20 mm thick, externally coated with a black painting, is exploited. The experimental set-up is based on the thermo-camera, which registers the radiation intensity of the sample and on a thermostatic bath, which maintains a constant temperature of 41.5 °C. This instrument is connected to the box, hollow inside, by three input channels and three output channels. The thermo-controlled water of the bath flows inside the body through them, maintaining its temperature equal to the bath-imposed value, as it is depicted in Figure 4.3.

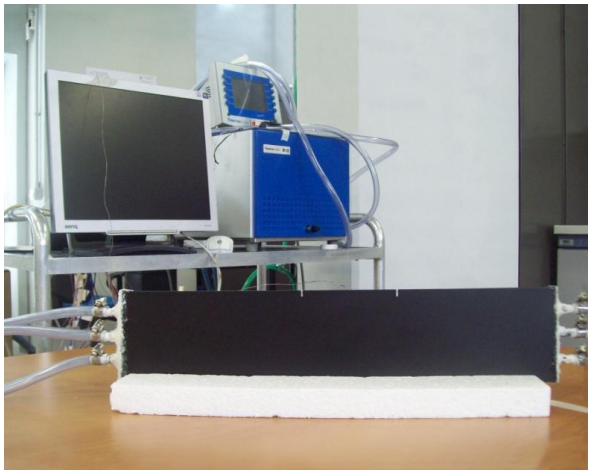

Figure 4.3: Thermostatic bath linked to the black sample.

The sample presents a small cavity, 1 mm lengthwise and 0.5 mm thick, where a miniaturized *type T* thermocouple is inserted, in order to measure the surface temperature [39]. After the reaching of the steady thermal condition, a first test with a ϑ of 0° is made. The box rotates on the axis passing through the probe of the thermocouple. In this way the thermocouple brings into focus always the same point, but the angle between this fixed observation point and the normal to the surfaces varies progressively: 0°, 45°, 0°, as it is can be seen in Figure 4.4 and in Figure 4.5. In this way it is possible to evaluate the behaviour of the thermo-camera also in a different position with respect to the usual one, characterized by a ϑ of 0°.

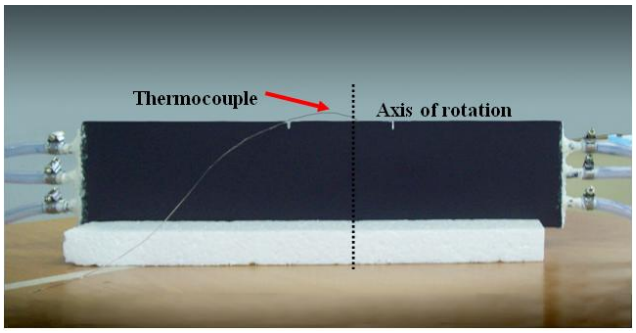

Figure 4.4: Black sample, test at a fixed temperature.

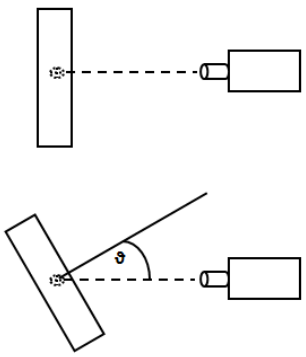

Figure 4.5: Outline of the test on the black sample.

The test campaign starts and finishes with a survey of the temperature of the sample orthogonal to the thermo-camera. In this way is verified the repeatability of the proofs and the independence from the environmental condition. The temperature of the aluminium box previously described is recorded with

different integration times of the thermo-camera. The first term of comparison is the minimum available integration time: 0.1 s, with which a temperature until 80 °C can be detected [39], the one utilized in the previous works [22] [23]. The sample is always connected to the thermostatic bath, whose temperature is maintained constant at 41.5 °C, which is, as a consequence, the maximum value the thermo-camera has to identify in this case. For this reason it is chosen as a second term of comparison an integration time of 0.25 s, which leads to a maximum detectable value of around 55 °C. In this way, the thermo-camera is able to correctly detect the temperature of the box, without saturation occurring in a quite wide range (from 41.5 °C to 55 °C), as it is demonstrated in [39]. It is important to highlight that the thermo-camera acquires one image each 100 ms: during the test, the thermocouple takes 7 values, while 700 frames are acquired by the thermo-camera. For this reason, in the post processing process first of all each pixel is mediated temporally on the 700 images; in this way it is obtained a single averaged 256x256 pixels matrix, subsequently divided in several sub-areas on which different spatial averages are conducted.

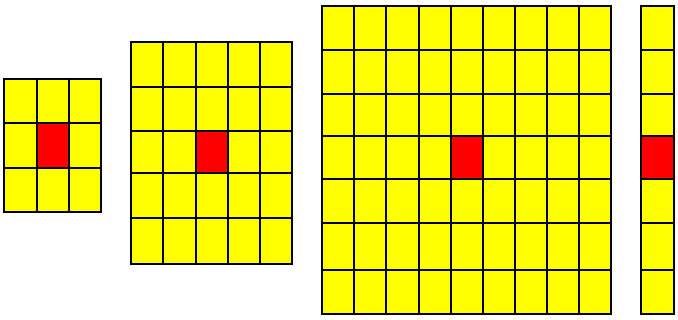

Figure 4.6: Analyzed areas around the thermocouple, squared regions.

In Figure 4.6 an example of these areas under investigation is depicted: the average is made on seven different zones. The first one is the whole sample; afterwards three different squared areas of pixels around the thermocouple are taken into account: 3 by 3, 5 by 5, 9 by 9; lastly, three vertical regions centred on the thermocouple are analyzed: these are one column, 5 columns and 9 columns wide. Regarding the thermocouple, instead, a first average is done considering only the values obtained during the test; another examination takes into account also values recorded before the start and after the end of the test, in order to better evaluate the behaviour of this instrument.
Table 4.3 and Table 4.4 show the results. It is important to highlight that 0.1 s and 0.25 s in the part referred to the thermocouple are related to the measures done when the thermo-camera makes the tests with these two different integration times.

Table 4.3: Standard deviation, squared regions of pixels, 0°.

0°				
	0.1s		0.25s	
Thermocouple				
	T [°C]	St.Dev. [°C]	T [°C]	St.Dev. [°C]
7 values	41.45	0.01	41.45	0.008
20 values	41.44	0.01	41.45	0.009
Thermo-camera				
	T [°C]	St.Dev. [°C]	T [°C]	St.Dev. [°C]
Thermocouple point	42.42	-	41.50	-
Total	42.30	0.18	41.49	0.04
3by3	42.34	0.17	41.43	0.03
5by5	42.38	0.16	41.45	0.02
9by9	42.36	0.16	41.45	0.02
Column	42.31	0.15	41.47	0.03
3 Columns	42.31	0.16	41.47	0.03
5 Columns	42.30	0.18	41.47	0.03

Table 4.4: Standard deviation, squared regions of pixels, 45°.

45°				
	0.1s		0.25s	
Thermocouple				
	T [°C]	St.Dev. [°C]	T [°C]	St.Dev. [°C]
7 values	41.51	0.02	41.42	0.01
20 values	40.51	0.02	40.42	0.01
Thermo-camera				
	T [°C]	St.Dev. [°C]	T [°C]	St.Dev. [°C]
Thermocouple point	42.16	-	41.26	-
Total	41.95	0.22	41.19	0. 09
3by3	42.03	0.18	41.14	0.03
5by5	41.99	0.19	41.15	0.02
9by9	41.99	0.19	41.15	0.02
Column	41.98	0.22	41.15	0.06
3 Columns	41.98	0.23	41.15	0.06
5 Columns	41.98	0.23	41.15	0.06

The average values given by the thermocouple do not change in a significant way with respect to the number of measures considered. Also the standard deviation is almost unchanged between the different means. Its low value guarantees the accuracy of the considered average.
Regarding the thermo-camera, first of all, it is important to highlight that a check is made in order to verify whether the test has been correctly conducted and whether it is repeatable. The two measurements at 0° are compared. Table 4.5 shows the ratio between the averaged temperatures in the different areas of interest: they are quite similar, their ratio is close to 1. Another check is conducted taking into consideration the temperature distribution of the two different measures. As it is depicted in Figure 4.7 and in Figure 4.8, also in this case the test reveals itself to be repeatable. It can be easily noticed that a greater integration time implies a more precise value, while the difference between the temperature detected by the thermo-camera and the one identified by the thermocouple increases with a smaller integration time. Focusing on the standard deviation, it can be seen that an integration time of 0.25 s guarantees a more accurate measure: its value is always lower with respect to the other integration time.

Table 4.5: Comparison between two measurements at 0°.

	Ratio between temperature $\frac{\text{T part 2}}{\text{T part 1}}$	
	0.1 s	0.25 s
Total	0.9994	0.9998
3by3	0.9990	0.9999
5by5	1.0000	0.9997
9by9	0.9995	0.9996
Column	0.9993	1.0009
2 Columns	0.9994	1.0007
5 Columns	0.9996	1.0008

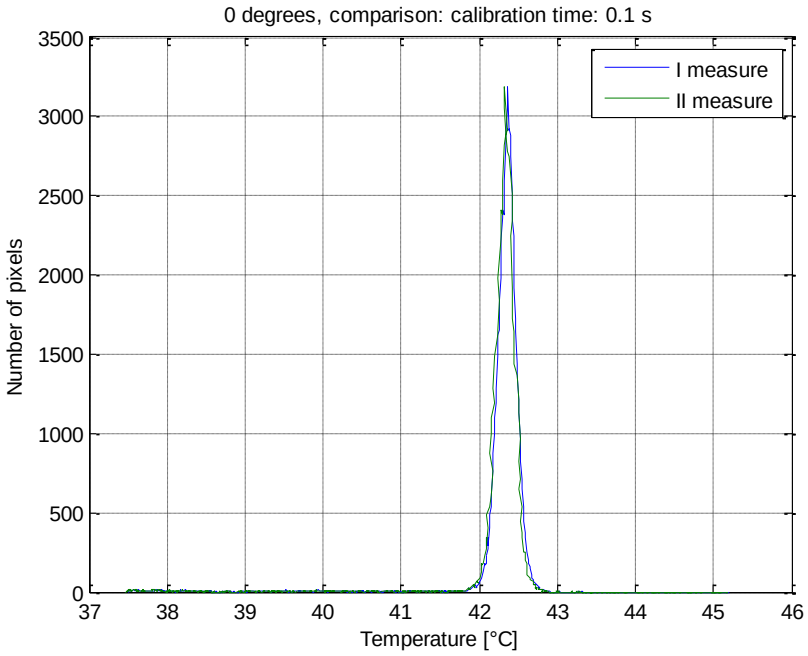

Figure 4.7: Comparison 0 degrees, calibration time 0.1 s.

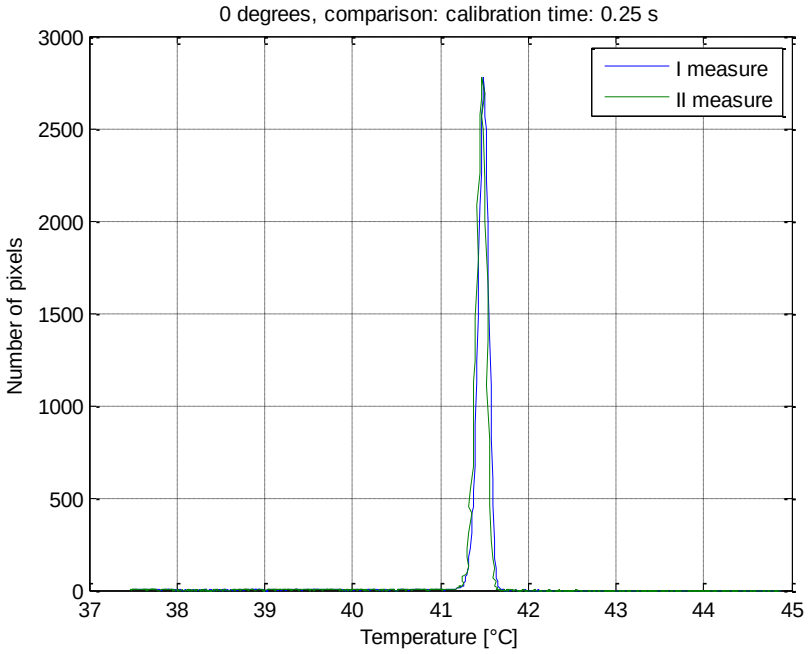

Figure 4.8: Comparison 0 degrees, calibration time 0.25 s.

4.2.2 Thermocouples calibration

The thermocouples utilized in this work are the same exploited by Fustinoni [39]. These instruments have been calibrated exploiting the thermostatic bath. When the thermostatic bath has reached the imposed value of temperature, for each thermocouple are acquired 160 values, one each 15 seconds. The calibration point is the mean value of such measures. It is important to highlight that the standard deviation is inferior to 0.02 °C.

4.3 Post-processing stage

Once that the integration parameter of the thermo-camera is set, the data acquired by the thermo-camera are elaborated to obtain the temperature, exploiting the calibration curve. Then several procedures are required for a correct analysis.

4.3.1 Filtering and morphological operations

The acquired images require a particular filtering operation, to limit the noise that, otherwise, could make unserviceable the data. Noise could be caused by unevenness of the sample surface, by spurious reflection of the environment light, by a non-uniform answer of the infrared instrument on the frequency spectrum. To limit these spurious effects, the test is conducted turning off the light of the laboratory. Also the black coating of the sample, characterized by a high emissivity and a low reflectivity, helps in reducing the noise. Thus, a median filter, with a 3x3 Kernel mask, is applied to the images. The phase analysis is also able to limit the effects caused by a non-uniformity in the heating and of emissivity. Figure 4.9 and Figure 4.10 show the comparison between a filtered and a non filtered thermogram. For the sake of completeness, the phase difference at the centre of the flaw given by the data obtained before and after the application of the filter in the experimental results is depicted for the flaw with a diameter of 8 mm and a depth of 5 mm. As it can be seen, the applied filter reveals itself to be effective in the elimination of the spurious data.

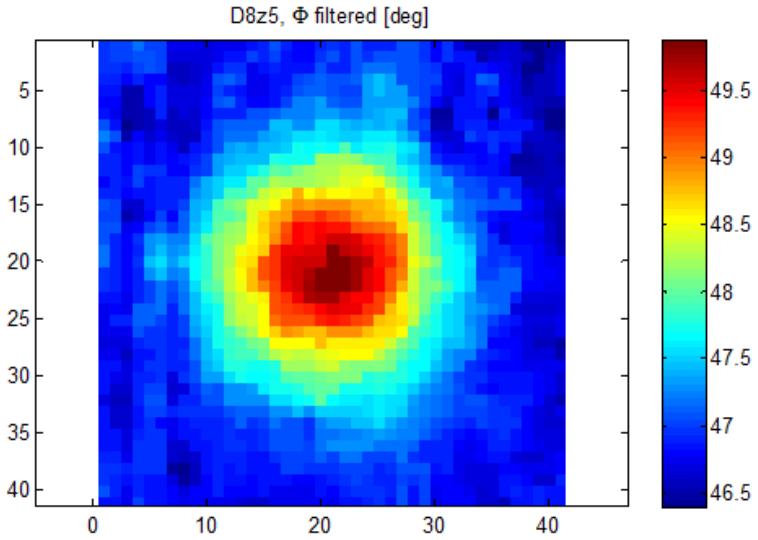

Figure 4.9: Filtered phase of the thermogram referred to D8mm,z5mm flaw, third frame.

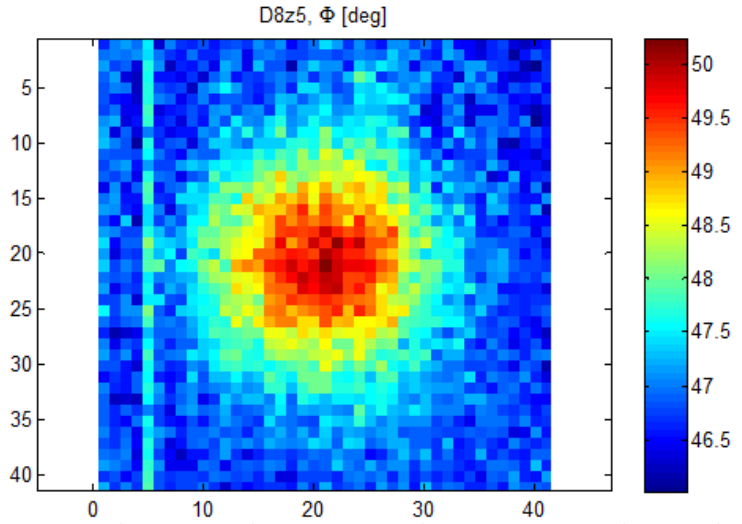

Figure 4.10: Non-filtered phase of the thermogram referred to D8mm,z5mm flaw, third frame.

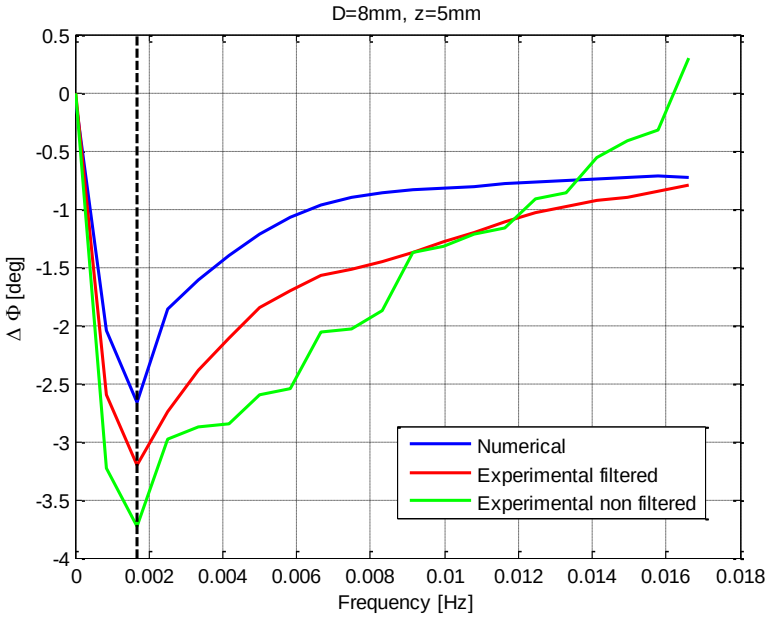

Figure 4.11: Phase difference, D8z5, numerical, experimental (Φ), experimental (Φ filtered).

After that the images are filtered, morphological reconstruction is applied. This method is the same exploited in the previous works, [22], [23], [40], based on the evaluation of local minimum and maximum and on operations of dilation and erosion, able to distinguish the zone of the flaw from the unaffected zones.

4.3.2 Depth characterization

To characterize the depth of each flaw, it is exploited the criterion of the optimum visibility frequency, as in the previous works, [22], [23], [40]. To determine this value, the statistic correlation concept is utilized. In the case of the correlation between two images, as the analyzed one done with the phase images, the correlation value is defined as:

$$r(A,B) = \frac{\sum_{i=1}^{rows}\sum_{j=1}^{columns}(A_{ij}-\overline{A})(B_{ij}-\overline{B})}{\sqrt{\left(\sum_{i=1}^{rows}\sum_{j=1}^{columns}(A_{ij}-\overline{A})^2\right)\left(\sum_{i=1}^{rows}\sum_{j=1}^{columns}(B_{ij}-\overline{B})^2\right)}}. \quad (4.3)$$

where $\overline{A}$ and $\overline{B}$ are the mean of the values of each image. Each phase image is then correlated with the following one, obtaining a *R* function, whose maximum corresponds to the optimum visibility frequency. Exploiting formula 4.2, the estimated found is then obtained.

4.4 Experimental issues

The principal aim of this thesis is the characterization of flaws in objects in special configuration with respect to the heating source or to the thermal imaging system. Due to the complexity of this problem, several aspects have to be carefully taken into account: the analysis has to deal with several problems, principally related to the curvature of the sample.

4.4.1 Directional emissivity

As stated before, one of the aims of this work is the inquiry of defects in elements non orthogonal to the observation direction. So, the directional spectral intensity has to be carefully evaluated in order to characterize the behaviour of the surfaces under investigation. Directionality is, indeed, an important feature of the thermal radiation. The surfaces can emit in the same way in all directions, or their emission may assume different values according to the direction under analysis, as it is depicted in Figure 4.12. Calling ϑ the angle between the normal to the surface and the observation direction, it can be seen that, in the case of a directional surface, in general the maximum value of the spectral intensity occurs when ϑ is equal to 0°, while, when ϑ increases, this value rapidly decreases, approaching zero when ϑ is equal to 90°. On the other hand, in the case of a sample acting as a black body, the spectral intensity is constant and independent of direction [13].

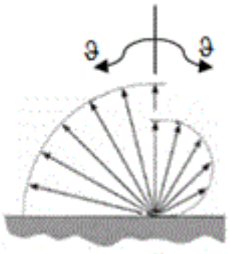

Figure 4.12: Comparison between different directional distribution of the surface emission. [13].

In order to preliminarily evaluate the behaviour of the cylindrical sample with respect to this feature, a test is done exploiting the same experimental set-up of the test regarding the calibration of the infrared instrument: also in this case, the thermocouple measures the temperature of the sample and the thermo-camera acquires an images every 100 ms. The post-processing stage starts applying the calibration corresponding to an integration time of 0.25 s and a median filter to eliminate the crazy pixels. Then each pixel is temporally averaged obtaining the corresponding averaged 256x256 pixels matrix. In order to obtain useful

information, the proper solution is to make a spatial average on this matrix. This mean is conducted considering different squared areas of pixels, respectively with a side of 2, 3, 5, 9 and 21 pixels. In particular, for each one of these values, the matrix is subdivided in several squares with such dimension, each one centred on a pixel of the matrix. In this way it is applied a sort of squared mask, moving in such a way that it is able to take into account the values on the whole matrix, as it is depicted in Figure 4.13.

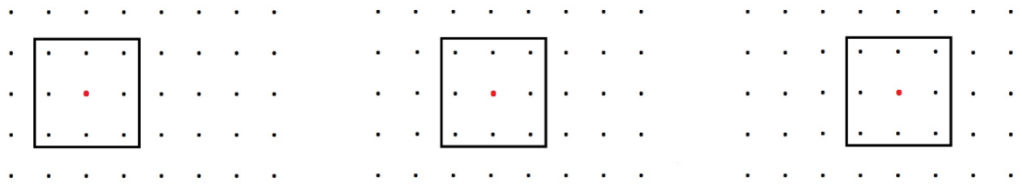

Figure 4.13: Regions on which the mean is conducted, proof at fixed temperature.

A spatial mean is then conducted on each square, in such a way that several matrices containing averaged values are obtained. Each matrix obtained with this procedure is averaged again, obtaining the analyzed mean value.

The mean value, obtained with the procedure explained before, is close to the one of the thermocouple. This is demonstrated also by the distribution of the temperature, a Gaussian curve with a peak around the mean value. To give an example, Figure 4.14 and Figure 4.15 show this curve for the measure at 0° and at 30°.

Table 4.6: Temperature, squared regions of pixels.

Squared regions of pixels					
	0°	30°	45°	60°	75°
	T [°C]	T [°C]	T [°C]	T [°C]	T [°C]
Total	41.49	41.33	41.19	40.81	39.39
2by2	41.49	41.33	41.19	40.81	39.39
3by3	41.49	41.33	41.19	40.81	39.39
5by5	41.49	41.33	41.19	40.81	39.39
9by9	41.49	41.33	41.20	40.81	39.39
21by21	41.49	41.33	41.20	40.81	39.39

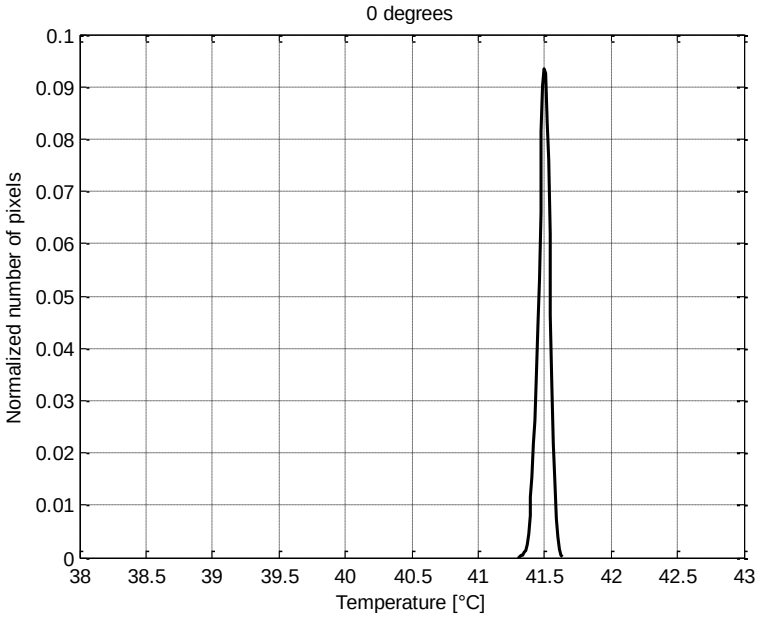

Figure 4.14: Distribution of temperature, 0 degrees.

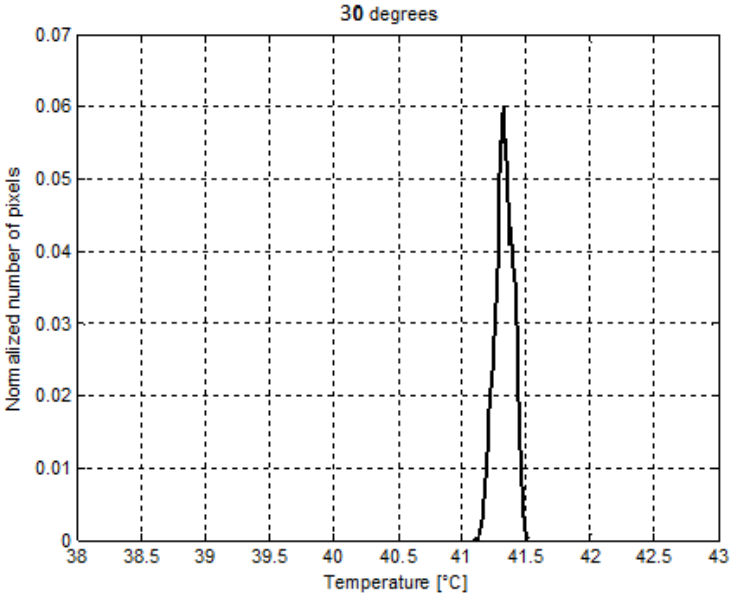

Figure 4.15: Distribution of temperature, 30 degrees.

Figure 4.16 and Figure 4.17 show the ratio of the measures of the averaged temperature taken at 30°, 45°, 60° and 75° on the one at 0°: the considered zones are the whole sample, the 2x2, 9x9 and 21x21 regions around the thermocouple.

It can be easily noticed that the averaged values are quite similar to the ones at 0°; indeed their ratio is close to 1. When the angle increases, this value tends to become smaller than 1. So, the radial emission of this surface is not independent by the angle of observation: the closest the angle to 0°, the smallest the difference between them and the emission at 0°.

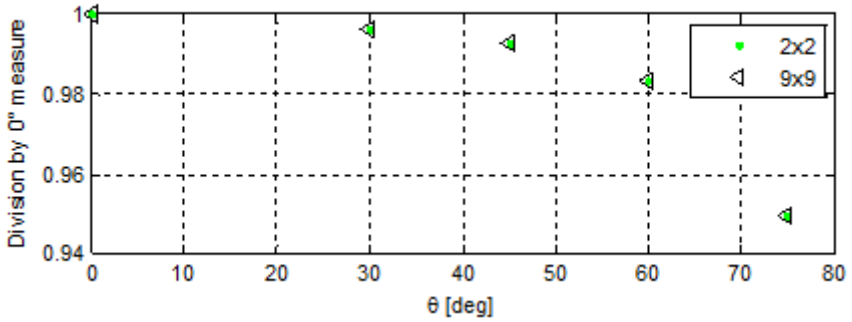

Figure 4.16: Comparison with respect to 0 degrees measurements, 2x2 and 9x9 pixels side, squared region.

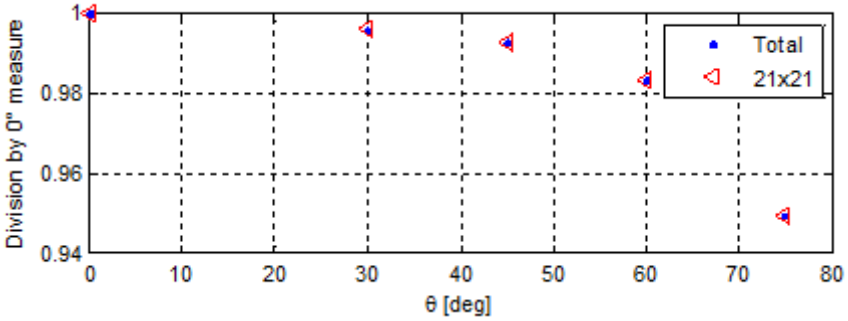

Figure 4.17: Comparison with respect to 0 degrees measurements21x21 pixels side squared region and total.

Since no significant changes are introduced taking into consideration different regions of the sample, it is chosen to take as a reference the values obtained by analyzing the whole sample, for the sake of completeness.
According to the results obtained up to now, it is possible to evaluate the effects of the variation of the emissivity angle of the sample. As it is stated before, the variations of the measured temperature are small until the angle is inferior to 60°, but they are going to increase when the angle grows up. In order to establish a relation able to be suited to this behaviour, as a first approximation, it is exploited the *Lambert's law*. It states that the radiant intensity of a *Lambertian* surface depends on the cosine of angle between the line of sight of the observation point and the line normal to the surface:

$$I_\vartheta = I_n \cos(\vartheta). \qquad (4.4)$$

Assuming that

$$I = \sigma T^4, \tag{4.5}$$

it is obtained that

$$\sigma T_\vartheta^4 = \sigma T_n^4 \cos(\vartheta) \rightarrow T_\vartheta^4 = T_n^4 \cos(\vartheta) \tag{4.6}$$

This relation is an ideal one, which is not able to capture exactly the behaviour of the analyzed specimen, which is not classifiable as a *Lambertian* surface, since its radiant intensity has not a strong dependence on the angle, such the ones theorized in the law. Thus, it is decided to make a comparison with the fourth root of the temperature at each analyzed angle of sight and the ones taken with an observation angle of 0°.
The obtained values are, thus, interpolated in order to find the general trend for any value of the inclination angle.

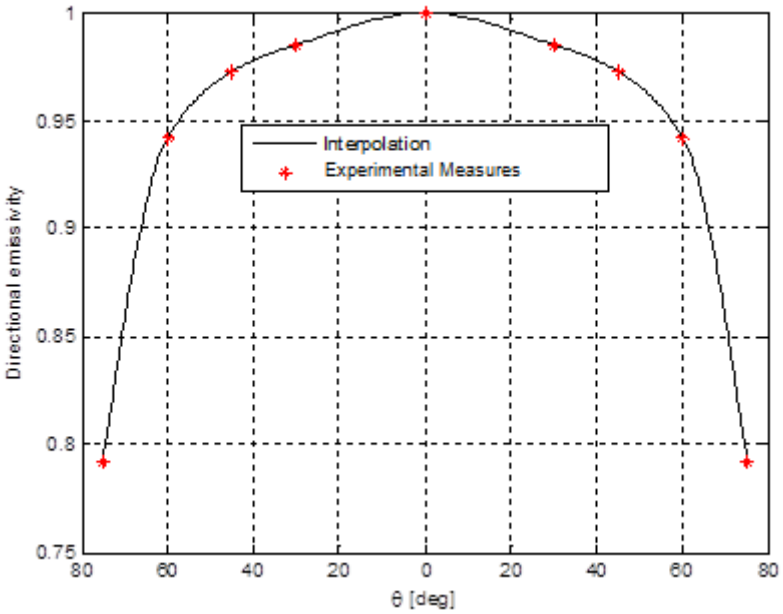

Figure 4.18: Interpolation of the emissivity values.

4.4.2 Out-of-focus effects

Another important issue, the sample under investigation requires, is related to the out-of-focus effects. This is due to the fact that each point, due to the curvature of the surface of the specimen it belongs to, is characterized by a different distance from the infrared camera. It is, thus, important to understand how the zones not perfectly brought into focus by the thermo-camera behave. For this reason, in addition to the rectangular zones previously analyzed, also

rectangles made up of 15, 21 and 31 columns around the thermocouple are considered in the analysis. In this way, indeed, it is possible to carry out an evaluation of the behaviour of the pixels characterized by an increasing distance from the thermocouple, which is the point that should be always into focus, since the sample is rotated around it. For a deeper investigation, for each one of the rectangles of columns both the whole columns and a smaller region of pixels around the thermocouple are analyzed: 3, 11, 21 and 31 pixels. Figure 4.19 shows the comparison between the region closest to the thermocouple and the further ones: the ratio between the measures taken at 30° and at 0° is the closest to 1; it tends to decrease when the angle grows up, remaining limited.

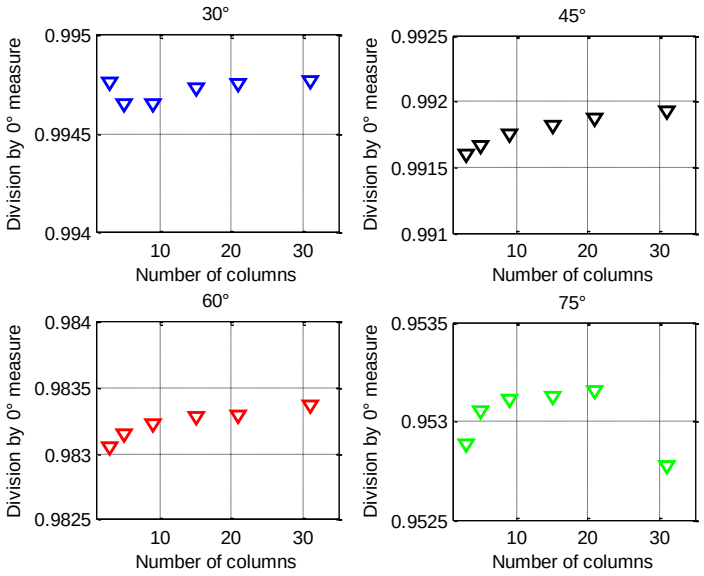

Figure 4.19: Comparison between different columns.

Table 4.7: Temperature, different regions of pixels, 0°.

Rectangular region					
0°					
	Total T [°C]	3 pixels T [°C]	11 pixels T [°C]	21 pixels T [°C]	31 pixels T [°C]
1 column	41.47	-	-	-	-
3 column	41.47	41.46	41.46	41.46	41.46
5 column	41.47	41.46	41.46	41.46	41.46
9 column	41.47	41.46	41.46	41.46	41.47
15 column	41.47	41.47	41.46	41.47	41.47
21 column	41.47	41.47	41.46	41.47	41.47
31 columns	41.46	41.47	41.47	41.47	41.47

Table 4.8: Temperature, different regions, 30, 45° and 60°.

Rectangular region					
30°					
	Total T [°C]	3 pixels T [°C]	11 pixels T [°C]	21 pixels T [°C]	31 pixels T [°C]
1 column	41.29	-	-	-	-
3 column	41.29	41.28	41.28	41.28	41.28
5 column	41.28	41.28	41.28	41.28	41.29
9 column	41.28	41.29	41.29	41.29	41.29
15 column	41.28	41.29	41.29	41.29	41.29
21 column	41.28	41.29	41.29	41.29	41.29
31 columns	41.28	41.29	41.29	41.29	41.30
45°					
	Total T [°C]	3 pixels T [°C]	11 pixels T [°C]	21 pixels T [°C]	31 pixels T [°C]
1 column	41.15	-	-	-	-
3 column	41.15	41.17	41.17	41.17	41.17
5 column	41.15	41.17	41.17	41.17	41.17
9 column	41.16	41.17	41.17	41.17	41.17
15 column	41.16	41.17	41.17	41.17	41.17
21 column	41.16	41.17	41.17	41.17	41.17
31 columns	41.16	41.17	41.18	41.17	41.18
60°					
	Total T [°C]	3 pixels T [°C]	11 pixels T [°C]	21 pixels T [°C]	31 pixels T [°C]
1 column	40.79	-	-	-	-
3 column	40.80	40.81	40.81	40.81	40.81
5 column	40.80	40.81	40.81	40.81	40.81
9 column	40.80	40.81	40.81	40.81	40.81
15 column	40.81	40.81	40.81	40.81	40.81
21 column	40.81	40.81	40.81	40.81	40.81
31 columns	40.81	40.81	40.81	40.81	40.81

Table 4.9: Temperature, different regions, 75°.

Rectangular region					
75°					
	Total T [°C]	3 pixels T [°C]	11 pixels T [°C]	21 pixels T [°C]	31 pixels T [°C]
1 column	39.54	-	-	-	-
3 column	39.54	39.55	39.55	39.55	39.55
5 column	39.55	39.55	39.55	39.55	39.55
9 column	39.55	39.55	39.55	39.55	39.55
15 column	39.55	39.55	39.55	39.55	39.55
21 column	39.56	39.55	39.55	39.55	39.55
31 columns	39.54	39.55	39.55	39.55	39.56

Table 4.7 shows the results for the measure taken at 0°. In this condition the sample is completely brought into focus by the thermo-camera. With this configuration any contingent difference in the measured temperature should not be ascribed to this issue. As it can be seen, the maximum difference between the values is 0.01°, inferior to the tolerance of the thermo-camera and, in addition to this fact, the maximum value of the standard deviation is 0.04°, as Appendix A shows. As a consequence, all the points belonging to the sample in this configuration are assumed to be at the same temperature. This result has a twofold consequence. First of all, the thermostatic bath reveals its effectiveness in maintaining the whole sample at a fixed temperature and, for an inclination angle equal to 0°, each point of the sample is proved to be characterized by the same value of emissivity. Analyzing the values taken at different angles of rotation, the results reveal how the measure deals with the out-of-focus effects. Considering Table 4.8 and Table 4.9 the maximum standard deviations are, respectively, 0.06°, 0.07°, 0.07° and 0.11°. These low values guarantee that it is possible to make an analysis on the mean of each zone, rather than on each single value. Since the difference between the measures is inferior to the tolerance of the infrared instrument, it is assumed that no significant changes are induced by the out-of-focus effects, assuming that the analyzed effect is negligible.

4.4.3 Non-uniform heating

As it is stated in [41], the effect of a non-uniform heating has to be taken accurately into account. The case under investigation has to widely deal with this aspect, since its surfaces experiment hardly the same amount of incident energy. In order to analyze the effects of this different thermal response, a test is conducted, heating a sample in different positions with respect to the sources of heating: its surface temperature is analyzed when the angle between it and the lamp is 0°, 30°, 45°, 60° and 75°. The squared sample, with a side of 200 mm and a thickness of 20 mm, is externally treated in order to obtain an object which represents a reasonable approximation for a black body, as in the case described in section 4.2. In this way the difference in the temperature registered by the thermocouples is connected only to the effect of the heating and not to a different directional emission of the body. The experimental set-up comprises the volt-ohm-milliammeter and four *type T* thermocouples, three located onto the superior surface of the sample and one which measures the temperature of the environment. In this way it is possible to measure the surface temperature in areas that should be subjected to a different heating in three specific points. In addition to this fact, another test is made regarding the emission of the sample, since the test is conducted rotating the sample around its centre, maintaining the lamps in a fixed position, as it is shown in Figure 4.21 and in Figure 4.22. Figure 4.20 shows the experimental set-up of the sample.

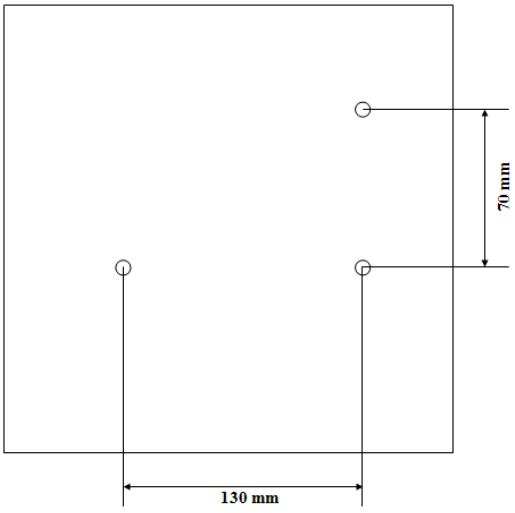

Figure 4.20: Outline of the sample with the thermocouples.

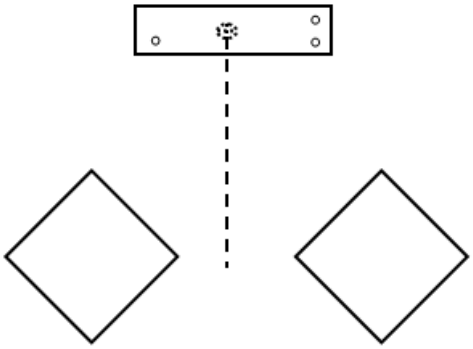

Figure 4.21: Outline of the test regarding the non uniform heating, 0°.

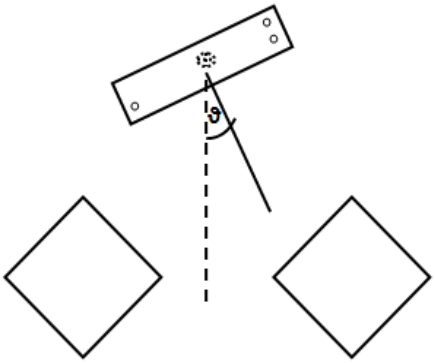

Figure 4.22: Outline of the test regarding the non uniform heating, ϑ°.

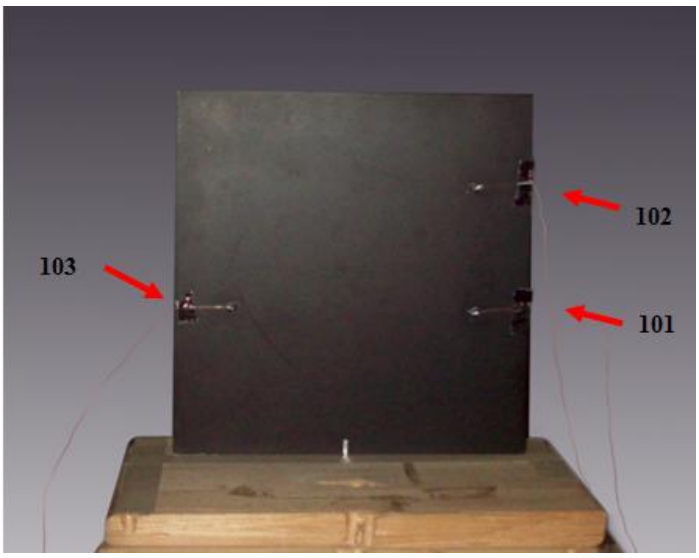

Figure 4.23: Outline of the test regarding the non uniform heating.

First of all, a 0° angle is considered, heating the sample for 90 s. In this way it is possible to study the thermal response of the object, finding the optimal heating time, which involves a variation in the temperature of the body significant for the following analyses: this value is set to 40 s, implicating a ΔT of 10 degrees. Other two tests at 0° are conducted, both to evaluate whether the optimal heating time found before implies the same increment of temperature and to understand if the experiment is repeatable. Another validation of the independence of the measures from the environmental conditions is done considering two different measures of the temperatures at 45°. It is important to highlight that the measures obtained by the thermocouples are significantly

influenced by the temperature of the environment. In order to make a comparison among these values, the temperature of the environment is subtracted from each measure, before doing the analysis. Figures from Figure 4.24 to Figure 4.31 confirm this aspect.

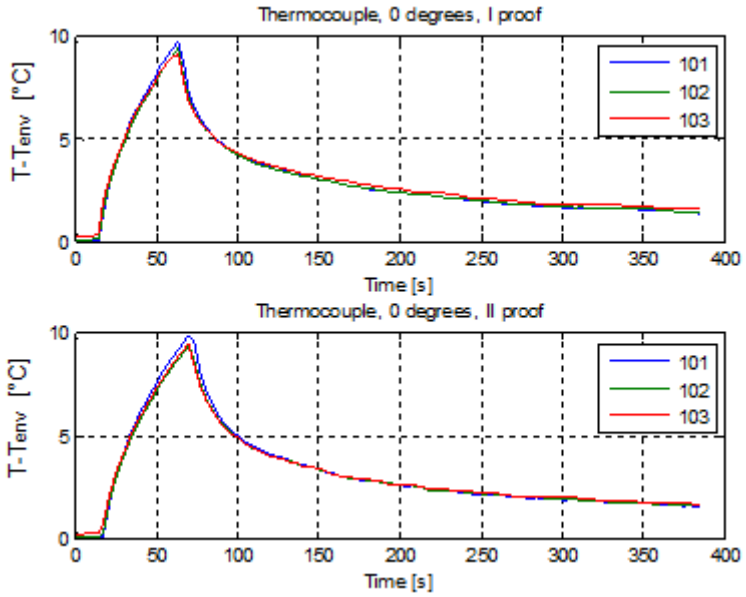

Figure 4.24: Thermocouples, comparison, 0°.

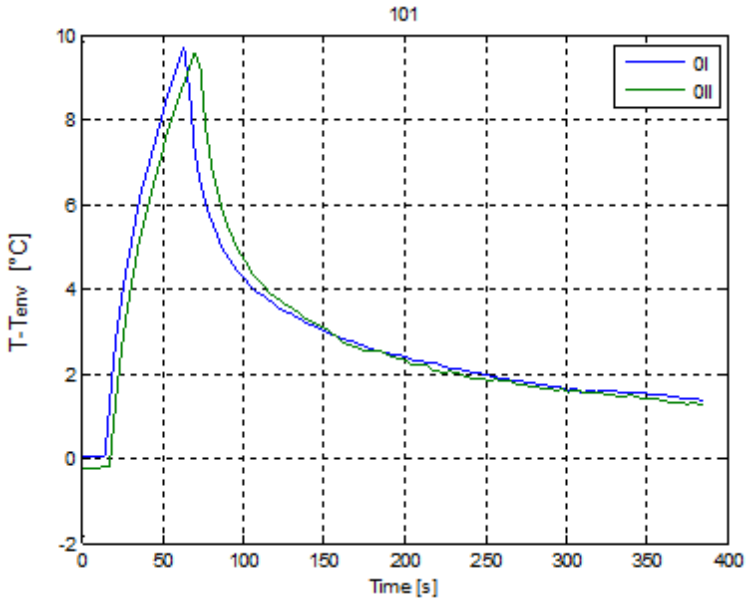

Figure 4.25: Thermocouples, comparison 0°, 101.

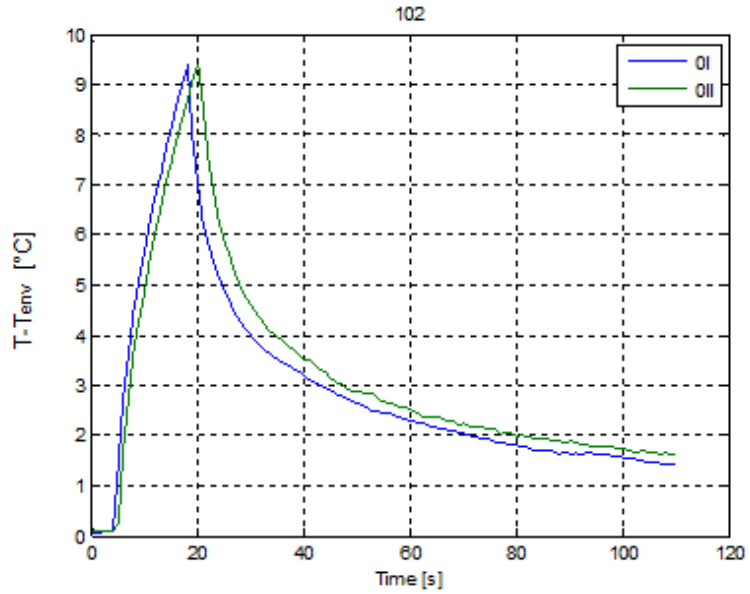

Figure 4.26: Thermocouples, comparison 0°, 102.

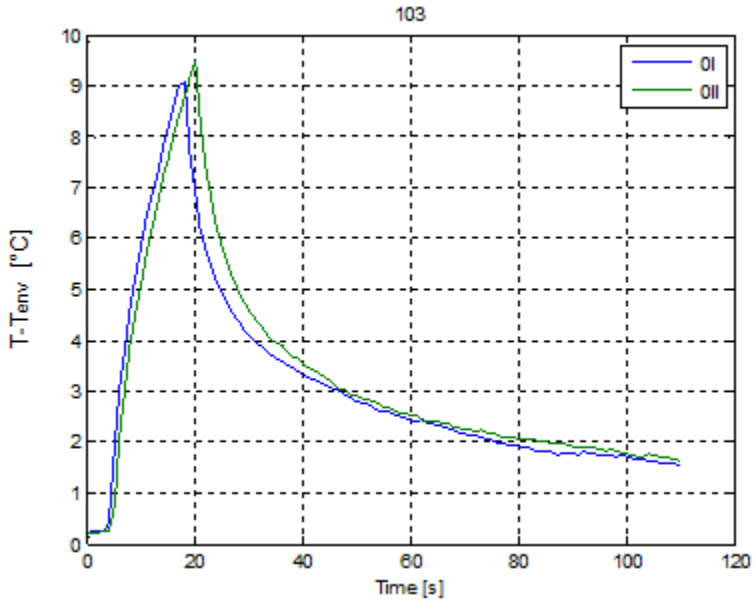

Figure 4.27: Thermocouples, comparison 0°, 103.

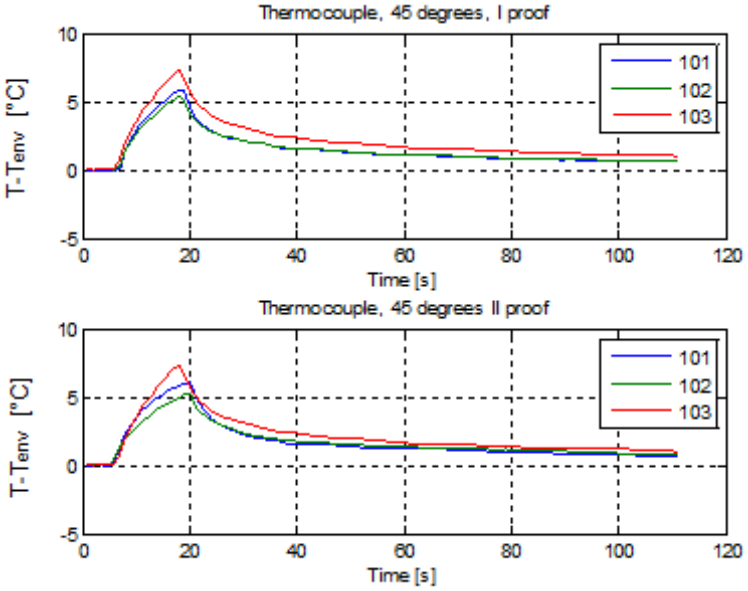

Figure 4.28: Thermocouples, comparison, 45°.

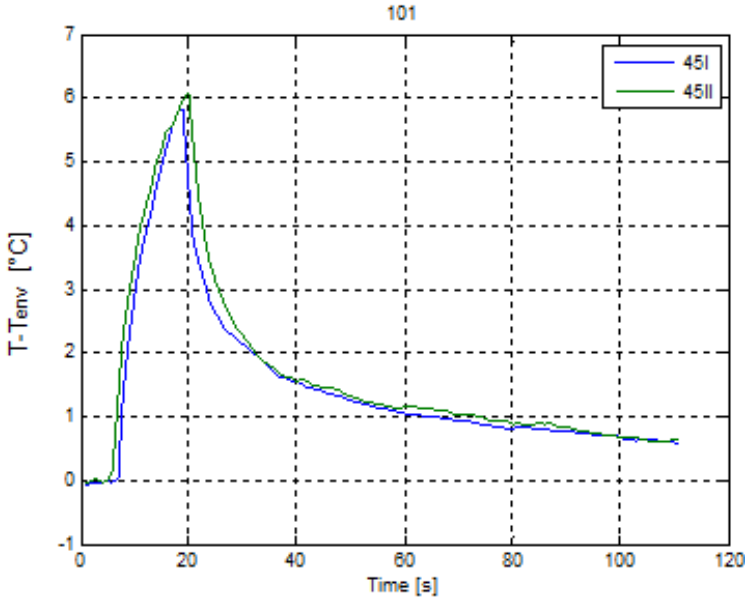

Figure 4.29: Thermocouples, comparison 45°, 101.

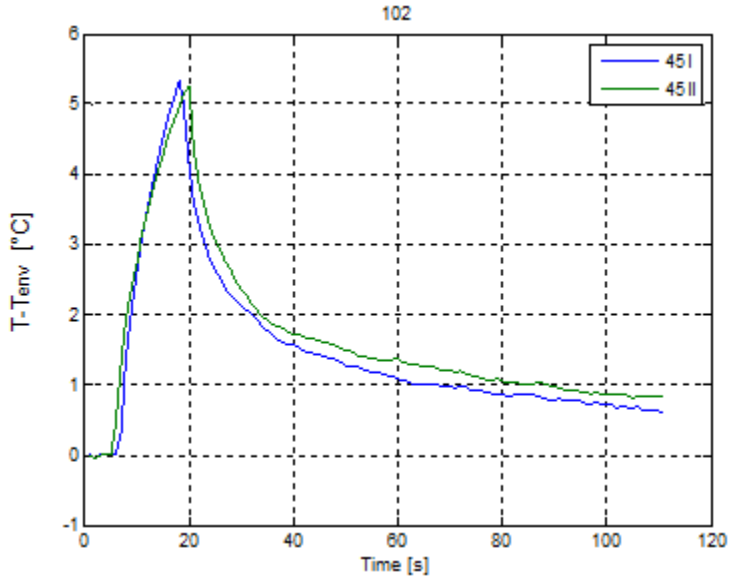

Figure 4.30: Thermocouples, comparison 45°, 102.

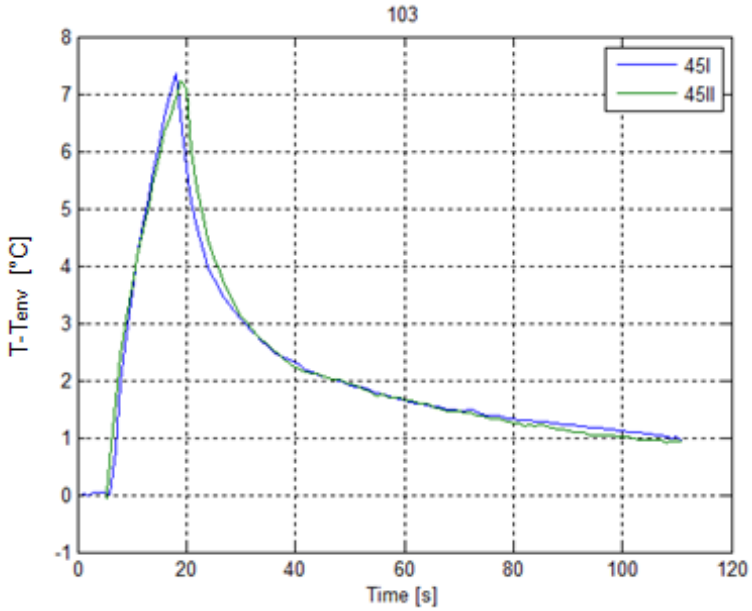

Figure 4.31: Thermocouples, comparison 45°, 103.

Then several tests with a heating time of 40 s are conducted. Figure 4.32-4.34 show the trend of the temperature for different degrees of inclination, once that the environment offset is removed. As it can be seen, a non-uniform heating involves a difference of 6 °C in the temperatures. In addition to this fact, it could be easily detected that, with the experimental set-up described in Figure 4.21

and in Figure 4.22, the left side of the sample is irradiated in a more uniform way: in the 103 thermocouple, the difference between the measure taken at 0° and the other measures has always a lower value with respect to the same differences found out in 101 and 102 thermocouples. In particular, the temperature of 103 can be approximated with its value at 0° for the test at 30°. As the angle increases, the difference increases, still remaining lower with respect to 101 and 102. The bottom right corner of the object is irradiated in the worst way.

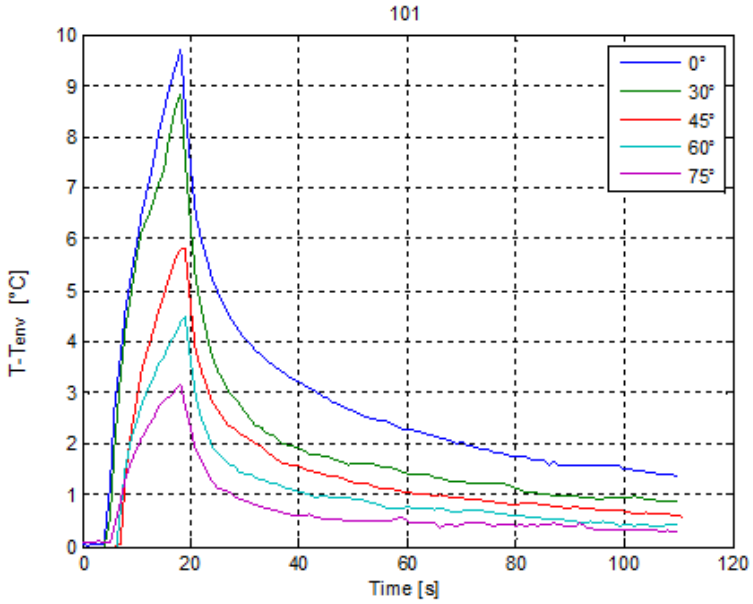

Figure 4.32: Thermocouple, comparison, 101.

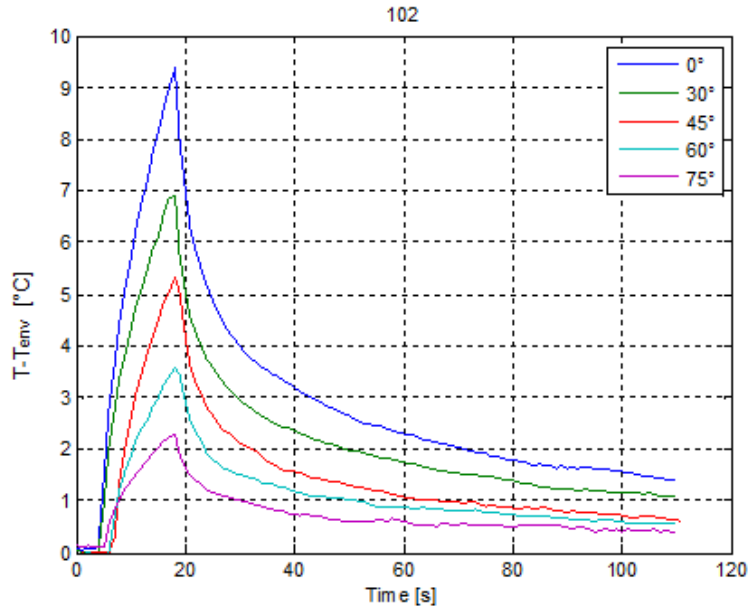

Figure 4.33: Thermocouple, comparison, 102.

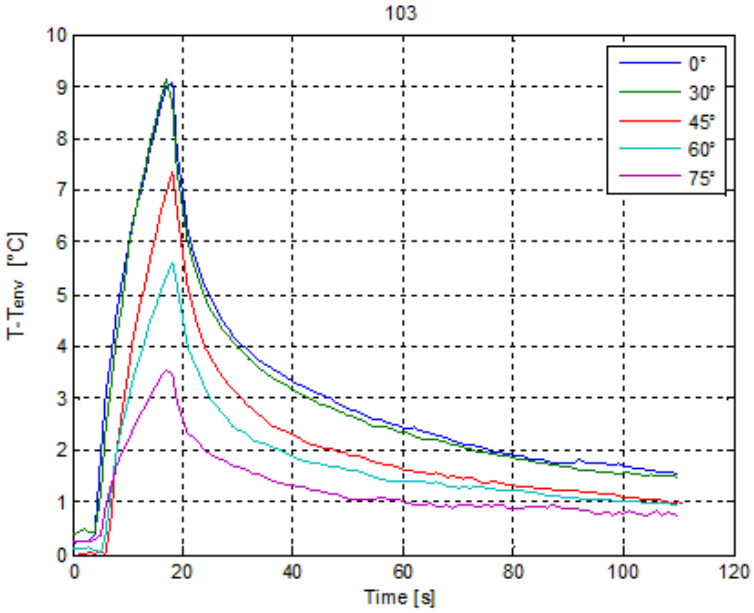

Figure 4.34: Thermocouple, comparison, 103.

As it is stated in section 4.4.1, the radiant emissivity remains almost constant until the angle of observation reaches 60°. In particular, the ratio between the

temperature at 0° and at 30° is 0.99. Thus, considering an observation angle of 30°, a check is done regarding this aspect. A comparison is done considering the measure taken at 0° and at 30° by the thermocouple, a measure that is influenced only by the non-uniformity of the heating, and the temperature measured by the thermo-camera, which could be affected also by the directional emissivity. Taking into account the temperature of the cylinder after the heating phase, the ratio between the ΔT at 30° and at 0° is $13.5°/19° = 0.71$, while the thermocouple is characterized by a ratio equal to $7°/9° = 0.77$. Thus, it is demonstrated that the effect of the directional emissivity for such angle is very low.

4.5 Experimental analysis of the cylindrical sample

The analysis on the cylinder exploits all the considerations done until now. In addition to these, other aspects have to be carefully analyzed. First of all, all the thermographic images have to be analyzed to find the zones of interest, such that only the cylinder is displayed in the image. It is important to highlight that the whole image displays the portion of the cylinder comprised between the two tangency angles of the thermo-camera.

4.5.1 Geometric evaluations

An important issue to consider is linked with the cylindrical shape of the object under investigation, which requires a particular analysis. The image acquired by the thermo-camera is a projection of the sample on a bi-dimensional plane. In this case, as opposed to the case of the straight sample, this projection is not scaled with respect to the actual surface of the cylinder: this is configured as a rectangle with a height representative of the height of the specimen, while the horizontal side is linked with the x-projection of the tangency points, not to the circumference. For this reason, the image needs to be resized with an expansion in order to correctly represent the real dimension of the cylinder. The acquired image has a number of columns and rows, respectively, of 222 and of 165. Since, as it is stated before, the height of this rectangle is representative of the real case, taking this dimension as a reference, it is considered that each pixel corresponds to a physical dimension of 0.9 mm. As a further confirmation of the correctness of the assumptions made before, it is obtained that, with this interval, the horizontal projection of the tangency point on the bi-dimensional image corresponds to a real dimension of 149 mm, value that is confirmed also by the analytic evaluation. An issue with this technique is the fact that the analyzed pixels are equally spaced on the projected plane, but their corresponding points on the circumference are characterized by different

distances one from each other. This distance has its maximum value at the furthest point, while as the point becomes closer and closer to the centre of the sample, the distance decreases, as Figure 4.36 shows. The trend of the observation angle is depicted in Figure 4.35. For this reason, in addition to the expansion of the image, also an operation of regularization of the spatial step is required. It is chosen to expand the horizontal size of the image considering the spatial step found before. The portion of the circumference comprised between the two tangency angles is 215 mm, which correspond to number of points equispaced with an interval of 0.9 mm equal to 238. In this way a matrix of 225x238 is obtained. The principal issue with this technique is to assign the correct values to the added columns. In order to do this, a comparison is done between the points on the circumference corresponding to the horizontal projection and the new equispaced points: all the new points comprised between an interval defined by the old coordinates assume the value of the interval itself. This procedure is obtained exploiting a constant interpolation between the old points and the new ones. It is important to highlight that in Figure 4.36 the considered angle is the central angle.

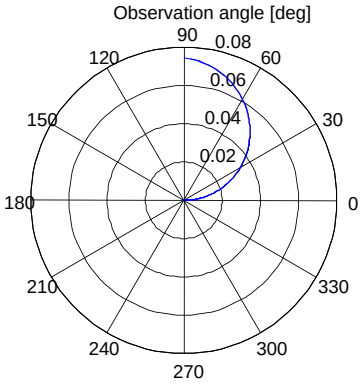

Figure 4.35: Trend of the observation angle.

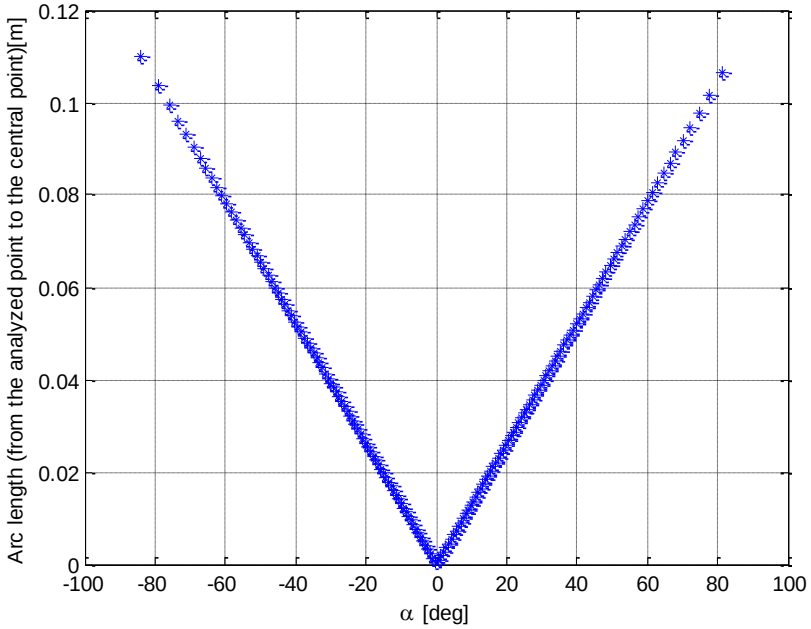

Figure 4.36: Distance between each analyzed point and the central point.

With these procedures, it is obtained a matrix of temperature, whose vertical and horizontal direction are scaled with respect, respectively, to the height of the cylinder and the portion of circumference comprised between the two tangency points: 2 mm and 215 mm.

4.5.2 Emissivity considerations

The thermo-camera requires as input the emissivity of the surface. In this way, from a theoretical point of view, it should be able to give as output an estimation of the temperature of the surface corrected by this index, in such a way that the temperature value is related to the effective radiation emitted by the surface and not to the one seen by the thermo-camera, influenced by the emissivity of the surface. This is true in the case of a straight sample, whose points are characterized by the same value of emissivity. In the case of a surface with a varying emissivity, such as the analyzed one, the correction applied by the infrared instrument is not correct. It is, thus, necessary to remove it, in order to obtain, for each point, the temperature seen by the thermo-camera, which takes into account the effect caused by the different emissivity of each point of the sample. Thus, each pixel is multiplied by the value of the emissivity imposed to

the thermo-camera in order to obtain the value of the temperature seen by the infrared instrument. This value has to be corrected with the real emissivity value. Considering the geometric assumptions and the consequent transformation explained in the previous section, each value of the starting matrix is multiplied by the $\varepsilon_{thermo\text{-}camera}$; each number of the expanded matrix is, then, corrected with the suitable value of emissivity. To find this value, it is possible to exploit the considerations made in section 4.4.1. With the exploited interpolation, it is possible to find the value assumed by ε_ϑ in each point of the new equispaced grid. This value takes into account only the value in the analyzed points, but, since the emissivity varies as the coordinate changes, it is important to consider also the influence of the neighbourhood. So, for each point, it is considered an interval centred on it. Each interval is, then, subdivided in several points, each one characterized by an emissivity, different one by each other. Then a mean is conducted on these values, a mean that replaces the value of the emissivity on this point. Figure 4.37 shows how this assumption behaves. An important remark regards the number of points in which each interval is subdivided. Indeed, it has been chosen as the minimum able to guarantee the convergence of the mean value.

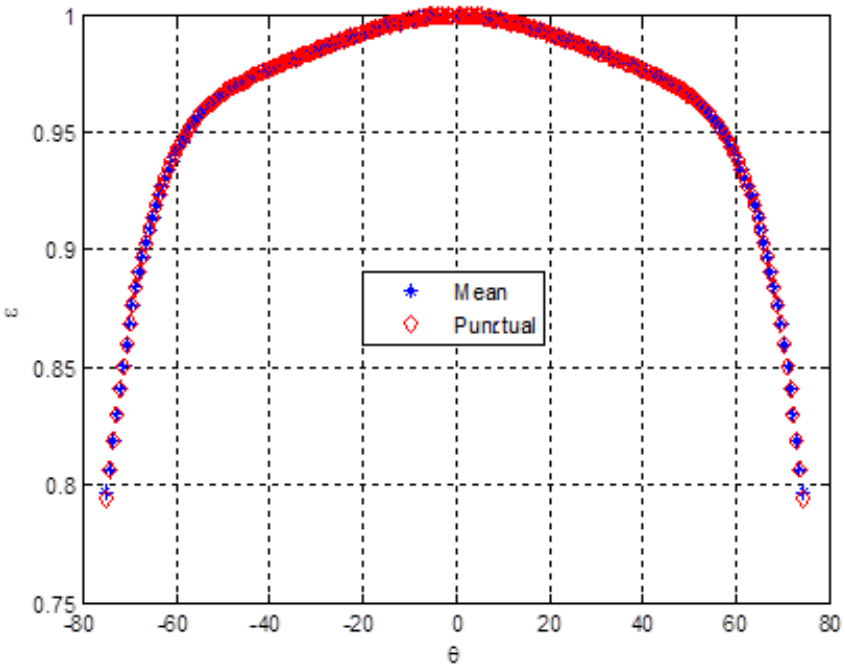

Figure 4.37: Emissivity values, averaged and punctual.

As it can be seen, the averaged value is slightly different from the punctual one of the point, since there are not huge changes in the emissivity values varying the observation angle. It is important to highlight that the portion of the cylinder

characterized by a ϑ angle exceeding 75° is not taken into account, since there are no data available on the behaviour of surfaces with such high observation angles. To resume, the following diagram shows the different stages the post-processing of the cylinder requires:

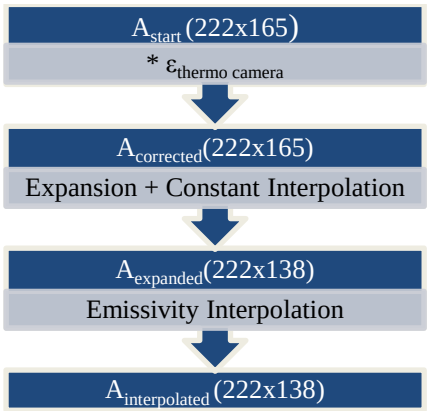

The following graphs show the results obtained at each stage.

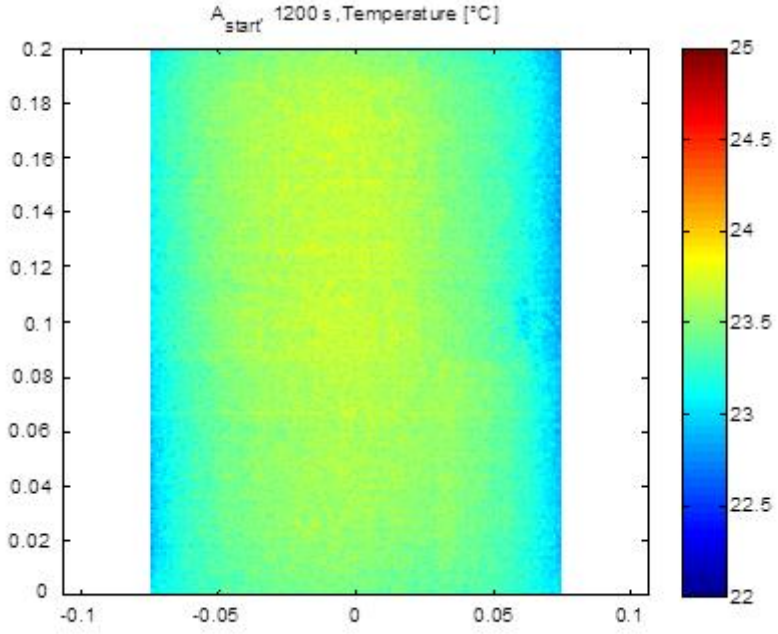

Figure 4.38: Cylinder, starting image, 1200 s.

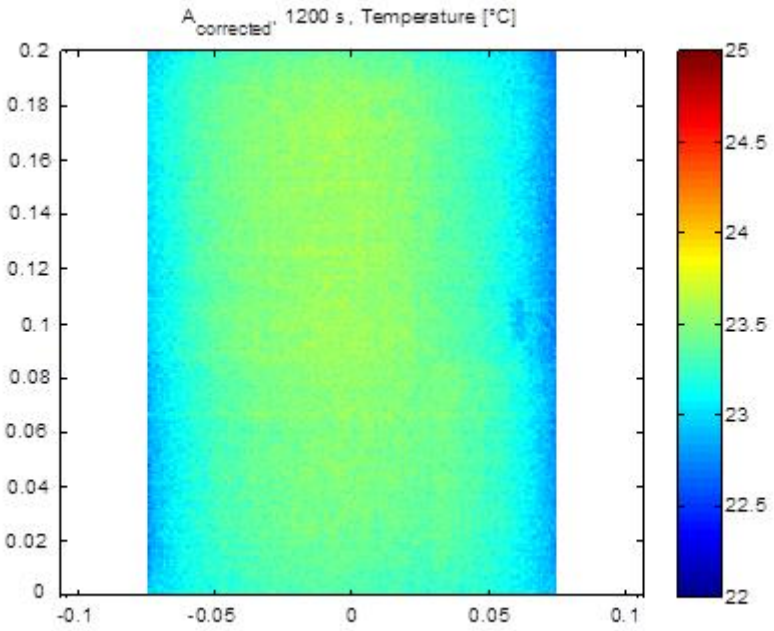

Figure 4.39: Cylinder, correction with ε thermo-camera, 1200 s.

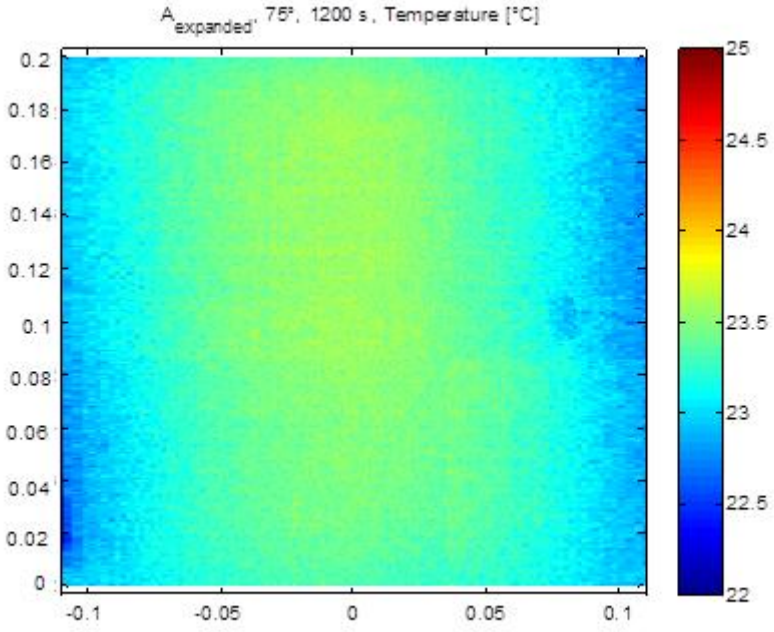

Figure 4.40: Cylinder, Expansion, 1200 s.

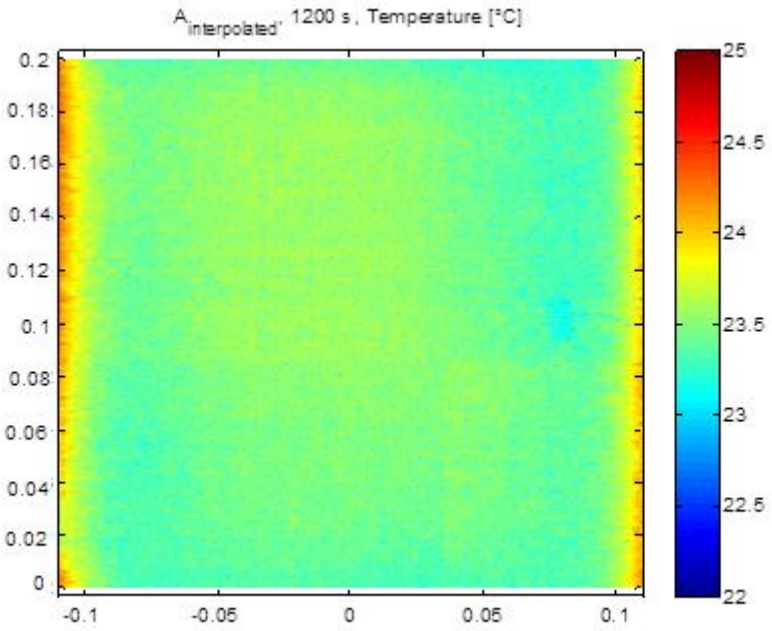

Figure 4.41: Cylinder, final image, 1200 s.

As it can be seen in Figure 4.41, the applied interpolation of emissivity is over corrected when the angle approaches 75°. This is due to the fact that the experimental tests to evaluate the emissivity have not taken into account any angles between 60° and 75°, range in which the emissivity changes in the most significant way. Thus, the interpolation has no data available on this interval.

Chapter 5
Numerical analyses

Comsol 4.2 is exploited to make numerical evaluations of the objects under analysis, in order both to compare these results with the ones obtained from the experimental tests and to have other data available on which a deeper investigation is subsequently conducted. It is important to highlight that the heating time and the power emitted by the heating source are fundamental parameters in this case, as it is stated in section 4.1.3. For this reason, several analyses are conducted to find the optimal values of these parameters.

5.1 Tilted samples

First of all, some preliminary analyses are conducted, to understand how the sample behave in a tilted configuration rather that in a straight one. A first comparison is done to understand the behavior with respect to different heat durations in a straight and in a tilted sample. The utilized model is a three dimension model: a squared Plexiglas specimen, 0.1 m lengthwise and 0.01 m thick. Since this is a preliminary analysis, it is chosen to model a squared flaw, in such a way that the computational complexity both for the mesh and for the analysis is reduced. Thus, a cubic air flaw, centred in the centre of the specimen, with a side of 0.02 m and a thick of 0.04 m is modeled. The defect is supposed to be 0.06 m under the upper surface, in such a way that its bottom side is coincident with the bottom surface, forming a sort of dummy hole. As in the experimental case, also in this part of the analysis the simulation is divided in two parts: the heating and the cooling stages. The first one is analyzed applying a finer time step, while the second one is analyzed each second for 1200 s, as in the experimental set-up, in such a way that also in this case the minimum detectable frequency is 8.3e-4 Hz. Taking into consideration the symmetry of the problem, not the whole sample requires to be modeled. The whole object is reconstructed during the post processing stage, exploiting Matlab program. In the case of the straight sample, for the sake of simplicity, it is decided to model only a quarter of the problem. The boundary conditions applied are the following, with respect to Figure 5.1 and to Figure 5.2: on sides 4, 5 and 6 insulation conditions and symmetry conditions on sides 1 and 3 for both the stages, while in the heating stage an inward heat flux, 100 $\frac{W}{m^2}$, is applied on face 2.

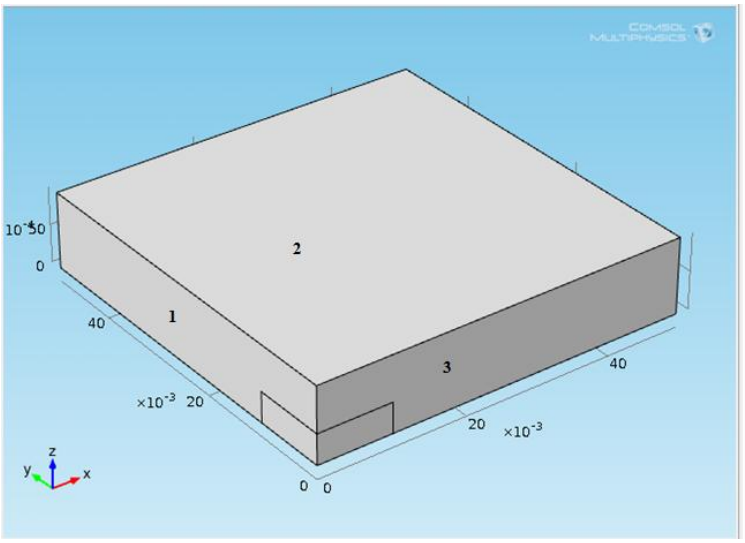

Figure 5.1: Front view, Comsol.

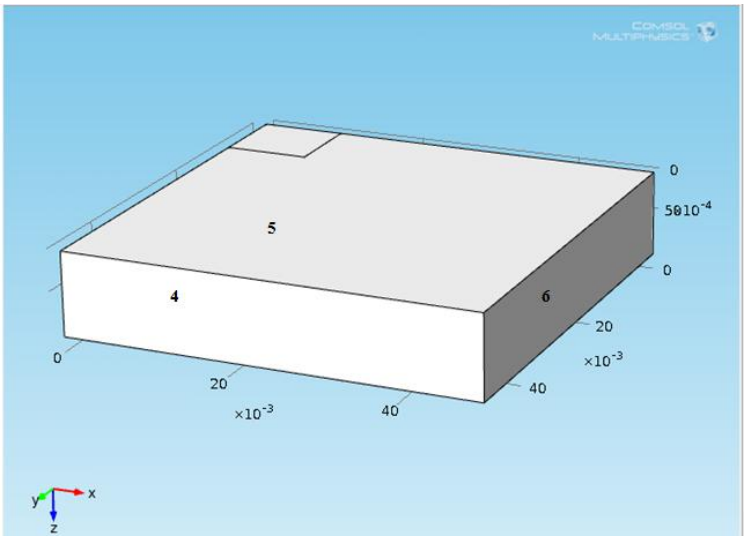

Figure 5.2: Back view, Comsol.

To make a deeper investigation, tests are conducted in similar conditions, changing the height of the hole: 0.0005 m and 0.001 m. The upper position of the flaw remains unchanged, in such a way that its deepness is constant under the upper surface of the specimen. Results are shown from Table 5.1 to Table 5.3. The phase difference is obtained subtracting the flaw phase from the sound phase. It is important to highlight that, as Figure 5.3 shows, the maximum value of phase difference is negative. This trend is due to the thickness of the sample, as it is stated in [23]. It is important to highlight that, for the sake of simplicity, to have a deeper understanding of the phenomenon, all the graphs represent the

absolute value of the phase difference. As it is stated in section 2.4, the frequencies of interest are only the first ones: the maximum value of phase difference is reached in correspondence of the lowest band of the spectrum. Figure 5.3 and Figure 5.4 show this trend for the heating time of 1 s. As it can be seen, the higher the frequencies, the lower the values of the phase difference. It is important to highlight that in all the tables from here onwards, the percentage error is defined as:

$$\text{error} = \left|\left(\frac{\text{Real depth} - \text{Estimated depth}}{\text{Real depth}}\right) * 100\right| \tag{5.1}$$

Table 5.1: Results on the dummy hole.

Dummy hole						
Heating time (s)	Maximum $\Delta\Phi$ [deg] (absolute value)	Number of $f_{\Delta\Phi max}$	$f_{\Delta\Phi max}$ [Hz^{-3}]	Estimated depth [m^{-3}]	Real depth [m^{-3}]	Percentage Error
1	4.68	2	8.3e-1	6.5	6	8%
3	5.04	2	8.3e-1	6.5	6	8%
5	5.41	2	8.3e-1	6.5	6	8%
10	6.24	2	8.3e-1	6.5	6	8%
20	7.57	2	8.3e-1	6.5	6	8%

Table 5.2: Results on the hole with an height of 0.0005 m.

Hole, Height 0.0005						
Heating time (s)	Maximum $\Delta\Phi$ [deg] (absolute value)	Number of $f_{\Delta\Phi max}$	$f_{\Delta\Phi max}$ [Hz^{-3}]	Estimated depth [m^{-3}]	Real depth [m^{-3}]	Percentage Error
1	1.89	2	8.3e-1	6.5	6	8%
3	1.99	2	8.3e-1	6.5	6	8%
5	2.24	2	8.3e-1	6.5	6	8%
10	2.65	2	8.3e-1	6.5	6	8%
20	2.96	2	8.3e-1	6.5	6	8%

Table 5.3: Results on the hole with an height of 0.005 m.

Hole, Height 0.005						
Heating time (s)	Maximum $\Delta\Phi$ [deg] (absolute value)	Number of $f_{\Delta\Phi max}$	$f_{\Delta\Phi max}$ [Hz^{-3}]	Estimated depth [m^{-3}]	Real depth [m^{-3}]	Percentage Error
1	2.34	2	8.3e-1	6.5	6	8%
3	2.64	2	8.3e-1	6.5	6	8%
5	2.97	2	8.3e-1	6.5	6	8%
10	3.25	2	8.3e-1	6.5	6	8%
20	3.59	2	8.3e-1	6.5	6	8%

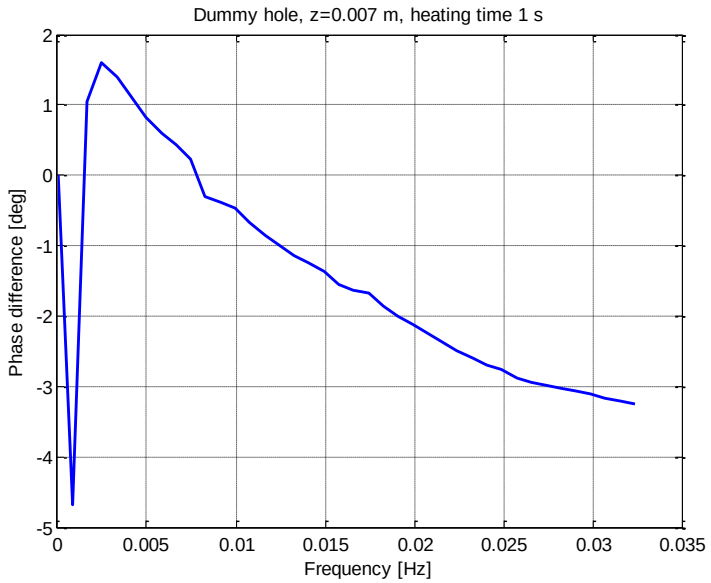

Figure 5.3: Dummy hole, z=0.006, heating time 1s, first values.

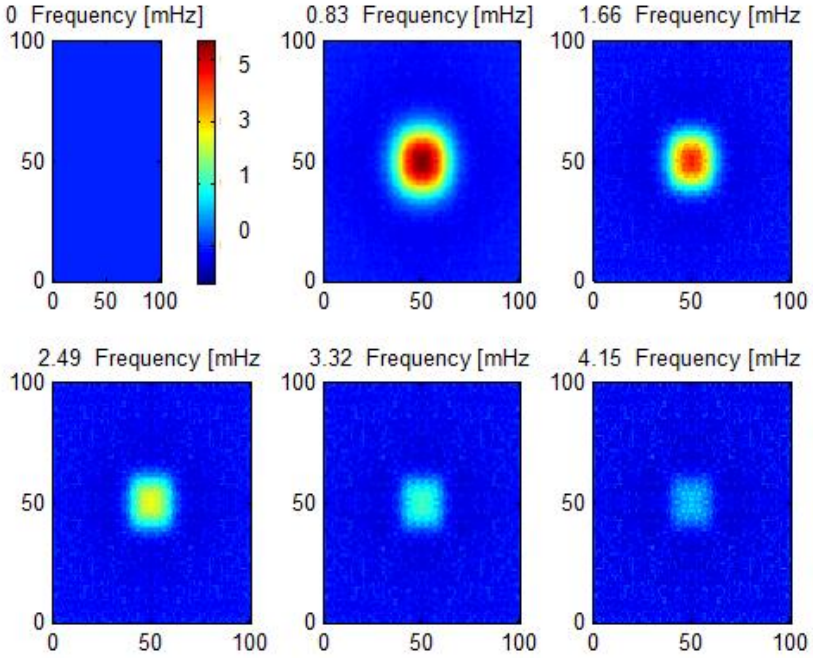

Figure 5.4: Dummy hole, phase difference, first frequencies, heating time 1s.

As Figure 5.4 demonstrates, the higher the heating time, the higher the value of the maximum phase difference. This is shown also in Figure 5.5. This value tends to increase also when the thickness of the flaw increases. On the other

hand, the frequency which corresponds to the maximum value of phase difference does not change varying the heating time, as it is demonstrates also in Figure 5.6. This is probably due to the fact that, for such configuration, all the considered *stimuli* are able to correctly excite the specimen.

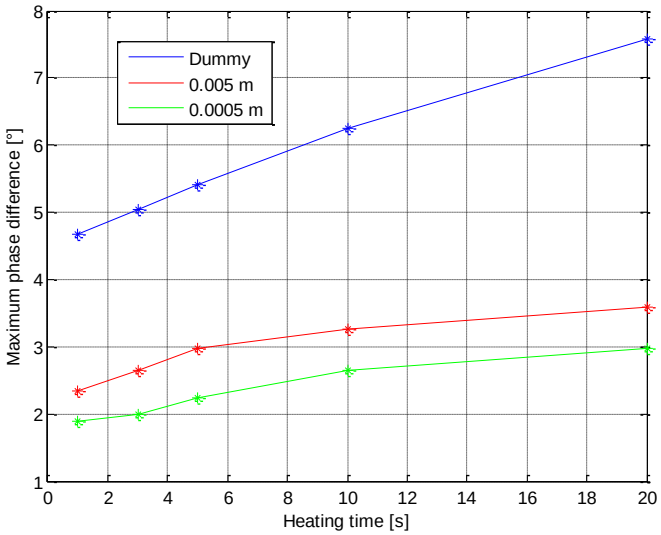

Figure 5.5: Maximum phase difference, heating time 1 s.

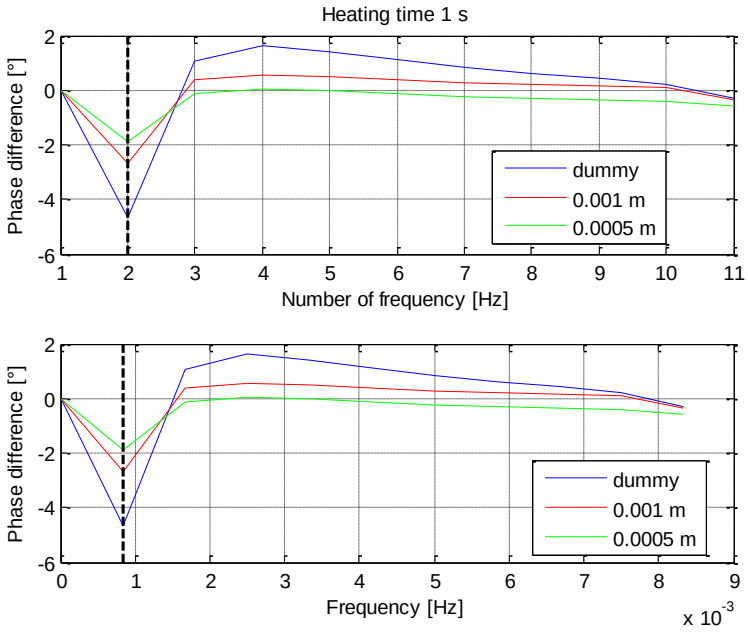

Figure 5.6: Phase difference, first values, heating time 1 s.

In order to make a preliminary study on the consequences of a non uniform heating due to the rotation of the specimen, a comparison is made with the dummy hole in the previous analyzed sample, due to the fact that no significant

changes are introduced changing the thickness of the flaw. In addition to this fact, in the case of an experimental comparison, the sample is going to present a dummy hole. In this case, the specimen is tilted of 45° with a configuration similar to the one depicted in Figure 4.21 and in Figure 4.22. The rotation is assumed to occur around the centre of the specimen. Taking into account a right handed reference frame, as it is depicted in Figure 5.7, the inward heat flux is supposed to vary with the x coordinate.

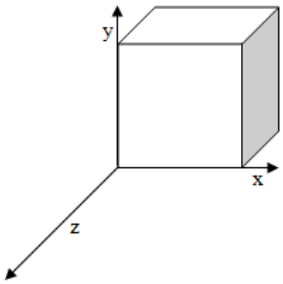

Figure 5.7: Reference Frame, Comsol.

The specimen is insulated from the environment also in this case. The hole is centred in the same central point of the sample, to make it experiment both an increasing and a decreasing heat flux. For this reason, it is no more possible to model only a quarter of the sample, as in the previous case, but, to simplify the computational complexity, one half of the specimen is considered and the whole sample is reconstructed in the post processing stage. The model, so, is 0.1 m length and 0.05 m width, as it is depicted in Figure 5.9. The boundary conditions applied are similar to the previous case, but, in this model, only face 1 experiments a symmetry condition, while all the other sides are assumed to be adiabatic. An evaluation of the increasing distance from the heating source is required in order to reproduce correctly the situation. For the sake of simplicity, the sample is assumed to be centred in (0, 0.025, 0.005). In this way the x-coordinate spaces from -0.05 m to 0.05 m. The distance between each x point and the lamps is determined exploiting the *Carnot theorem*; taking into consideration that in the case previously described the specimen surface is posed 0.6 m away from the lamps and that the inclination angle is 45°, the theorem takes the form of:

$$f(x) = \begin{cases} \sqrt{0.6^2 * \mathrm{abs}(x)^2 - 2 * 0.6 * \mathrm{abs}(x) * \cos(45°)}, & x < 0 \\ \sqrt{0.6^2 * x^2 - 2 * 0.6 * x * \cos(135°)}, & x \geq 0 \end{cases}$$

In this way, as it can be seen in Figure 5.8 the distance between the central x point and the heating lamps is 0.6 m and the inward heat flux is dimensioned to have on this point a value equal to 100 $\frac{W}{m^2}$, in such a way that the condition of the sample not tilted is perfectly reproduced in the centre of rotation.

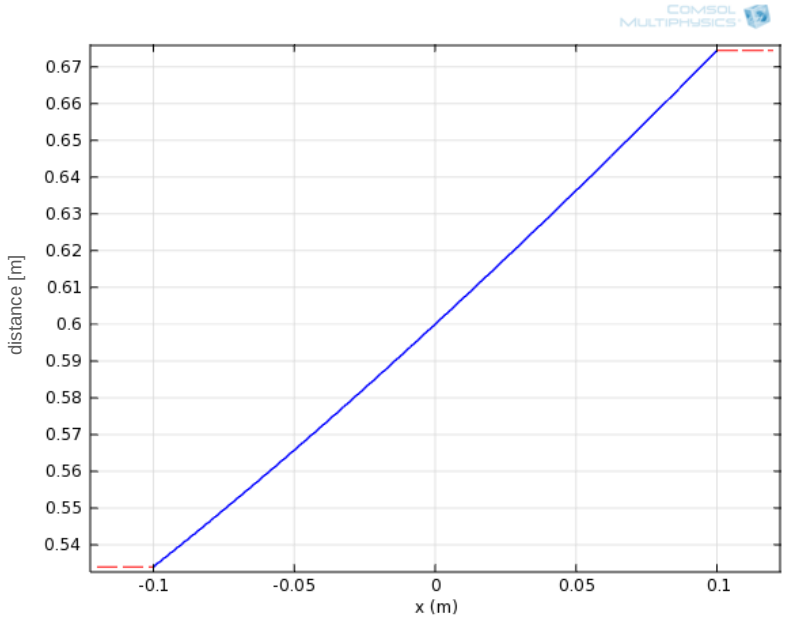

Figure 5.8: Distance from the heating sources.

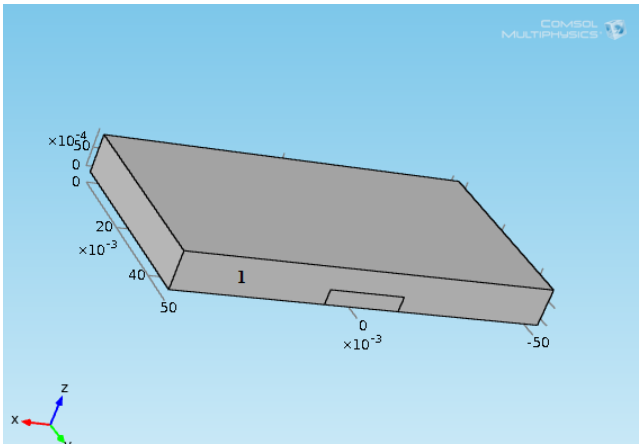

Figure 5.9: Comsol, tilted model.

The specimen is heated for 1s, 3s, 5s, 10s and 20s, as in the previous case, to make a comparison between the different situations. The analysis is, then, conducted on the cooling stage, during which the temperature is collected each second for 1200 s. Figure 5.10 shows the variation of temperature during this stage for two different points, with a different y and the same x coordinate. As it can be seen, the temperature is not affected by a variation of y, since the heat flux is a function of the x only.

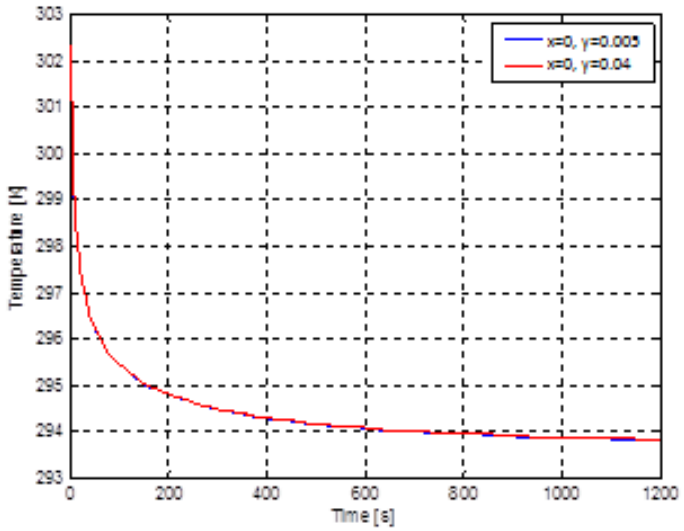

Figure 5.10: Temperature of different points, tilted sample.

A matter with this technique is the fact that the surface temperature varies with the x-coordinate. So it is difficult to choose the sound area with which comparing the phase of the flaw. It is chosen to consider, as a reference, the point with an x coordinate equal to the ones of the centre of the defect. In this way the two points experiments the same inward heat flux. To better understand the effects due to the choice of the *sound point*, an analysis is conducted also considering a sound point taken in an area that is not influenced by the flaw, but that is characterized by a different x coordinate, as Figure 5.11 shows. As it can be seen in Table 5.4, changing the *sound point* does not change the value of the estimated depth. This is a further pro of the *Pulse Phase Thermography* method: as it is stated in section 1.1.3, it is able not to take into account the effects of a non uniformity in the heating. It is important to highlight that also in this case the value of the maximum phase difference is negative, due to the small depth of the sample.
Results are shown in Table 5.4.

Table 5.4: Tilted configuration

Heating time [s]	Sound point	Maximum ΔΦ [deg] (absolute value)	Number of $f_{\Delta\Phi max}$	$f_{\Delta\Phi max}$ [Hz^{-3}]	Estimated depth [m^{-3}]	Percentage Error
1	-0.0495 2.5126e-4	4.30	2	8.3e-4	6.5	8%
	2.5126e-4 2.5126e-4	4.41	2	8.3e-4	6.5	8%
	0.0495 2.5126e-4	4.46	2	8.3e-4	6.5	8%
3	-0.0495 2.5126e-4	4.82	2	8.3e-4	6.5	8%
	2.5126e-4 2.5126e-4	5.02	2	8.3e-4	6.5	8%
	0.0495 2.5126e-4	4.95	2	8.3e-4	6.5	8%
5	-0.0495 2.5126e-4	5.31	2	8.3e-4	6.5	8%
	2.5126e-4 2.5126e-4	5.50	2	8.3e-4	6.5	8%
	0.0495 2.5126e-4	5.43	2	8.3e-4	6.5	8%
10	-0.0495 2.5126e-4	6.25	2	8.3e-4	6.5	8%
	2.5126e-4 2.5126e-4	6.43	2	8.3e-4	6.5	8%
	0.0495 2.5126e-4	6.37	2	8.3e-4	6.5	8%
20	-0.0495 2.5126e-4	6.52	2	8.3e-4	6.5	8%
	2.5126e-4 2.5126e-4	6.78	2	8.3e-4	6.5	8%
	0.0495 2.5126e-4	6.64	2	8.3e-4	6.5	8%

As it can be seen in the previous tables, the results do not change considering a straight and a tilted configuration.

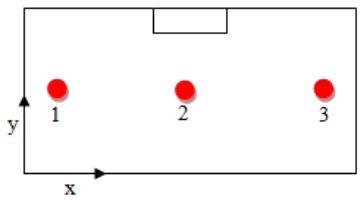

Figure 5.11: Sound point, tilted configuration.

The same procedure is applied for cylindrical flaws, with inclination angle of 0° and of 45°. Also in this case a sensitivity analysis to the heating time is done. Considering the improvement in the heating device of the ThermALab, it is chosen to test the behaviour of the specimen considering two different amount of the input power of the heating source, 1000 W and 3000 W. Exploiting the program developed in [23], it is known that the duration of the heating can be identified in 10 s or in 20 s. Thus, a sensitivity analysis is conducted considering, for each flaw, four different heating: 1000 W for 10 s, 1000 W for 20 s, 3000 W for 10 s and 3000 W for 20 s. It is important to highlight that in these preliminary analyses it is evaluated as sound point only the central ones, since it is assumed that, as it is demonstrated in the previous case, this choice does not change the results. Once that the heating parameters are fixed, also the other sound points are analyzed. Results are shown in the following tables.

Table 5.5: Different heating time, D8mm-z2.5mm, straight sample.

D 8 mm, z 2.5 mm			
Straight configuration			
Heating power [W]	Heating time [s]	Estimated depth [m^{-3}]	Percentage Error
1000 W	10 s	2.9	16%
1000 W	20 s	2.4	4%
3000 W	10 s	2.9	16%
3000 W	20 s	2.5	2%

Table 5.6: Different heating time, D8mm-z2.5mm, tilted sample.

D 8 mm, z 2.5 mm				
Tilted configuration				
Heating power [W]	Heating time [s]	Sound point	Estimated depth [m^{-3}]	Percentage Error
1000 W	10 s	2	2.9	16%
1000 W	20 s	2	2.4	4%
3000 W	10 s	2	2.9	16%
3000 W	20 s	2	2.5	2%

Table 5.7: Different heating time, D6mm-z3mm, straight sample.

D 6 mm, z 3 mm			
Straight configuration			
Heating power [W]	Heating time [s]	Estimated depth [m^{-3}]	Percentage Error
1000 W	10 s	3.7	23%
1000 W	20 s	3.2	7%
3000 W	10 s	3.2	7%
3000 W	20 s	2.9	3%

Table 5.8: Different heating time, D6mm-z3mm, tilted sample.

D 6 mm, z 3 mm				
Tilted configuration				
Heating power [W]	Heating time [s]	Sound point	Estimated depth [m^{-3}]	Percentage Error
1000 W	10 s	2	3.7	23%
1000 W	20 s	2	3.2	7%
3000 W	10 s	2	3.2	7%
3000 W	20 s	2	2.9	3%

Table 5.9: Different heating time on D8mm-z4mm, straight sample.

D 8 mm, z 4 mm			
Straight configuration			
Heating power [W]	Heating time [s]	Estimated depth [m^{-3}]	Percentage Error
1000 W	10 s	3.7	7.5%
1000 W	20 s	3.7	7.5%
3000 W	10 s	3.7	7.5%
3000 W	20 s	3.7	7.5%

Table 5.10: Different heating time, D8mm-z4mm, tilted sample.

D 8 mm, z 4 mm				
Tilted configuration				
Heating power [W]	Heating time [s]	Sound point	Estimated depth [m^{-3}]	Percentage Error
1000 W	10 s	2	3.7	7.5%
1000 W	20 s	2	3.7	7.5%
3000 W	10 s	2	3.7	7.5%
3000 W	20 s	2	3.7	7.5%

As it can be seen, a heating of 20 s for 3000 W allows the better identification. It is important to highlight that as the depth increases there are no significant changes varying the typology of the heating. Probably this is due to the fact that the deeper the flaw, the lower the frequency at which the maximum phase difference has to occur for a good identification. With a minimum available frequency of 8.3e-4, the deepest possible dimensions are 0.0065 m and 0.0046 m, connected, respectively, to 8.3e-4 Hz and to 0.0017 Hz. Thus, for the deeper defects, it is necessary a high excitation only of the first frequencies. As it can be seen in section 2.4, both 10 s and 20 s are able to excite in a correct way these frequencies.
Table 5.11 shows the complete results for the three flaws taken into account subjected to a heating power of 3000 W for 20 s, respectively for the straight and the tilted configuration.

Table 5.11: Results on dummy holes, straight sample.

Defect geometry		Maximum ΔΦ			Estimated depth [m^{-3}]	Percentage Error
Depth [m^{-3}]	Diameter [m^{-3}]	Value [deg] (absolute value)	Number of f	f at ΔΦ maximum [Hz^{-3}]		
2.5	8	11.48	8	5.8	2.5	2%
3	6	6.01	6	4.2	2.9	3.33%
4	8	6.33	3	1.7	3.7	7.5%

Table 5.12: Results on dummy holes, tilted sample.

Defect geometry		Inclination angle [deg]	Sound point	Maximum ΔΦ			Estimated depth [m^{-3}]	Percentage Error
Depth [m^{-3}]	Diameter [m^{-3}]			Value [deg] (Absolute value)	Number of freq	f at ΔΦ maximum [Hz^{-3}]		
2.5	8	45	-0,0989949 0,00050251	11.48	8	5.8	2.5	2%
			0,0005025 0,0005025	12.39	8	5.8	2.5	2%
			0,0989949 0,0005025	11.24	8	5.8	2.5	2%
3	6	45	-0,0989949 0,00050251	6.01	6	4.2	2.9	3%
			0,0005025 0,0005025	6.49	6	4.2	2.9	3%
			0,0989949 0,0005025	6.01	6	4.2	2.9	3%
4	8	45	-0,0989949 0,00050251	6.33	3	1.7	3.7	7.5%
			0,0005025 0,0005025	7.17	3	1.7	3.7	7.5%
			0,0989949 0,0005025	6.25	3	1.7	3.7	7.5%

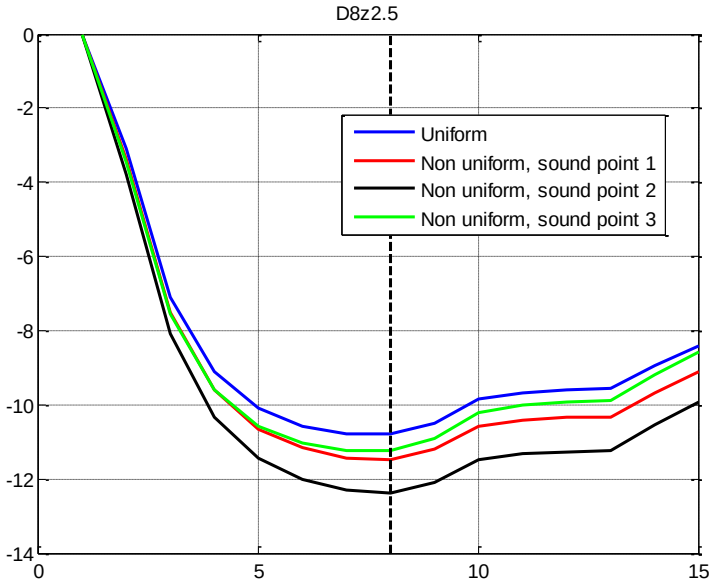

Figure 5.12: Comparison between phase difference, D8z2.5, first values.

As it can be seen, the optimum visibility frequency. This guarantees the same results, even if there are some slight differences.

5.2 Cylindrical samples

After that the preliminary analyses have been conducted, with the important confirm that the *Pulse Phase Thermography* technique is not invalidated by the choice of a different *sound point*, numerical analyses are done on a cylindrical Plexiglas tube with an outer and an inner diameter, respectively, of 0.15 m and 0.13 m, with an height of 0.2 m, as the sample utilized in the previous test campaign. Also in this case, due to the symmetry of the problem, only a quarter of the described pipe is modeled, to minimize both the computational and the geometrical complexity. In this way, a hollow pipe with a cross section of an half of a cylinder is modeled. Due to the particular shape of the sample, two significant issues with this simulation involve the directional emissivity and the mesh, due to the calendering of the surface the finite elements have to befit to.

5.2.1 Mesh

Meshing an object implies to find a triangulation that is able to approximate the domain Ω as best as it can. The domain is subdivided into smaller elements, in such a way that their union is really close to the real structure. Calling τ_h the adopted assembly of elements, each one with a dimension characterized by the *h* parameter, it can be easily noticed that $\cup_k \cong \Omega$, where $k \in \tau_h$. As it is stated in [42], it is important to utilize the coarsest mesh able to capture the dominant behaviour of the physical model. In the case of a non-straight domain, this could represent a complication, since the chosen elements have to deal with curved edges. For this reason, for the geometry under investigation, several attempts have been conducted to find the optimal compromise between the computational complexity and a good representation of the physic of the problem. In general, a refinement in the dimension of the element is set up in those zones closer to the area of interest, while in the remaining part the mesh is coarser. For this reason, it is chosen to subdivide the domain in four parts, in such a way that it is simpler to deal with the mesh in the different areas, as it is depicted in Figure 5.13: the further the area from the flaw, the coarser the mesh and *vice versa*. In order to obtain this subdivision, the different parts are made and assembled exploiting SolidWorks; then the whole assembly is imported in Comsol Multiphysics. In this way both the definition of the four areas and the realization of the suitable mesh are easier. Considering the zx plane, the distribution of the elements becomes denser approaching the flaw. The same mesh feature is applied in whole domain: starting from y=0, this mesh distribution is repeated at regular close interval in the area 2 and 3, while, as the y coordinate in region 1 increases, the spatial step between two following mesh planes becomes coarser. This structure is shown in Figure 5.15 and in Figure 5.16.

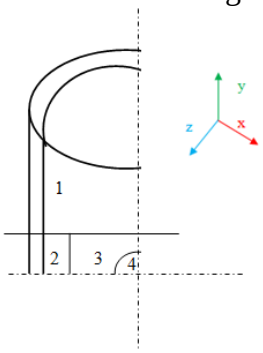

Figure 5.13: Outline of the different zones of interest of the cylinder.

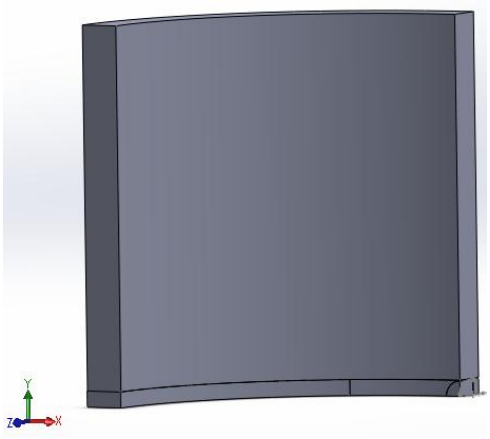

Figure 5.14: Outline of the different zones of the cylinder, SolidWorks.

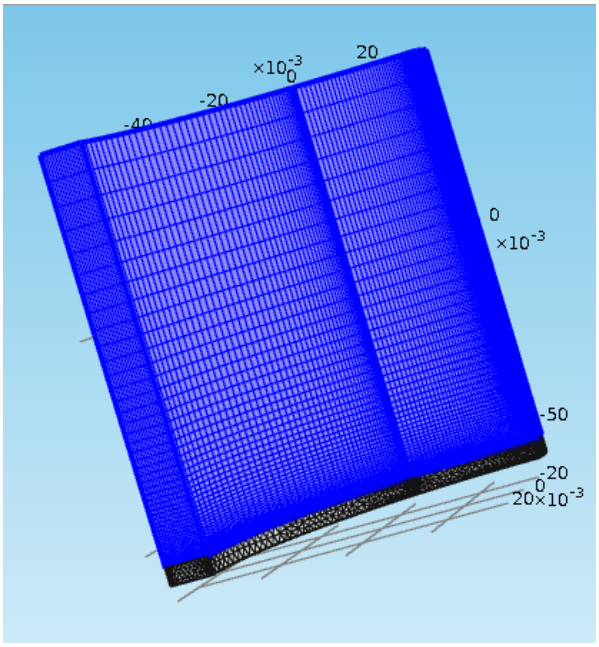

Figure 5.15: Mesh of the domain, y direction.

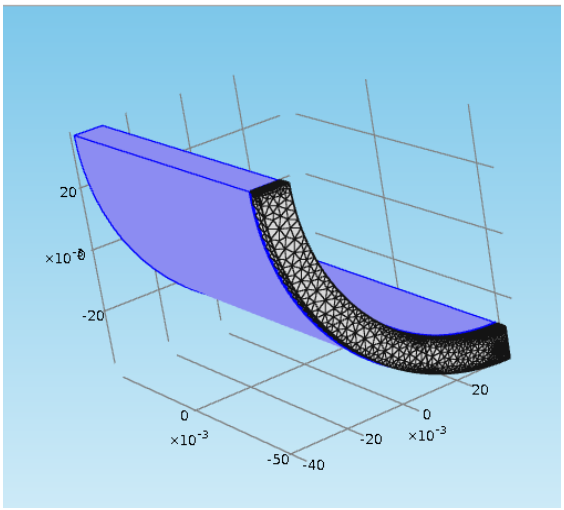

Figure 5.16: Mesh of the domain, xz plane.

With this schematization, considering the external surface of the cylinder in correspondence to y=0, the distribution of the phase difference like the one depicted in Figure 5.17.

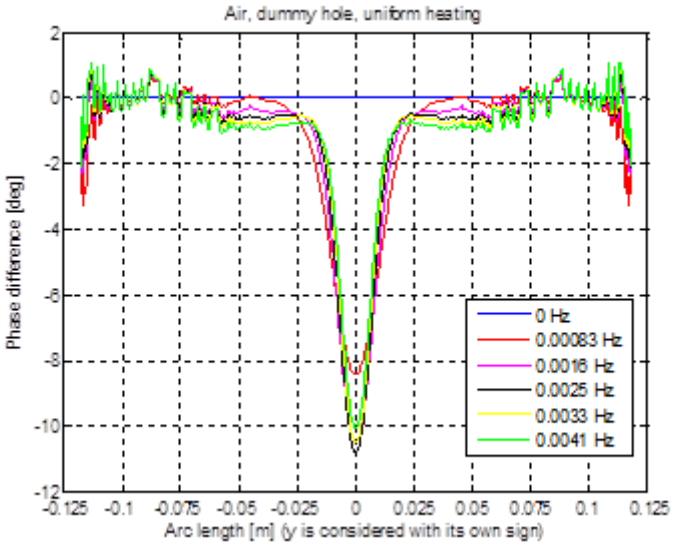

Figure 5.17: Phase difference, external surface, y=0, finer mesh.

It is important to notice how the oscillations are due to the discretization Comsol exploits. Indeed, the denser the mesh, the more reduced becomes the amplitude of the oscillation. To test this aspect, the same analyses are conducted considering the whole domain with an equivalent mesh discretization. In this way, the distribution of the finite elements results the same, but the dimension of each element is bigger. As it can be seen, the amplitude of the oscillation is

higher in this last case with respect to the previous one, especially in the part closer to the flaw.

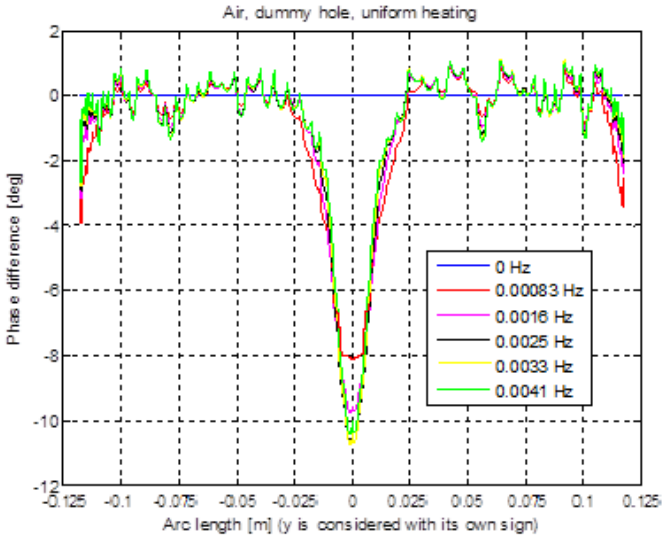

Figure 5.18: Phase difference, external surface, y=0, coarser mesh.

The denser the mesh, the smaller the oscillation. Some tests are conducted considering a number of degrees of freedom higher than one thousands. With this huge number of elements, the oscillations are very attenuated, but they are still present in the first time instants. Considering that the goal of this work is to find the depth of different type of flaws exploiting the phase difference between the sound region and the centre of the flaw, this aspect can be easily detected notwithstanding the presence of such oscillations, since their amplitude is not going to invalidate the results. In order to totally avoid the oscillations, a number of degrees of freedom higher than one thousands is requested, but this feature implies a too elevated computational complexity, in such a way that the simulation requires a too long time without a better identification of the depth of the flaw. Indeed, as Table 5.13 demonstrates, the estimated depth is the same with the two different types of mesh.

Table 5.13: Air flaw, coarser mesh.

	Defect geometry		Maximum $\Delta\Phi$			Estimated depth [m^{-3}]	Percentage Error
Coarser mesh	Depth [m^{-3}]	Diameter [m^{-3}]	Value [deg] (Absolute value)	Number of $f_{\Delta\Phi max}$	$f_{\Delta\Phi max}$ [Hz^{-3}]		
	3	8	8.64	4	2.5	3.2	8%
	2	2	3.44	13	10	1.9	6%
	4	6	1.23	3	1.7	4.6	7%

Table 5.14: Air flaw, finer mesh.

	Defect geometry		Maximum ΔΦ			Estimated depth [m^{-3}]	Percentage Error
Finer mesh	Depth [m^{-3}]	Diameter [m^{-3}]	Value [deg] (Absolute value)	Number of $f_{\Delta\Phi max}$	$f_{\Delta\Phi max}$ [Hz^{-3}]		
	3	8	8.56	4	2.5	3.2	8%
	2	2	3.46	13	10	1.9	6%
	4	6	1.13	3	1.7	4.6	7%

5.2.2 Directional emissivity

The curvature of the surface under investigation requires a particular analysis to simulate the way in which the thermo-camera registers the temperature of the analyzed cylinder. The directional emissivity becomes the focus of this evaluation, since the registered emission depends on the angle between the normal to the surface and the observation direction. It is important to identify the angle of tangency of the thermo-camera. The thermo-camera is assumed to be located at 0.64 m away from the centre of the external surface of the cylinder. Knowing the radius of the external cylinder, indeed, the central angle corresponding to the tangency point is equal to 83°, which correspond to a x coordinate of $x_{tangency}$= 0.0745 m. So the emission from the points belonging to the external surface with an x-coordinate major than the tangency one is assumed not to be registered by the infrared instrument. Furthermore, the further the points from the thermo-camera axis, the lower the emission registered. As it is stated in [13], as the angle between the normal to the surface and the observation direction increases, the directional emissivity is going to decrease.

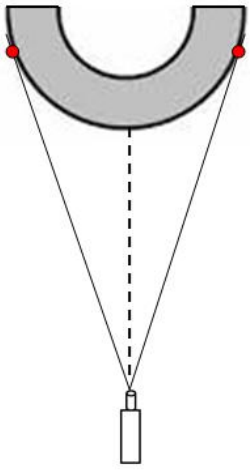

Figure 5.19: Outline of the tangency angle of the thermo-camera.

In the numerical simulations, the temperature is the real one emitted by the sample. Thus, the previous evaluations are not taken into account. It is important to highlight that Comsol Multiphysics could be an useful instrument for future evaluation on this aspect.

5.3 Heating typologies

The simulations are conducted considering, first of all, a uniform heating of the external surface of the cylinder, in a configuration similar to the one utilized in the experimental stage; then this test is conducted taking into account an inhomogeneous inward heat flux given by two tilted lamps. For this last simulation, the experimental configuration is assumed to be set up as the one depicted in Figure 4.21 and in Figure 4.22. An important feature is the tangency angle between the curved surface of the sample and the heating source. Indeed, it identifies the *discrimen* between areas heated either by only one lamp or by both of them. With reference to Figure 5.20, the points belonging to the arc $\widehat{AB}$ are subjected only to the inward heat flux of the first lamp, as the zone comprising the $\widehat{CD}$ arc is warmed up by the second lamp. The arc $\widehat{BC}$ experiments the inward heat flux given by both of the lamps.

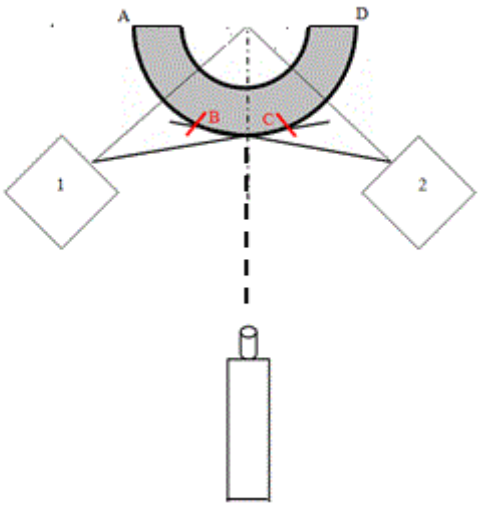

Figure 5.20: Outline of the tilted heating source.

5.3.1 Sensitivity analysis of the heating time

As it is stated before, it is fundamental, in this kind of simulations, to choose in an appropriate way the heating power and of the observation time. In [23], Vitali has fulfilled a program to determine the values of such parameters, program optimized for a thin sample and a sample approximated as a semi-infinite medium, respectively with a thickness of 0.004 m and of 0.02 m. Due both to the cylindrical shape of the specimen and to the thickness of the specimen, right in the middle of the difference between the two type of medium analyzed in the previous work, several proofs are conducted to find the optimal value of the heating parameters, considering the values suggested by [23] as a sort of starting guess. Thus, considering the developed heating apparatus of the Thermal lab, each flaw is subjected to four different type of heating: 1000 W for 10 s and 20 s and 3000 W, once again for 10 s and 20 s. It is important to highlight that for each one of the four heating type, both the uniform and the non uniform heating are taken into account, although the ability of the *Pulse Phase Thermography* is the fact that its analysis is not affected by the non uniformity in the heating. In this way also this aspect is tested. Results are shown from Table 5.15 to Table 5.20.

Table 5.15: Different heating time, z = 3 mm, cylindrical sample.

Depth 3 mm				
D = 8 mm				
Input power [W]	Heating time [s]	Heating type	Number of $f_{\Delta\Phi max}$	Percentage Error
1000 W	10	Uniform	5	7%
1000 W	10	Non uniform	5	7%
1000 W	20	Uniform	6	3%
1000 W	20	Non uniform	6	3%
3000 W	10	Uniform	5	7%
3000 W	10	Non uniform	5	7%
3000 W	20	Uniform	6	3%
3000 W	20	Non uniform	6	3%
D = 6 mm				
1000 W	10	Uniform	8	16%
1000 W	10	Non uniform	8	16%
1000 W	20	Uniform	7	10%
1000 W	20	Non uniform	7	10%
3000 W	10	Uniform	8	16%
3000 W	10	Non uniform	8	16%
3000 W	20	Uniform	7	10%
3000 W	20	Non uniform	7	10%

Table 5.16: Different heating time, z = 2 mm, cylindrical sample.

Depth 2 mm				
D = 8 mm				
Input power [W]	Heating time [s]	Heating type	Number of $f_{\Delta\Phi max}$	Percentage Error
1000 W	10	Uniform	10	14%
1000 W	10	Non uniform	10	14%
1000 W	20	Uniform	11	10%
1000 W	20	Non uniform	11	10%
3000 W	10	Uniform	10	14%
3000 W	10	Non uniform	10	14%
3000 W	20	Uniform	12	2%
3000 W	20	Non uniform	12	2%
D = 4 mm				
Input power [W]	Heating time [s]	Heating type	Number of $f_{\Delta\Phi max}$	Percentage Error
1000 W	10	Uniform	16	16%
1000 W	10	Non uniform	16	16%
1000 W	20	Uniform	11	10%
1000 W	20	Non uniform	11	10%
3000 W	10	Uniform	15	15%
3000 W	10	Non uniform	15	15%
3000 W	20	Uniform	13	5%
3000 W	20	Non uniform	12	2%
D = 2 mm				
Input power [W]	Heating time [s]	Heating type	Number of $f_{\Delta\Phi max}$	Percentage Error
1000 W	10	Uniform	16	16%
1000 W	10	Non uniform	16	16%
1000 W	20	Uniform	11	10%
1000 W	20	Non uniform	11	10%
3000 W	10	Uniform	15	15%
3000 W	10	Non uniform	15	15%
3000 W	20	Uniform	13	5%
3000 W	20	Non uniform	13	5%

Table 5.17: Different heating time, z = 5 mm, cylindrical sample.

Depth 5 mm				
D = 8 mm				
Input power [W]	Heating time [s]	Heating type	Number of $f_{\Delta\Phi max}$	Percentage Error
1000 W	10	Uniform	3	8%
1000 W	10	Non uniform	3	8%
1000 W	20	Uniform	3	8%
1000 W	20	Non uniform	3	8%
3000 W	10	Uniform	3	8%
3000 W	10	Non uniform	3	8%
3000 W	20	Uniform	3	8%
3000 W	20	Non uniform	3	8%
D = 4 mm				
Input power [W]	Heating time [s]	Heating type	Number of $f_{\Delta\Phi max}$	Percentage Error
1000 W	10	Uniform	2	29%
1000 W	10	Non uniform	2	29%
1000 W	20	Uniform	3	8%
1000 W	20	Non uniform	3	8%
3000 W	10	Uniform	2	29%
3000 W	10	Non uniform	2	29%
3000 W	20	Uniform	3	8%
3000 W	20	Non uniform	3	8%

Table 5.18: Different heating time, z = 4 mm, cylindrical sample.

Depth 4 mm				
D = 8 mm				
Input power [W]	Heating time [s]	Heating type	Number of $f_{\Delta\Phi max}$	Percentage Error
1000 W	10	Uniform	4	7%
1000 W	10	Non uniform	4	7%
1000 W	20	Uniform	4	7%
1000 W	20	Non uniform	4	7%
3000 W	10	Uniform	4	7%
3000 W	10	Non uniform	4	7%
3000 W	20	Uniform	4	7%
3000 W	20	Non uniform	4	7%
D = 6 mm				
Input power [W]	Heating time [s]	Heating type	Number of $f_{\Delta\Phi max}$	Percentage Error
1000 W	10	Uniform	3	14%
1000 W	10	Non uniform	3	14%
1000 W	20	Uniform	4	7%
1000 W	20	Non uniform	4	7%
3000 W	10	Uniform	3	14%
3000 W	10	Non uniform	3	14%
3000 W	20	Uniform	4	7%
3000 W	20	Non uniform	4	7%
D = 4 mm				
Input power [W]	Heating time [s]	Heating type	Number of $f_{\Delta\Phi max}$	Percentage Error
1000 W	10	Uniform	3	14%
1000 W	10	Non uniform	3	14%
1000 W	20	Uniform	3	14%
1000 W	20	Non uniform	3	14%
3000 W	10	Uniform	3	14%
3000 W	10	Non uniform	3	14%
3000 W	20	Uniform	3	14%
3000 W	20	Non uniform	3	14%

Table 5.19: Different heating time, z = 8 mm, cylindrical sample, minimum frequency 4.8e-4 Hz.

Depth 8 mm				
D = 8 mm (minimum frequency 4.845e-4)				
Input power [W]	Heating time [s]	Heating type	Number of $f_{\Delta\Phi max}$	Percentage Error
1000 W	10	Uniform	2	6%
1000 W	10	Non uniform	2	6%
1000 W	20	Uniform	2	6%
1000 W	20	Non uniform	2	6%
3000 W	10	Uniform	2	6%
3000 W	10	Non uniform	2	6%
3000 W	20	Uniform	2	6%
3000 W	20	Non uniform	2	6%

Table 5.20: Different heating time, z = 8 mm, cylindrical sample, minimum frequency 8.3e-4.

Depth 8 mm				
D = 8 mm (minimum frequency 8.3e-4 Hz)				
Input power [W]	Heating time [s]	Heating type	Number of $f_{\Delta\Phi max}$	Percentage Error
1000 W	10	Uniform	2	18%
1000 W	10	Non uniform	2	18%
1000 W	20	Uniform	2	18%
1000 W	20	Non uniform	2	18%
3000 W	10	Uniform	2	18%
3000 W	10	Non uniform	2	18%
3000 W	20	Uniform	2	18%
3000 W	20	Non uniform	2	18%

As it can be seen, the considerations made in section 5.1 still hold: when the flaw is located at a huge depth under the external surface, the optimum visibility frequency is found in the lower band of the spectrum. Thus, even a minor stimulus is able to give the correct amount of energy to excite it.

Chapter 6
Final outcomes

6.1 Experimental results

Considering all the passages described in section 4.5, it becomes possible the characterization of the experimental flaws exploiting the images obtained with the application of the geometric and emissivity considerations. First of all, the whole image is taken into account, applying the Fourier transform, which allows the passage from the time domain to the frequency domain. In this way it is possible to compute the phase of each pixel. The obtained image is, then, post-processed applying the operations described in section 4.3. The result is displayed in Figure 6.1. As it can be seen, the flaws are clearly visible, except the one located in the highest part of the sample, characterized by a diameter of 2 mm and a depth of 2 mm. Thus, it is decided to restrict the area of analysis, limiting it to a square of 40x40 pixels centred on each flaw. The correlation criterion is exploited to find the value of the optimum visibility frequency, on which the identification of the depth is possible, exploiting formula 4.2. The following figures show, for each flaw, the filtered phase diagrams. The value of the correlation number is shown, in order to give an example, for the flaw with a diameter of 8 mm and a depth of 5 mm. The estimated depth is shown in Table 6.1.

Table 6.1: Experimental results on the flaws.

Diameter [m^{-3}]	Depth [m^{-3}]	Estimated depth [m^{-3}]	Percentage Error
2	2	(not available)	-
8	5	4.6	8%
4	5	4.6	8%
8	8	6.5	18%
4	2	2.6	23%

As it can be seen, only one flaw is not detected by this analysis. In the other cases, the error is low, especially for the flaw characterized by a higher depth. The defect characterized by a diameter of 8 mm and a depth of 8 mm deserves a particular remark. The estimated depth is the highest allowed by the chosen resolution in frequency. For this reason, the error of 20% could be caused by this aspect rather than by the technique itself.

It is important to highlight that the fact that the previous analysis has been conducted considering a little squared area centred on the flaw does not bind the procedure. It is proved that the flaws are identified also taking into account a wider area around it. In addition to this fact, it is also important to underline that the developed program has a video interface that enables the user to select the zone of interest on which the analysis is conducted.

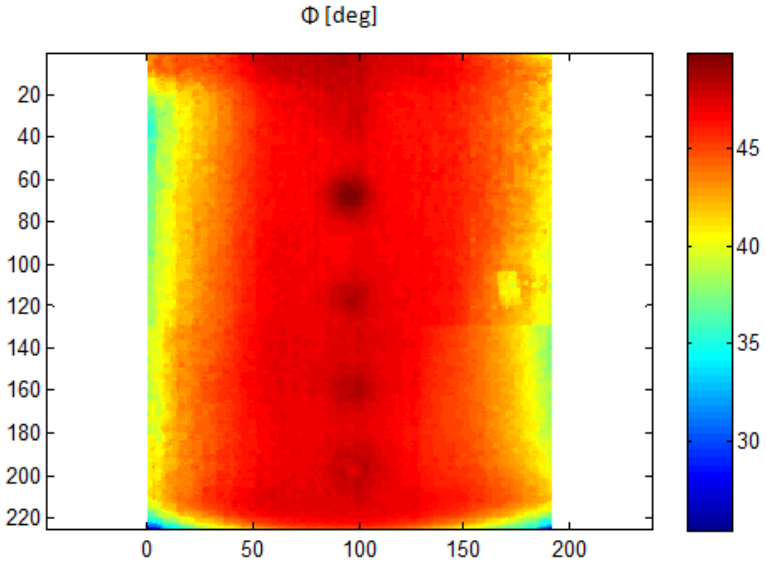

Figure 6.1: Whole cylinder, Φ filtered.

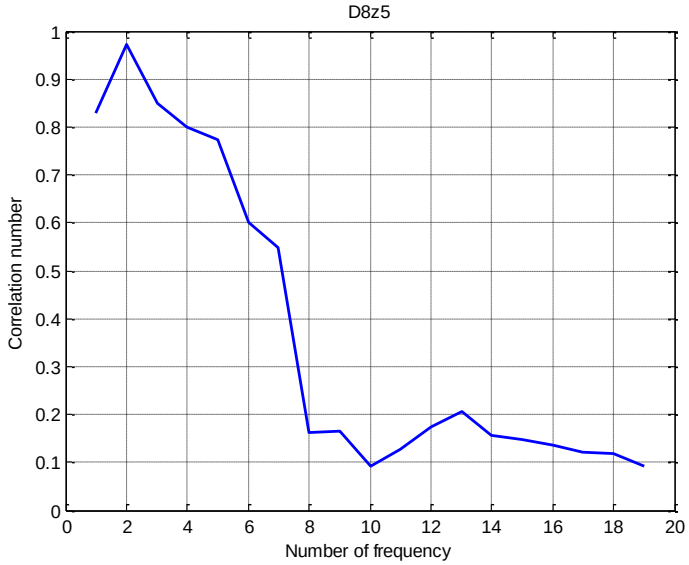

Figure 6.2: D8z5, correlation.

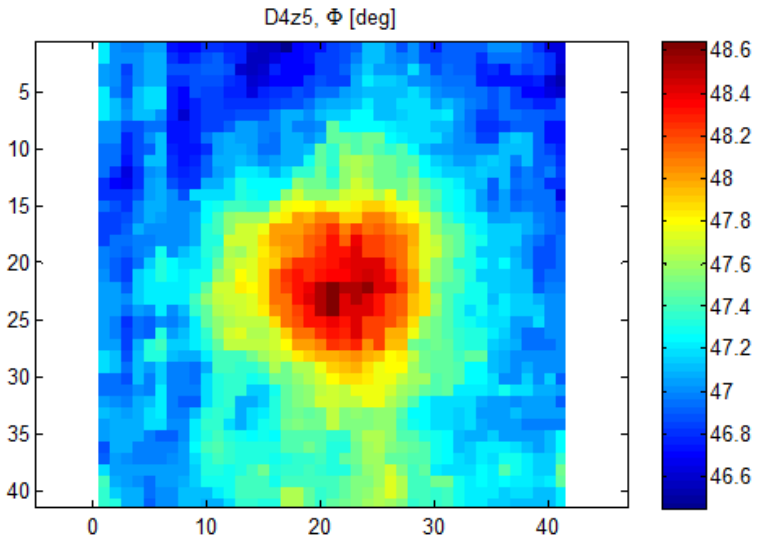

Figure 6.3: D4z5, Φ filtered.

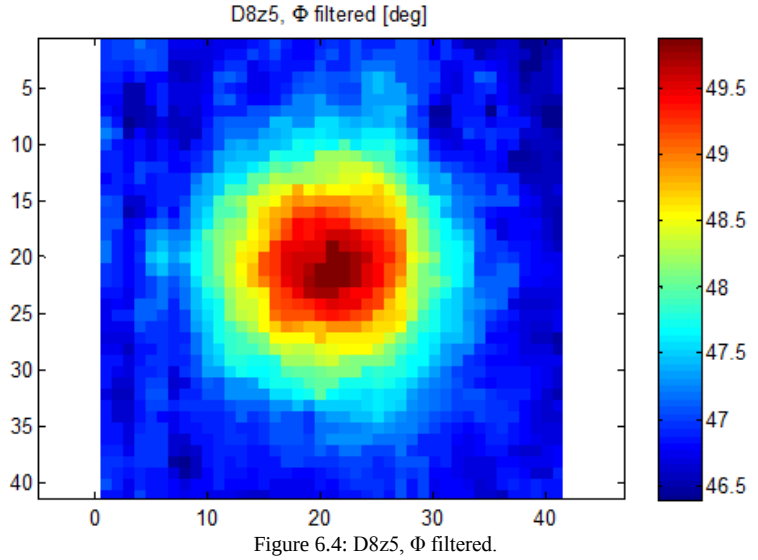

Figure 6.4: D8z5, Φ filtered.

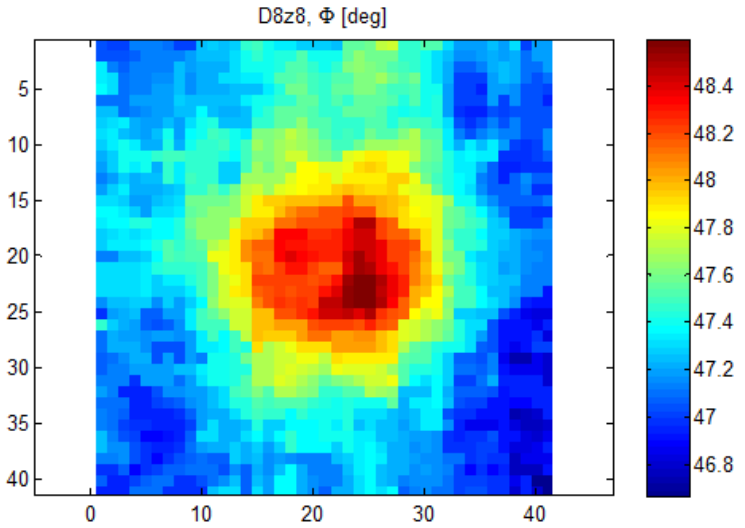

Figure 6.5: D8z8, Φ filtered.

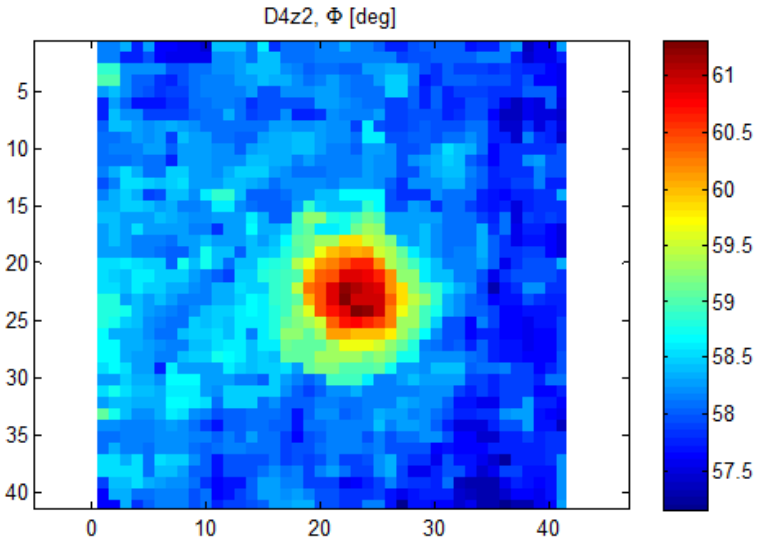

Figure 6.6: D4z2, Φ filtered.

6.2 Numerical results

Owing to the outcomes obtained in section 5.3.1, the numerical simulations are conducted by setting the simulation parameters to the values in Table 6.2:

Table 6.2: Parameters of the numerical simulations.

Parameter	Value
Heating time	20 s
I	3000 W
$\Delta T_{\text{heating start - heating end}}$	25 °C
Time step heating stage	0.01 s
Observation time	1200 s
Time step cooling stage	1 s

Table 6.3: Results on cylindrical sample, experimental flaws.

Flaw	Heating type	Defect geometry		Maximum ΔΦ			Estimated depth [m^{-3}]	Percentage Error
		Depth [m^{-3}]	Diameter [m^{-3}]	Value [deg] (Absolute value)	Number of freq	f [Hz^{-3}]		
Air	Uniform	5	8	2.52	3	1.7	4.6	8%
Air	Non uniform	5	8	2.66	3	1.7	4.6	8%
Air	Uniform (4.8e-4 Hz)	8	8	2.33	2	0.48	8.5	6%
Air	Non uniform (4.8e-4 Hz)	8	8	2.90	2	0.48	8.5	6%
Air	Uniform	8	8	1.25	2	0.83	6.5	18%
Air	Non uniform	8	8	1.42	2	0.83	6.5	18%
Air	Uniform	5	4	2.14	3	1.7	4.6	8%
Air	Non uniform	5	4	2.35	3	1.7	4.6	8%
Air	Uniform	2	4	5.35	13	10	1.9	5%
Air	Non uniform	2	4	5.26	12	9.1	1.95	2%
Air	Uniform	2	2	2.12	13	10	1.9	5%
Air	Non uniform	2	2	2.46	13	10	1.9	5%

As it can be seen in Table 6.3, the results do not change considering a uniform or a non uniform heating, except in one case. The difference in the estimated depth in such case is ascribed to different values of the optimum visibility frequency, the highest value of which is bigger than the other by only one unity. The fact that the correspondent error becomes higher is due to the discretization in frequency linked to the observation time. It is, thus, supposed that the different estimated depths are not caused by a different behaviour of the specimen with regard to the kinds of applied heating.

Other tests are conducted to establish how the technique fit to the identification of flaws, in order to generalize the analysis.

Table 6.4: Results on cylindrical sample, 20 W for 20 s, other flaws.

Flaw	Heating type	Defect geometry		Maximum ΔΦ			Estimated depth [m^{-3}]	Percentage Error
		Depth [m^{-3}]	Diameter [m^{-3}]	Value [deg] (absolute value)	Number of freq	f [Hz^{-3}]		
Air	Uniform	2	8	12.39	12	9.10	1.95	2%
Air	Non uniform	2	8	11.22	12	9.1	1.95	2%
Air	Uniform	3	8	7.97	6	4.2	2.9	3%
Air	Non Uniform	3	8	8.09	6	4.2	2.9	3%
Air	Uniform	4	8	4.25	4	2.5	3.7	7%
Air	Non Uniform	4	8	5.46	4	2.5	3.7	7%
Air	Uniform	3	6	2.61	7	5	2.7	10%
Air	Non Uniform	3	6	2.78	7	5	2.7	10%
Air	Uniform	4	6	2.01	4	2.5	3.7	7%
Air	Non Uniform	4	6	2.39	4	2.5	3.7	7%
Air	Uniform	4	4	1.23	3	1.7	4.6	14%
Air	Non Uniform	4	4	1.77	3	1.7	4.6	14%

The simulation has proved that, taking into consideration different flaws, characterized by various diameters and depths, the error is less than 10% in the majority of the cases. As it can be seen, the larger the diameter, the better the identification, even if the ratio between diameter and depth decreases.
Figure 6.7, Figure 6.8 and Figure 6.9 show the phase difference, as an example, for the flaw with a diameter of 8 mm and a depth of 2 mm. It can be seen that the phase difference in correspondence to the flaws tends to increase. The oscillations are due to the adopted mesh, as it is said in section 5.2.1.

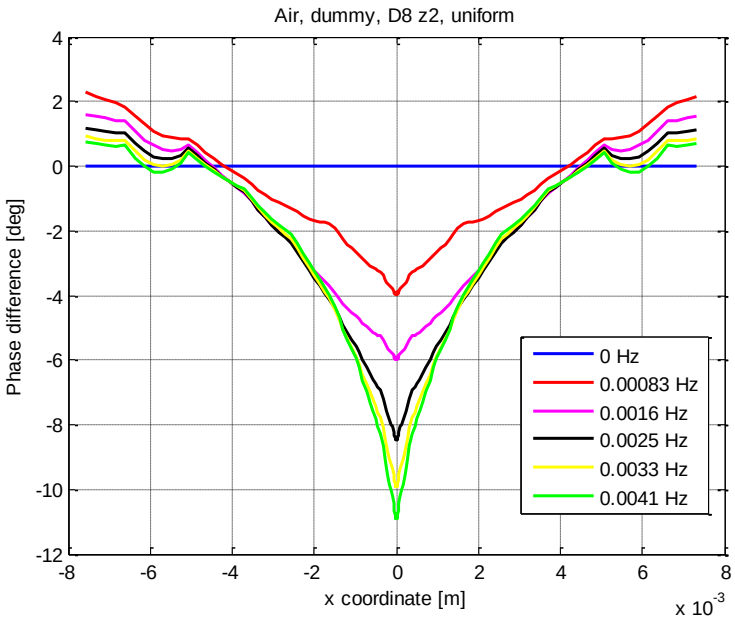

Figure 6.7: Phase difference, D8z2, 0-0.0041 Hz, central part.

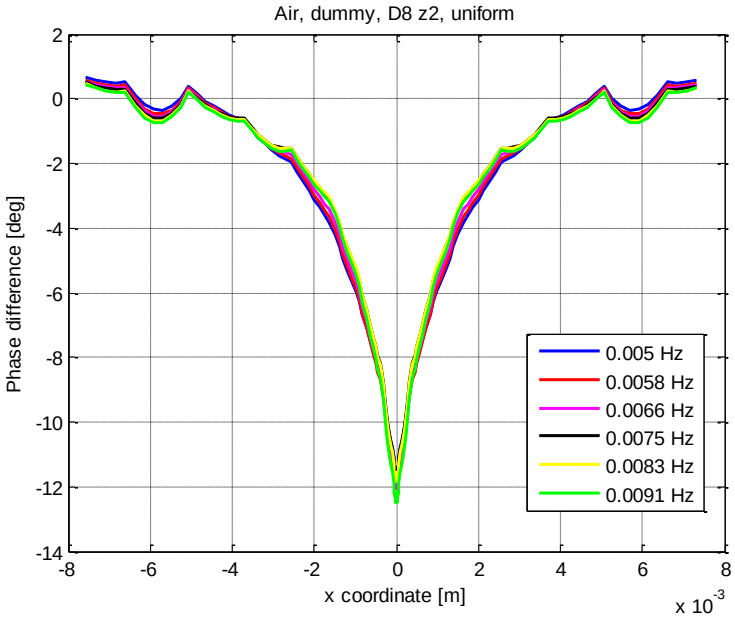

Figure 6.8: Phase difference, D8z2, 0.005-0.0091 Hz, central part.

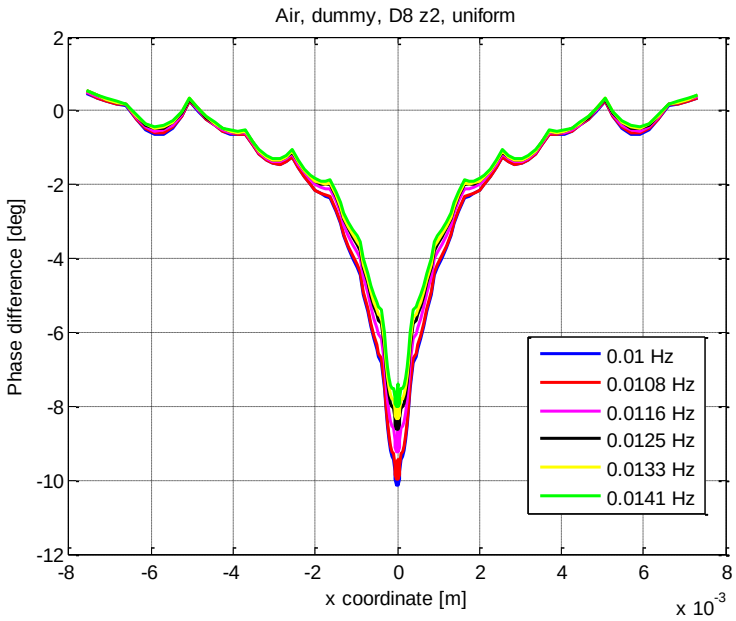

Figure 6.9: Phase difference, D8z2, 0.01-0.0141 Hz, central part.

Making a comparison between different flaws, characterized by the same diameter, it can be easily recognized that the deeper the defects, the lower the value of the phase difference and of the corresponding frequency. This confirms the correctness of the exploited method: different depths give rise to different optimum visibility frequency, in such a way that it seems an effective technique to base the identification of the depth on this parameter. This aspect was found also in the previous works, [22] [23], for 20 mm and 4 mm depth sample. Regarding the behaviour of the phase difference with respect to different diameters, it is not possible to make a univocal remark. Indeed, as it can be seen in the previous tables, the maximum phase difference value has not a constant trend in flaws characterized by different diameter located at the same depth: to give an example, the 5 mm depth defects are characterized by the same value of the optimum visibility frequency and the corresponding value of the maximum phase difference varies according to the diameter size; on the other hand, taking into consideration the 3 mm flaws, the error in the found depth is higher with a smaller diameter. This aspect deserves to be closely examined, it could be a significant result basing on which it is possible to find a method useful to determine the diameter. This aspect is confirmed also by [38], where the characterization of the diameter is based on the *full width at half maximum* evaluation of the line profiles of the temperature across the defect in the horizontal and vertical direction, as it is stated in [48].

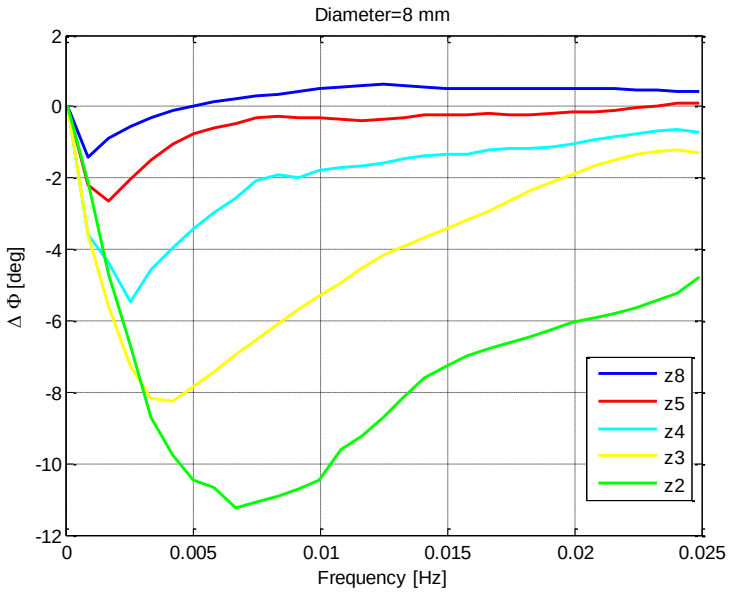

Figure 6.10: Phase difference, comparison between flaws with different depths.

Other tests are conducted considering different materials of the flaws. In this way, the ability in the characterization of the depth of the flaw is tested also with different reflection coefficient between the material of the sample and the one of the flaw. With an interface Plexiglass – Air the *r* coefficient is close to 1. Two different cases are analyzed, assuming its value equal to 0.9 and to 0.75. Results are shown in Table 6.5.

Table 6.5: Results regarding different reflection coefficient.

r̂	Heating type	Defect geometry		Maximum ΔΦ			Estimated depth [m^{-3}]	Percentage Error
		Depth [m^{-3}]	Diameter [m^{-3}]	Value [deg] (absolute value)	Number of freq	f [Hz^{-3}]		
0.9	Non uniform	2	2	4.26	14	10.8	1.8	10%
0.75	Non uniform	2	2	3.38	15	11.7	1.7	13%
0.9	Non uniform	2	4	4.93	13	10	1.9	5%
0.75	Non uniform	2	4	4.83	15	11.7	1.7	13%
0.9	Non uniform	4	4	1.19	3	1.7	4.6	14%
0.75	Non uniform	4	4	1.07	3	1.7	4.6	14%
0.9	Non uniform	5	4	1.26	2	0.83	6.5	30%
0.75	Non uniform	5	4	1.35	2	0.83	6.5	30%
0.9	Non uniform	3	6	4.17	7	5	2.7	10%
0.75	Non uniform	3	6	3.16	7	5	2.7	10%
0.9	Non uniform	4	6	2.04	4	2.5	3.7	7%
0.9	Non uniform	4	6	1.98	4	2.5	3.7	7%
0.9	Non uniform	2	8	9.75	12	9.1	1.95	2%
0.75	Non uniform	2	8	7.62	12	9.1	1.95	2%
0.9	Non uniform	3	8	6.11	7	5.0	2.7	10%
0.75	Non uniform	3	8	4.48	7	5.0	2.7	10%
0.9	Non uniform	4	8	3.07	4	2.5	3.7	6%
0.75	Non uniform	4	8	2.23	3	1.7	4.6	13%
0.9	Non uniform	5	8	4.11	2	0.83	6.5	30%
0.75	Non uniform	5	8	3.79	2	0.83	6.5	30%

As it can be seen in the previous table, the technique suits even in the case of samples characterized by flaws composed by different materials. In the majority of the cases, the error is inferior to 15%. A particular remark regards the flaws characterized by a depth of 5 mm, which origins the greatest errors. As it is

stated before, the values of the thermal diffusion lengths corresponding to the higher frequencies vary greatly between one frequency and the other one. Thus, a small difference in the optimum visibility frequency brings to a significant error: if its value was decreased by one unity, the found depth would be 4.6 mm instead of 6.5 mm, characterized by an error of 8% rather than 30%. The errors remain limited especially when the coefficient *r* is closer to 1. When the flaw has a huge dimension, in general, the technique leads to a better identification, even when the *r* coefficient is low.

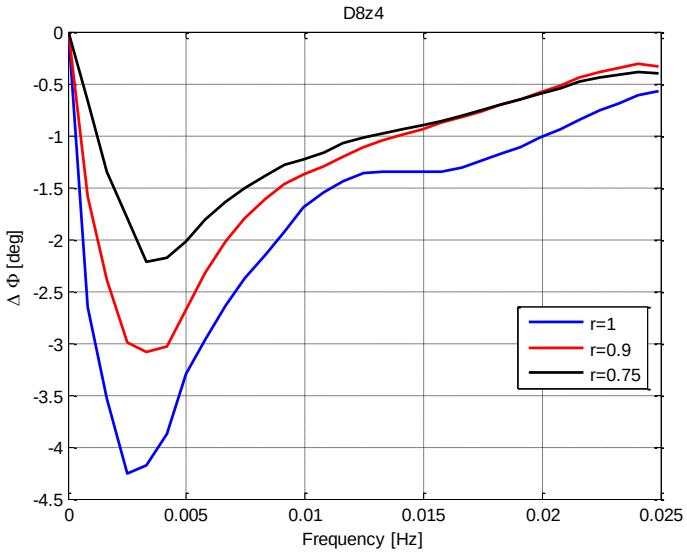

Figure 6.11: Phase difference, comparison between flaws with different reflection coefficients.

6.3 Comparison between experimental and numerical results

The following table reports the estimated depths in the numerical and in the experimental cases, in order to simplify the comparison.

Table 6.6: Comparison between numerical and experimental results.

Type of the analysis	Defect geometry		Estimated depth [m^{-3}]	Percentage Error
	Depth [m^{-3}]	Diameter [m^{-3}]		
Experimental	5	8	4.6	8%
Numerical	5	8	4.6	8%
Experimental	8	8	6.5	18%
Numerical	8	8	6.5	18%
Experimental	5	4	4.6	8%
Numerical	5	4	4.6	8%
Experimental	2	4	2.6	23%
Numerical	2	4	2	2%
Experimental	2	2	-	-
Numerical	2	2	1.9	6%

As it can be seen from a comparison with the experimental flaws, the estimated depth is the same for the three deepest defects, while the experimental simulation identifies a worst value in the case of a flaw with a diameter of 4 mm and a depth of 2 mm. Obviously, in the numerical simulation it is identifiable also the smallest flaw, not seen in the experimental test. The following figures show a comparison between the phase difference at the centre of the flaw in the numerical simulation and in the experimental test. As it can be seen from Figure 6.13 to Figure 6.15, the numerical and experimental trends of the phase difference do not perfectly overlap; for the three deepest flaws their maximum values occur at the same frequency value, leading to the same estimated depth, but their trend is different. This difference increases in the case of the flaw with a diameter and a thickness, respectively, of 4 mm and 2 mm. The causes that bring to this behaviour have to be closely examined in future developments.

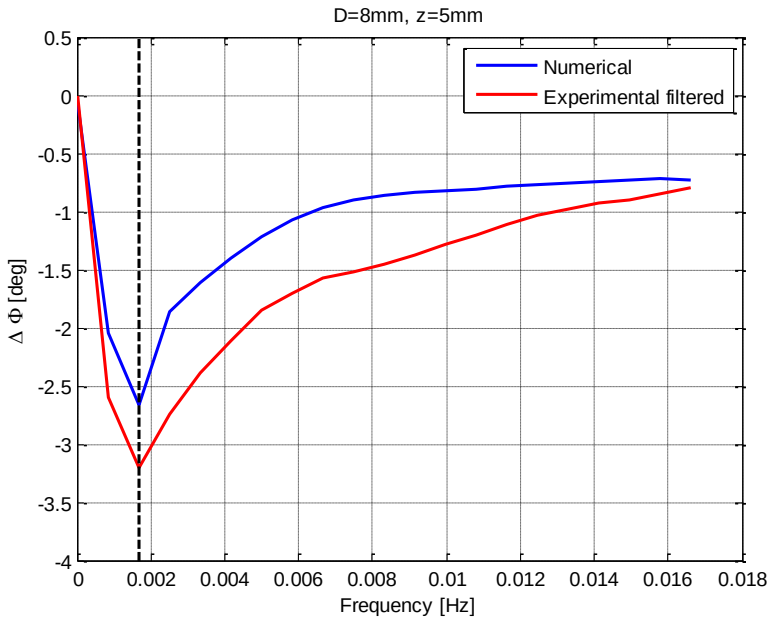

Figure 6.12: Phase difference, D8z5, comparison between numerical and experimental simulations.

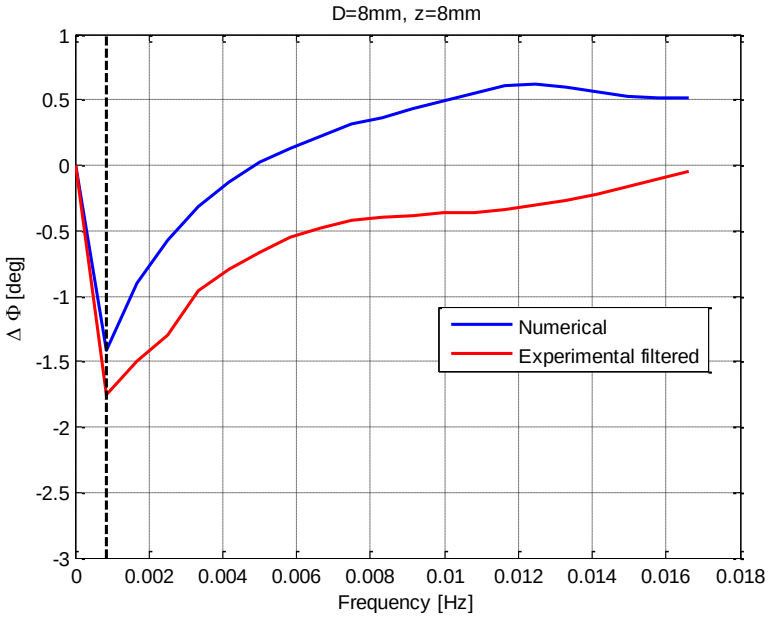

Figure 6.13: Phase difference, D8z8, comparison between numerical and experimental simulations.

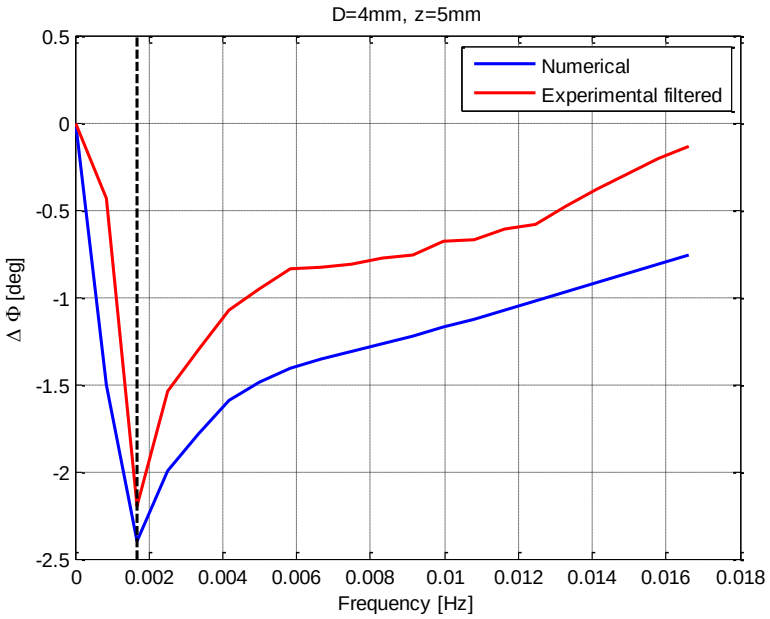

Figure 6.14: Phase difference, D4z5, comparison between numerical and experimental simulations.

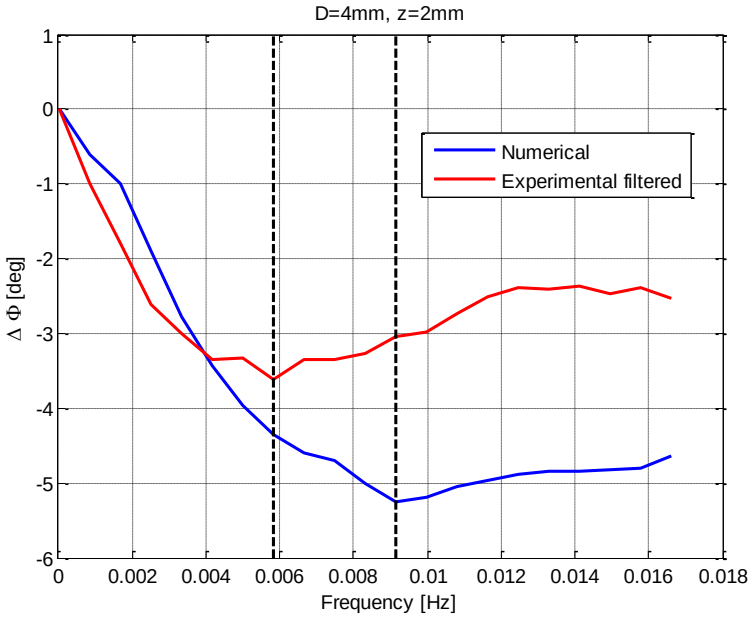

Figure 6.15: Phase difference, D4z2, comparison between numerical and experimental simulations.

It is important to highlight that the new heating apparatus reveals itself to be effective even making a comparison between the experimental results obtained in this work and the ones of the previous work. Taking into consideration the flaw analyzed also in [22] and in [23], considering the estimated depth obtained in the same experimental set-up, even if with different sample, it can be seen that the error for the D4z2 flaw is cut in half, from 40% to 23%.

6.4 Conclusions and future developments

This thesis work has proved the feasibility of the *Pulse Phase Thermography* technique in the characterization of the depth of flaws in non-straight samples. The depth of defects in a cylindrical sample is characterized starting from the procedures developed in the previous works, [22], [23], [40]. These previous works have been focused on specimens characterized by a thickness of 20 mm or 4 mm, therefore a sample approximated with a semi-infinite media or a very thin sample; the thickness of the specimen analyzed in this thesis is 10 mm, between the thickness of the previous analyzed samples. An important result of this work is the demonstration of the feasibility of the technique utilized by the ThermALab in such area of expertise, for defects in different geometry. On the other hand, it is found that, even if the general procedure suits to the analyzed

problem, its parameters have to be accurately evaluated and adapted to the different examined geometries. Indeed, the difference in the phase difference trend could be probably ascribed to this aspect. With a proper calibration of such parameters, maybe this difference could decrease.
One of the most important outcomes of this work is the developing of an automated procedure to analyze the mentioned cylindrical shape specimens. A program able to make morphological operations on the images acquired by the infrared camera is realized, in such a way that an image representative of the height and of the circumference of the cylinder is obtained. Starting from several experimental tests, different parameters useful in this analysis have been set up, such as the emissivity value at different angles of observation or the out-of-focus effects, values that are inserted in the program in order to correctly evaluate the behaviour of such kind of samples.
The heating apparatus of the ThermALab has been improved, passing from a system constituted by two halogen 500 W lamps to a device made by six lamps, equal to the previous lamps, so that it is able to provide an output power of 3000 W. In order to find the optimum value of the heating duration suitable for this new geometry with the new heating apparatus, several numerical simulations have been conducted. These tests take, as a sort of starting guess, the values found by Vitali in [23]. Other numerical simulations have been conducted both to test the applicability of the technique even in flaws constituted by materials different from air, and, so, with a reflection coefficient lower than the one of the air, and to prove the independence of the *Pulse Phase Thermography* technique on the non-uniformity of the heating.
Future developments have to be focused, primarily, on an increasing of the experimental tests on the sample maintained at a fixed temperature in order to better characterize the variations in the emissivity value depending on the angle of observation, especially in the range comprised between 60° and 75°. In addition to this fact, it would be necessary to carry on other experimental campaigns analyzing other kinds of flaws. In this way, it would be possible both to properly calibrate the parameters exploited in the program able to identify the depth and to characterize the limits of the dimension of the flaws that the technique can identify. Once that these have been identified, a technique for the identification of the diameter has to be found, which has to be different from the one adopted until now. Indeed, starting from the results obtained in the numerical simulations, it has been proved that in such kind of specimens the optimum visibility frequency of flaws with constant depths and different diameter could vary, even if the variation is small. Thus, another parameter has to be taken into account. Future developments could be focused on the evaluation of the *full width at half maximum* principle, as [38] and [48] suggest.
It is important to point out that all the new tests have to be conducted by exploiting an external coating of each sample with the same optical properties of the utilized one, in order to obtain the same comparable experimental values.

The morphological reconstruction done in this work takes into account issues related exclusively to a cylindrical shape. Starting from the results obtained in this thesis, it is possible to develop a more generalized procedure able to characterize flaws in different 3d geometries.

Appendix A

Evaluation of standard deviations at fixed temperature

The following tables show the standard deviations for all the measures shown in section 4.4.

Table A.1: Standard deviations [°C], test at a fixed temperature, 0° and 30°.

0°							
Square regions							
	Total	2x2	3x3	5x5	9x9	21x21	
	0.16	0.01	0.04	0.04	0.04	0.04	
Rectangular regions: columns							
	1 column	3 columns	5 columns	9columns	15 columns	21 columns	31 columns
Total	0.03	0.03	0.04	0.04	0.04	0.04	0.04
3 pixels	-	0.04	0.04	0.04	0.03	0.03	0.03
11 pixels	-	0.04	0.04	0.04	0.03	0.03	0.03
21 pixels	-	0.04	0.04	0.04	0.03	0.03	0.03
31 pixels	-	0.04	0.04	0.03	0.03	0.03	0.03

30°							
Square regions							
	Total	2x2	3x3	5x5	9x9	21x21	
	0.16	0.07	0.07	0.07	0.07	0.06	
Rectangular regions: columns							
	1 column	3 columns	5 columns	9columns	15 columns	21 columns	31 columns
Total	0.05	0.05	0.06	0.06	0.06	0.06	0.06
3 pixels	-	0.06	0.05	0.05	0.05	0.05	0.04
11 pixels	-	0.05	0.05	0.05	0.05	0.05	0.04
21 pixels	-	0.05	0.05	0.05	0.05	0.05	0.04
31 pixels	-	0.05	0.05	0.05	0.05	0.04	0.04

Table A.2: Standard deviations [°C], test at a fixed temperature, 45° and 60°.

45°							
Square regions							
	Total	2x2	3x3	5x5	9x9	21x21	
	0.19	0.07	0.07	0.07	0.07	0.07	
Rectangular regions: columns							
	1 column	3 columns	5 columns	9 columns	15 columns	21 columns	31 columns
Total	0.07	0.06	0.06	0.06	0.06	0.07	0.06
3 pixels	-	0.06	0.05	0.05	0.05	0.05	0.05
11 pixels	-	0.06	0.05	0.05	0.05	0.05	0.05
21 pixels	-	0.05	0.05	0.05	0.05	0.05	0.05
31 pixels	-	0.05	0.05	0.05	0.05	0.05	0.04

60°							
Squared regions							
	Total	2x2	3x3	5x5	9x9	21x21	
	0.17	0.13	0.13	0.13	0.13	0.13	
Rectangular regions: columns							
	1 column	3 columns	5 columns	9 columns	15 columns	21 columns	31 columns
Total	0.07	0.07	0.07	0.06	0.06	0.06	0.06
3 pixels	-	0.06	0.06	0.06	0.06	0.06	0.06
11 pixels	-	0.06	0.06	0.06	0.06	0.06	0.06
21 pixels	-	0.06	0.06	0.06	0.06	0.06	0.06
31 pixels	-	0.06	0.06	0.06	0.06	0.06	0.06

Table A.3: Standard deviations [°C], test at a fixed temperature, 75°.

75°						
Square regions						
	Total	2x2	3x3	5x5	9x9	21x21
	0.19	0.16	0.16	0.16	0.15	0.16

Rectangular regions: columns

	1 column	3 columns	5 columns	9 columns	15 columns	21 columns	31 columns
Total	0.11	0.10	0.08	0.07	0.06	0.06	0.08
3 pixels	-	0.08	0.09	0.09	0.09	0.09	0.09
11 pixels	-	0.08	0.08	0.08	0.08	0.08	0.08
21 pixels	-	0.08	0.08	0.08	0.08	0.08	0.08
31 pixels	-	0.08	0.08	0.08	0.08	0.08	0.08

Appendix B

Solution of the Fourier equation with the method of separation of variables

A semi-infinite medium, whose behaviour is described by the Fourier's equation,

$$\frac{\partial^2}{\partial z^2}(T) = \frac{1}{\alpha}\frac{\partial T}{\partial t} \tag{B.1}$$

is taken into account. It is subjected to an applied surface temperature that oscillates around a certain value T_m. It is possible to describe it introducing a value ϑ, defined as:

$$\vartheta = T - T_m. \tag{B.2}$$

Thus, the boundary condition can be seen as:

$$\vartheta(0, t) = \vartheta_0(t) = \vartheta_0 \cos(\omega t). \tag{B.3}$$

The Fourier's equation becomes:

$$\frac{\partial^2}{\partial z^2}(\vartheta) = \frac{1}{\alpha}\frac{\partial \vartheta}{\partial t}. \tag{B.4}$$

The problem can be solved considering the method of the separation of variables, assuming a solution in the form:

$$\vartheta(z, t) = Z(z)\tau(t). \tag{B.5}$$

So,

$$\frac{1}{\alpha} Z\dot{\tau} = Z''\tau, \tag{B.6}$$

where the apostrophe indicates a space derivative, while the point a time derivative. Dividing by ϑ, the following form is obtained:

$$\frac{1}{\alpha}\frac{\dot{\tau}}{\tau} = \frac{Z''}{Z}, \tag{B.7}$$

implicating that each of the two parts has to be constant.

$$\int \frac{\dot{\tau}}{\tau} = \int C_1 \alpha dt, \ln \tau = C_1 \alpha t + C', \tau = e^{C_1 \alpha t} e^{C'} = e^{C_1 \alpha t} C\,. \tag{B.8}$$

It can be easily noticed that C_1 has to be complex, $C_1 = \mu \pm i\lambda^2$. μ has to be equal to 0, so

$$\begin{cases} \tau^+ = Ce^{i\lambda^2 \alpha t} \\ \tau^- = Ce^{-i\lambda^2 \alpha t} \end{cases}. \tag{B.9}$$

Considering the part of the equation referred to the Z component,

$$\begin{cases} Z^{+\prime\prime} - i\lambda^2 Z = 0 \\ Z^{-\prime\prime} + i\lambda^2 Z = 0 \end{cases}, \tag{B.10}$$

which is an ordinary differential equation with constant coefficients. Solving its characteristics equation, it is obtained that

$$\begin{aligned} Z^+ &= C_1' e^{z_1 z} + C_2' e^{z_2 z} \\ Z^- &= C_3' e^{z_3 z} + C_4' e^{z_4 z}, \end{aligned} \tag{B.11}$$

where $z_{1,2} = \pm\sqrt{i\lambda^2} = \pm\lambda\sqrt{i}$ and $z_{3,4} = \pm\sqrt{i\lambda^2} = \pm\lambda\sqrt{-i}$.
Thus,

$$\vartheta = C_1 e^{\left(i\lambda^2 \alpha t + \frac{\lambda z}{\sqrt{2}} + \frac{i\lambda z}{\sqrt{2}}\right)} + C_2 e^{\left(i\lambda^2 \alpha t - \frac{\lambda z}{\sqrt{2}} - \frac{i\lambda z}{\sqrt{2}}\right)} + C_3 e^{\left(-i\lambda^2 \alpha t - \frac{\lambda z}{\sqrt{2}} + \frac{i\lambda z}{\sqrt{2}}\right)} + C_4 e^{\left(-i\lambda^2 \alpha t + \frac{\lambda z}{\sqrt{2}} - \frac{i\lambda z}{\sqrt{2}}\right)}. \tag{B.12}$$

Considering that λ is assumed to be positive, since the terms related to C_1 and C_4 tends to diverge when z increases, they are posed equal to 0. Applying the *Euler's formula*,

$$\vartheta = e^{-\frac{\lambda z}{\sqrt{2}}}\left[(C_2 + C_3)\cos\left(\lambda^2 \alpha t - \frac{\lambda z}{\sqrt{2}}\right) + i(C_2 - C_3)\sin\left(\lambda^2 \alpha t - \frac{\lambda z}{\sqrt{2}}\right)\right]. \tag{B.13}$$

Applying the boundary conditions, it is obtained that:

$$\vartheta(0, t) = 1[(C_2 + C_3)\cos(\lambda^2 \alpha t - 0) + i(C_2 - C_3)\sin(\lambda^2 \alpha t - 0)] == \vartheta_0 \cos(\omega t). \tag{B.14}$$

Thus, $\begin{cases} C_2 = C_3 = \frac{\vartheta_0}{2} \\ \lambda^2\alpha = \omega, \lambda = \pm\sqrt{\frac{\omega}{\alpha}} \end{cases}$.

Thus, introducing the *wave number* $\hat{k}$, defined as $\frac{\lambda}{\sqrt{2}} = \frac{2\pi}{\hat{\lambda}} = \sqrt{\frac{\omega}{2\alpha}}$, where $\hat{\lambda}$ is the wavelength,

$$\vartheta(z,t) = e^{-\frac{\lambda z}{\sqrt{2}}}\vartheta_0 \cos\left(\lambda^2\alpha t - \frac{\lambda z}{\sqrt{2}}\right) = e^{-\hat{k}z}\vartheta_0 \cos(\omega t - \hat{k}z) \qquad (B.15)$$

and

$$T(z,t) = T_m - \vartheta_0 e^{-\hat{k}z}\cos(\omega t - \hat{k}z)\,. \qquad (B.16)$$

If a thermal heat flux is imposed, on the surface a temperature field with a delay of $\frac{\pi}{4}$ is found: assuming to apply the variables separation procedure, as it is previously shown, considering z=0, it is obtained that:

$$\Theta(z=0,t) = \Theta_0(\cos(\omega t)), \qquad (B.17)$$

while

$$q(z=0,t) = \sqrt{2}k\hat{k}\vartheta_0\left(\cos\left(\omega t + \frac{\pi}{4}\right)\right). \qquad (B.18)$$

These thermal waves are highly dispersive waves: the perturbation propagates instantly in all the object, due to parabolic nature of the Fourier equation, but the amplitude is exponentially reduced when the coordinate *z* increases. In addition to this fact, the perturbation comes with a delay that increases with z:

$$\varphi = \hat{k}z, \qquad (B.19)$$

where $\hat{k}$ is the *wave number*, previously defined.
Thus, on the surface there are the effects due both to the heat flux:

$$\Theta = \Theta_0(\cos(\omega t - \varphi)) \qquad (B.20)$$

and to the reflected wave:

$$\Theta = \Theta_0 e^{-2\hat{k}l}\left(\cos\left(\omega t - \frac{\pi}{4} - \varphi\right)\right). \quad \text{(B.21)}$$

This is a wave whose amplitude is added to the ones of the primary wave coming with a delay.

Appendix C

Development of the heating sources and of the cylindrical sample

As it is said in section 4.1.2, the heating source of the ThermALab has been improved. Figure C.1 show the developed heating device, able to give an increase in ΔT of 150%, as it is demonstrated in Figure C.2.

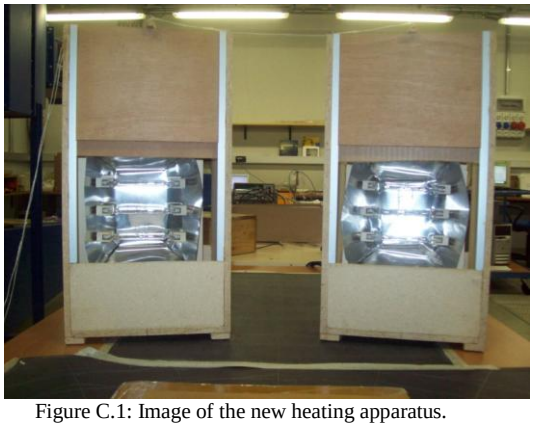

Figure C.1: Image of the new heating apparatus.

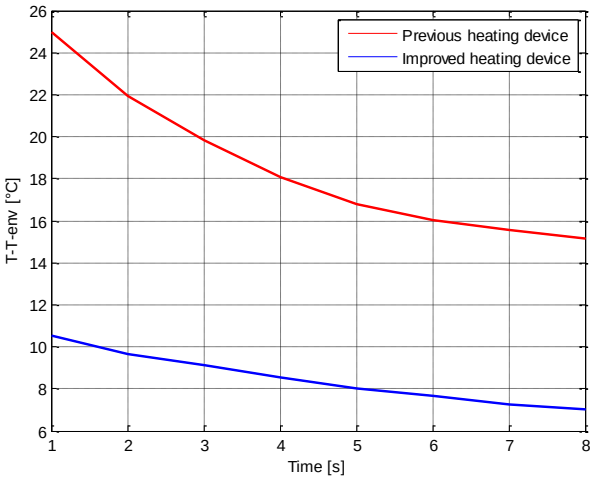

Figure C.2: Comparison between ΔT given by the two heating devices.

Regarding the cylindrical Plexiglas sample, in the following images the coating treatment and the flaws made are depicted.

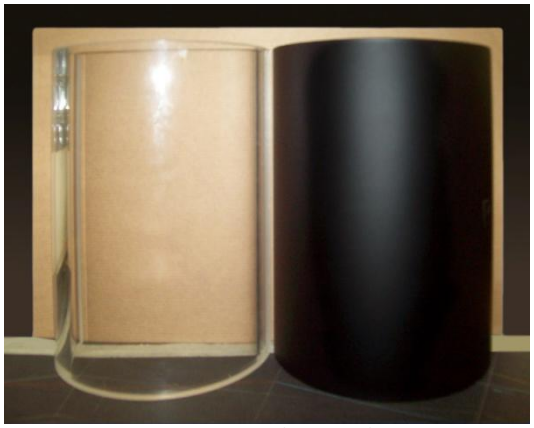

Figure C.3: Cylindrical sample, before and after the coating.

Figure C.4: Flaws on the cylindrical sample.

Appendix D

Analysis of the hyperbolic formulation of the heat conduction equation

Under the assumption of a local equilibrium, the hyperbolic equation obtained in Chapter 2 may conduce to a negative value of the entropy, in contrast with Clausius' inequality. To solve this problem, some authors have proposed different theories concerning a released of the assumption of local equilibrium. Some theories seem not so consistent [43], as the ones proposed by Gurtin and Pipkin [44] or the theory suggested by Coleman et al [45]. They, respectively, assume that the specific Helmholtz free energy ψ, the specific entropy s and the heat flux depend on temperature and the history both of temperature and of the gradient of temperature or that the specific internal energy u depends on q and on T. Jou et al. [46] propose an extension of the irreversible thermodynamics. They assume that the specific entropy s is a function of the heat flux density vector and of the specific internal energy u. In this theory, the entropy flux is given by the ratio between the heat flux and the non equilibrium temperature θ, in a condition of a non equilibrium state. Barletta and Zanchini [43] has, instead, demonstrate that it possible to find domain of application such that Cattaneo and Vernotte's formulation is valid under the assumption of a local equilibrium state. This occurs in the case of an entropy production rate per unit volume non negative at every point and at every time. More recent theories are based on the *thermomass* concept [15], based on the mass-energy duality of the heat, such that heat is seen as a substance with mass flowing in material thanks to a temperature difference. This aspect arises a new relation between heat and temperature field, describing a lagging time between them. Several numerical studies have been developed, exploiting, for example, the differential quadrature method [47].

Bibliography

1. C.J. HELLIER, *Handbook of non destructive evaluation*, Mc Graw-Hill, New York, 2003.

2. K. HALL, *Non destructive testing*, Department of Civil and Environmental Engineering, Illinois.

3. *http://www.engineershandbook.com/MfgMethods/ndt.htm.*

4. J. SCHLICHTING, CH. MAIERHOFER and M. KREUTZBRUCK, *Crack sizing by laser excited thermography*, NDT&E International, 45(2011), 133-140.

5. G. ZAUNER, G. MAYR and G. HENDORFER, *Wavelet-based subsurface defect characterization in pulsed phase thermography for non-destructive evaluation*, Proc. SPIE 7248, Wavelet Applications in Industrial Processing VI, 72480D (January 27, 2009); F. Truchtet, O. Laligant.

6. X. MALDAGUE, *Introduction to NDT by active infrared thermograph*, submitted 18.6.2002 to Materials Evaluation.

7. X. MALDAGUE, *Applications of infrared thermography in non-destructive evaluation.*

8. X. MALDAGUE, *Theory and Practice of Infrared Technology for Non Destructive Evaluation Testing*, John Wiley & Sons, Inc., 2001.

9. P.O. MOORE, X. MALDAGUE, *NDT Handbook on Infrared technology*, ASNT Handbook Series, ASNT Press, 2001.

10. D. ALMOND, S.G. PICKERING, *An analytical study of the pulsed thermography defect detection limit*, Journal of Applied Physics 111(2012), 093152012.

11. G. BUSSE, *Thermal wave imaging with phase sensitive modulate thermography*, Journal of Applied Physics, 71/8, (1992).

12. LI.R. VOTI, *Thermal wave physics*, Journal of Optoelectronics and Advanced Materials, 3 (2001).

13. F.P. INCROPERA, et al., *Fundamentals of heat and mass transfer,* John Wiley & Sons, New York, 2007.

14. G.F. CAREY, M. TSAI, *Hyperbolic heat transfer with reflection,* Numerical Heat Transfer, 5 (1982), 309-327.

15. M. WANG, N. YANG and Z. GUO, *Non-Fourier heat conductions in nanomaterials,* J.Applied Physics.110(2011),064310.

16. C.R. CATTANEO, *Sur une forme de l'équation de la chaleur éliminant le paradoxe d'une propagation instantanée,* Comptes Rendus 247 (4): 431, 1958.

17. A.SALAZAR, *Energy propagation of thermal waves,* European Journal of Physics 27(2006), 1349-1355.

18. B. PULVIRENTI, E. ROSSI DI SCHIO, *Non-Fourier heat conduction by axisymmetric thermal waves in an infinite solid medium,* Heat and Mass Transfer 35(1999).

19. M. BERTOLOTTI, et al., *Thermal waves reflection and refraction: Theoretical and experimental evidence,* Journal of Applied Physics, 85(7), 1999.

20. F. GASPARRI, *Studio di tecniche termografiche attive con analisi di fase per controlli non distruttivi,* Politecnico di Milano, 2004.

21. F. PIU, *Studio sperimentale di nuove metodologie di analisi con la termografia modulata per il riconoscimento dei difetti,* Politecnico di Milano, 2005.

22. G. CASETTA, *Studio numerico - sperimentale per la rilevazione di difetti mediante termografia pulsata con analisi di fase,* Politecnico di Milano, 2007.

23. L.VITALI, *Ottimizzazione della tecnica sperimentale "Pulse Phase Thermography" per il controllo non distruttivo di provini sottili,* Politecnico di Milano, 2012.

24. X. MALDAGUE and S. MARINETTI, *Pulse phase infrared thermography,* Journal of Applied Physics, 79(5),1996.

25. F. GALMICHE, X. MALDAGUE, *Depth defect retrieval using the wavelet pulsed phase thermography,* Proc. of Qirt, 2000.

26. C. IBARRA-CASTENEDO, D. GONZÀLEZ and X. MALDAGUE, *Automatic algorithm for quantitative pulsed phase thermography calculations,* Available on www.ndt.net, 2004.

27. D.A. GONZÀLEZ, et al., *Differential absolute phase contrast algorithm for the analysis of pulsed thermography sequence,* Infrared Physics & Technology 48(2006),16-21.

28. V.S. GHALI, R. MULAVEESALA, *Comparative Data Processing Approaches for Thermal wave Imaging Technique for Non Destructive Testing*, Sens Imaging 12(2011), 15-33.

29. V. VAVILOV, *Pulsed thermal NDT of materials: back to the basics,* Nondestructive testing and evaluation, 22(2007), 2-3.

30. V. VAVILOV, *Infrared thermographic nondestructive testing of composite materials: determining thermal properties, detecting and characterizing hidden defects,* Available on www.ndt.net, 2010.

31. N.P. AVDELIDIS, et al., *A thermographic comparison study for the assesment of composite patches,* Infrared Physics and Technology, 45, 2004.

32. M. GENEST, *Image Processing for Automated Flaw Detection in Pulsed Thermography,* Available on www.ndt.net, 2009.

33. C. IBARRA-CASTENEDO, D. GONZÀLEZ and X. MALDAGUE, *Automatic Algorithm for quantitative pulsed phase thermography calculations,* Available on www.ndt.net, 2004.

34. R. MONTANINI, *Quantitative determination of subsurface defects in a reference specimen made of Plexiglas by means of Lock-in and pulse phase infared thermography,* Infrared Physics & Technology 53(2010),363-371.

35. K.E. CRAMERA, et al., *Status of Thermal NDT of Space Shuttle Materials at NASA,* NASA Report, available at http://ntrs.nasa.gov, 2006.

36. G. SHEN, G. CHEN, T. LI and C. LI, *Infrared Thermography for high temperature pressure pipe*, 10th Asia-Pacific Conference on Non-Destructive Testing, Brisbane, Australia, September, 2001.

37. X. MALDAGUE, *Pipe Inspection by Infrared Thermography*, Materials Evaluation (USA). Vol. 57(Sept. 1999), 899-902.

38. A. VAGESWAR, *Periscope infrared thermography for local wall thinning in tubes*, NDT&E Int, 42(4), 2009 275-282.

39. D. FUSTINONI, *Analisi della convezione forzata su supefici variamente strutturate*, Ph.D. Thesis, Politecnico di Milano, 2012.

40. A. GUTIÉRREZ FAJARDO, *An analytical and experimental study on defect recognition methodologies with Pulsed Phase Thermography*, Politecnico di Milano, 2005.

41. G. HENDORFER, G. MAYR and G. ZAUNER, *Wavelet - based subsurface defect characterization in pulsed phase thermography for non destructive evaluation*, *Wavelet Applications in Industrial Processing VI.* F. Truchtet, O. Laligant, 2009, Vol. 7248, 72480D - 1.

42. A. QUARTERONI, R. SACCO and F. SALERI, *Modellistica Numerica per Problemi Differenziali*, 3th edition, Springer, Italia, 2006.

43. A. BARLETTA, E. ZANCHINI, *Hyperbolic heat conduction and local equilibrium: a second law analysis*, Journal of Heat and Mass Transfer, vol.40(5), (1997), 1007-1016.

44. M.E. GURTIN, A.C.PIPKIN, *A general theory of heat conduction with finite speed waves*, Archives of Rational Mechanical Analysis, 31(1968), 113-126.

45. B.D. COLEMAN, M. FABRIZIO and D.R. OWEN, *On the thermodynamics of second sound in dielectric crystals*, Archives of Rational Mechanical Analysis, 80(1982), 135-158.

46. D. JOU, J. CASAS-VÀZQUEZ and G. LEBON, *Extended irreversible thermodynamics*, Reports on Progress in Physics, 51(1988), 1105-1179.

47. H. RAHIDEH, P. MALEKZADEH and M.R. GOLBAHAR HAGHIGHI, *Non-Fourier Heat Conduction Analysis with Temperature-Dependent Thermal Conductivity*, International Scholarly Research Network, ISRN Mechanical Engineering, 2011, Received 27 January 2011.
48. M.B. SAINTEY, D.P.ALMOND, *Defect sizing by transient thermography II: a numerical treatment*, Journal of Physics D: Applied Physics vol. 28, pp. 2539-2546, 1995.